APPLIED COMPUTATIONAL ELECTROMAGNETICS SOCIETY JOURNAL

MAY 2023 REVIEWERS

Agarwal
Yuanxi Cao
Jie Chen
Merit Cisneros-Gonzalez
Valentina Consolo
Dileepan Dhanasekaran
Stavroula Foteinopoulou
Piotr Gas
Muyu Hou
Pankaj Jha
Xiao Jian-Kang
Roman Kubacki

Tu-Lu Liang
Fabrizio Loreto
Antonino Musolino
Andrew Peterson
Anna Pietrenko-Dabrowska
Qurban Ali Shah
Ye Tian
Yasuhiro Tsunemitsu
Tiago Varum
Shu Wang
Xiaoyan Zhang

THE APPLIED COMPUTATIONAL ELECTROMAGNETICS SOCIETY JOURNAL

TABLE OF CONTENTS

Multi-level Power Series Solution for Large Surface and Volume Electric Field Integral Equation

Y. K. Negi[1], N. Balakrishnan[1], and S. M. Rao[2]

[1]Supercomputer Education Research Centre
Indian Institute of Science, Bangalore, Karnataka, 560012 India
yknegi@gmail.com, balki@iisc.ac.in

[2]Naval Research Laboratory
Washington DC, 20375, USA
sadasiva.rao@nrl.navy.mil

Abstract – In this paper, we propose a new multi-level power series solution method for solving a large surface and volume electric field integral equation-based H-Matrix. The proposed solution method converges in a fixed number of iterations and is solved at each level of the H-Matrix computation. The solution method avoids the computation of a full matrix, as it can be solved independently at each level, starting from the leaf level. Solution at each level can be used as the final solution, thus saving the matrix computation time for full H-Matrix. The paper shows that the leaf level matrix computation and solution with power series gives as accurate results as the full H-Matrix iterative solver method. The method results in considerable savings time and memory savings compared to the H-Matrix iterative solver. Further, the proposed method retains the $O(NlogN)$ solution complexity.

Index Terms – H-Matrix, Method of Moments (MoM), power series solution, surface electric field integral equation, volume electric field integral equation.

I. INTRODUCTION

With the use of ever increasing higher frequencies for various defence and civilian applications in the current world, the electrical size of electromagnetic scattering/radiation problem has grown drastically[1, 2]. Solving the electrically large problems numerically to obtain fast and accurate results is the biggest challenge in the Computational Electromagnetics (CEM) community. Also, with the increase in computing power and memory, the need for large-scale solution algorithms has grown even more. Out of the various numerical methods in CEM, the most popular methods are: a) the Finite Difference Time Domain (FDTD) [3] method in the time domain and b) the Method of Moments (MoM) [4] and Finite Element Method (FEM) [5] in the frequency domain. Traditionally, the frequency domain methods have been more popular than the time domain methods as most of the early experimental results were available in the frequency domain and validating the computational results was convenient and easy. Out of the various frequency domain methods, MoM based methods are highly accurate and flexible for modeling irregular structures, the MoM matrix can be computed with the Surface Electric Field Integral Equation (S-EFIE) for solving Perfect Electrical Conductor (PEC) problems with surface mesh, and the Volume Electric Field Integral Equation (V-EFIE) [6] for solving inhomogeneous dielectric problems with volume mesh. Further, the MoM leads to a smaller number of unknowns compared to FEM and is free from grid dispersion error. However, the MoM matrix is a full matrix compared to a sparse matrix for the FEM method. Hence, the solution to large size problems with MoM in electromagnetics requires high matrix memory and computation time due to the dense matrix. Note that MoM dense matrix computation, matrix vector product and storage cost scales to $O(N^2)$ for N number of unknowns. Solving the dense matrix with an iterative solver leads to $N_{itr}O(N^2)$ calculations for N_{itr} iteration with $O(N^2)$ for matrix-vector multiplication cost. With a direct solver, the complexity grows as $O(N^3)$. Various fast solver algorithms like Multi-Level Fast Multipole Algorithm (MLFMA) [6], Adaptive Integral Method (AIM) [7], FFT [8], IE-QR [9], and Hierarchical Matrix (H-Matrix) [10–12] have been proposed to overcome the MoM limitations of high memory and computation cost. Fast solver reduces the matrix memory, matrix fill time, and matrix-vector product time to $O(NlogN)$. The reduced matrix-vector product time improves the solution time to $N_{itr}O(NlogN)$ for N_{itr} iterations with various iterative solution methods like Bi-Conjugate Gradient (BiCG) or Generalized Minimum Residual (GMRES).

Fast solvers are built on the compressibility property of the far-field interaction matrices. The compression of the far-field matrices can be done using analytical matrix compression methods like MLFMA or AIM, and also with numerical matrix compression methods like H-Matrix. Compared to analytical compression methods, numerical compression methods are easy to implement and are kernel independent. All the fast solvers depend on the iteration count of the iterative solution methods. The convergence of the iterations depends on the condition number of the computed MoM matrix, and further, for a large number of unknowns, the convergence iteration count also increases. The high iteration count can be mitigated by using various preconditions like ILUT, Null-Field, and Schur's complement method based preconditioners [13–15]. The matrix preconditioner improves the condition number of the matrices and reduces the iteration count of the overall matrix solution. Despite the improvement in solution time, the use of preconditioners comes with the overhead of preconditioner computation time and extra preconditioner solution time for each iteration. Also, for the solving of a large number of unknowns, the iteration count may still be high.

Recently there has been a trend in the CEM community for the development of an iteration-free fast solver method for solving problems with a large number of unknowns. Various fast direct solvers [16, 17] have been proposed to overcome the iteration dependency of the solution process. These direct solvers are based on LU decomposition and compression methods. The methods are complex to implement and give quadratic scaling for complex real-world problems.

In this work, we propose a Multi-Level (ML) fast matrix solution method based on the power series [18, 19]. The proposed method exploits the property of ML matrix compression of the H-Matrix. The matrix is solved for each level using the matrix computation of the leaf level only, and the matrix solution can be terminated at the desired level as per the required accuracy. Our experimental results show that we get good accuracy even for the lowest level solution. The method relies on matrix-vector multiplication at each level and using the solution of the lowest level saves matrix computation time and memory requirement for the overall matrix solution.

The rest of the paper is organized as follows. Section II gives a summary of MoM computation for S-EFIE and V-EFIE, section III covers H-Matrix computation for S-EFIE and V-EFIE. The derivation of the proposed ML power series solver is given in section IV. The numerical results of the proposed method, and conclusion are discussed in sections V, and VI.

II. METHOD OF MOMENTS

MoM is a popular and efficient integral equation based method for solving various electromagnetic radiation/scattering problems. MoM can be computed using Electric Field Integral Equation (EFIE) for both surface and volume modeling. Surface modeling can be done using Rao Wilton Glisson (RWG) [20] triangle basis function, whereas volume modeling can be done using Schaubert Wilton Glisson (SWG) [21] tetrahedral basis function. In the case of dielectric modeling compared to S-EFIE, V-EFIE is an integral equation of the second kind and is more well-conditioned and stable. V-EFIE can model inhomogeneous bodies more efficiently than surface EFIE. In this work, we use RWG basis function for PEC surface S-EFIE modeling and SWG basis function for volume V-EFIE modeling. The surface/volume EFIE governing equation for the conductor/dielectric scattering body illuminated with the incident plane wave is given as the total electric field (E^{total}) from a scattering surface/volume and is the sum of incident electric field (E^{inc}) and scattered electric fields (E^{scatt}).

$$E^{total} = E^{inc} + E^{scatt}. \tag{1}$$

The scatted electric field is due to the surface current in PEC surface or volume polarization current in the dielectric media and is given as:

$$E^{scatt} = -j\omega A(r) - \nabla\phi(r). \tag{2}$$

In the above equation $A(r)$ is the magnetic vector potential and describes radiation of current, $\phi(r)$ is electric potential and describes associate bound charge. Applying the boundary condition for PEC structure the S-EFIE can be written as:

$$E^{inc} = j\omega A(r) + \nabla\phi(r). \tag{3}$$

Similarly, the V-EFIE can be written for a dielectric inhomogeneous body as:

$$E^{inc} = \frac{D(r)}{\varepsilon(r)} + j\omega A(r) + \nabla\phi(r). \tag{4}$$

In the above, equation $D(r)$ is the electric flux density and $\varepsilon(r)$ is the dielectric constant of the scattering volume media. The surface current in equation (3) for PEC structure is expanded with RWG function, and similarly in equation (4) for dielectric volume structure polarization current and charge is modeled with SWG basis function. Performing Galarkin testing over each term with integrating over the surface/volume, the final system of equation boils down to the linear system of the equation as below:

$$[Z]x = b. \tag{5}$$

In the above equation, $\boldsymbol{Z}$ is a dense MoM matrix, $\boldsymbol{b}$ is a known incident plane wave, and $\boldsymbol{x}$ is an unknown coefficient to be computed. The dense matrix leads to high cost matrix computation and memory requirement as well as solution time complexity. In the next section, we discuss the implementation of the H-Matrix for the mitigation of high cost of the conventional MoM matrix

III. H-MATRIX

The high cost of MoM limits its application to a few λ problem sizes. This limitation of MoM can be overcome by incorporating fast solvers. Most of the fast solvers work on the principle of compressibility of the far-field matrices. For the implementation of a fast solver, the mesh of geometry is divided into blocks using an oct-tree or binary-tree division process and terminated at the desired level with a limiting edge or face count in each block. The non-far-field interaction blocks at the lowest level are considered near-field blocks and are in the dense matrix form. The compression of the far-field block matrix at each level can be done analytically or numerically. The system of equations in equation (5) can now be written as the sum of near-field and far-field matrix form as:

$$[\boldsymbol{Z}_N + \boldsymbol{Z}_F]\boldsymbol{x} = \boldsymbol{b}. \qquad (6)$$

In the above equation $\boldsymbol{Z}_N$ is a near-field block matrix and $\boldsymbol{Z}_F$ is far-field compressed block matrices for the MoM fast solver matrix. Numerical compression of far-field matrices is easy to implement and is kernel-independent. A few of the popular fast solvers using numerical compression methods are IE-QR, H-Matrix. In this work, we have implemented H-Matrix for ML matrix compression. For the ML compression computation, the mesh is divided into ML binary tree division-based subgroups. H-Matrix works on the computation of a far-field matrix for the interaction blocks satisfying the admissibility condition given in equation (7). The admissibility condition states that η times the distance between the observation cluster (Ω_t) and source cluster (Ω_s) should be greater or equal to the minimum diameter of the observation cluster or source cluster for far-field computation, where η is the admissibility control parameter, and its value is taken as 1.0.

$$\eta \; dist(\Omega_t, \Omega_s) \geq min(diam(\Omega_t), diam(\Omega_s)). \qquad (7)$$

The far-field matrix block compression is done in such a way that its parent interaction matrix should not be computed at the top level. Matrix compression at each level is carried out using Adaptive Cross Approximation (ACA) [22] [23] method. The method exploits the rank deficiency property of the far-field matrix blocks. The low-rank sub-block of the far-field $\boldsymbol{Z}_{sub}$ with m rows and
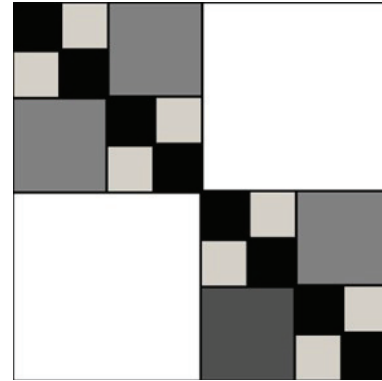
Fig. 1. Compressed far-field and dense near-field matrix blocks layout.

n columns is decomposed into approximate $\boldsymbol{U}_{(m \times k)}$ and $\boldsymbol{V}_{(k \times n)}$ matrices where k is the numerical rank of the low-rank sub-block far-field matrix such that $k << min(m, n)$. In this work, for memory savings, we only compute half of the H-Matrix [12] by making the computation process symmetric, and to maintain the accuracy of the H-Matrix, we use re-compressed ACA [24] for far-field block compression. The solution of the iterative solver is iteration count dependent, and further, the convergence iteration count depends on the condition number of the matrix. Also, as the number of unknowns increases, the iterating count for the convergence increases. In the next section, we discuss our proposed method, which is an iteration count and far-field level block independent solution process.

IV. MULTI-LEVEL POWER SERIES SOLUTION

The full H-Matrix is a combination of near-field and far-field block matrices. The far-field compressed block matrices are computed for various levels, and in equation (6), the far-field matrix ($\boldsymbol{Z}_F$) can be further decomposed into the different matrix levels as below:

$$[\boldsymbol{Z}_F] = [\boldsymbol{Z}_{F1}] + [\boldsymbol{Z}_{F2}] + [\boldsymbol{Z}_{F3}]. \qquad (8)$$

In the above equation far-field matrix $\boldsymbol{Z}_{F1}$ is for level 1, $\boldsymbol{Z}_{F2}$ is for level 2 and, $\boldsymbol{Z}_{F3}$ is for level 3. Level 3 forms the leaf level of the binary tree and level 1 as the top level of the tree. Figure 1 shows the H-Matrix layout for a two-dimension strip. In Fig. 1, light gray boxes represent $\boldsymbol{Z}_{F1}$ far-field matrix at level 1, dark gray boxes as $\boldsymbol{Z}_{F2}$ is for level 2 and large white boxes as $\boldsymbol{Z}_{F3}$ for level 3, the black boxes are the near-field dense matrices. For illustrative purposes, the near-field matrix is a diagonal block form for a two-dimension strip. The real-world problems are three-dimension in structure, giving a non-diagonal block near-field matrix. To implement our ML power series solution method, we must diagonalize the

near-field block matrix. The near-field matrix in equation (6) is diagonalized using diagonal scaling coefficient $[\boldsymbol{\alpha}]$, as computed in [15] such that the scaled diagonal block near-field matrix can be given as:

$$[\tilde{\boldsymbol{Z}}_N] = [\boldsymbol{\alpha}][\boldsymbol{Z}_N]. \tag{9}$$

Expanding equation (8) and scaling it with the scaling coefficients $[\boldsymbol{\alpha}]$ gives:

$$[\boldsymbol{\alpha}][\boldsymbol{Z}_N + \boldsymbol{Z}_{F1} + \boldsymbol{Z}_{F2} + \boldsymbol{Z}_{F3}]\boldsymbol{x} = [\boldsymbol{\alpha}]\boldsymbol{b}, \tag{10}$$

$$[\tilde{\boldsymbol{Z}}_N]\boldsymbol{x} + [\boldsymbol{\alpha}][\boldsymbol{Z}_{F1}]\boldsymbol{x} + [\boldsymbol{\alpha}][\boldsymbol{Z}_{F2}]\boldsymbol{x} + [\boldsymbol{\alpha}][\boldsymbol{Z}_{F3}]\boldsymbol{x} = \tilde{\boldsymbol{b}}. \tag{11}$$

In the above equation $\tilde{\boldsymbol{b}}$ is a $[\boldsymbol{\alpha}]$ scaled vector $\boldsymbol{b}$ and can be further simplified as:

$$\begin{aligned} \boldsymbol{x} + [\tilde{\boldsymbol{Z}}_N]^{-1}[\boldsymbol{\alpha}][\boldsymbol{Z}_{F1}]\boldsymbol{x} + [\tilde{\boldsymbol{Z}}_N]^{-1}[\boldsymbol{\alpha}][\boldsymbol{Z}_{F2}]\boldsymbol{x} \\ + [\tilde{\boldsymbol{Z}}_N]^{-1}[\boldsymbol{\alpha}][\boldsymbol{Z}_{F3}]\boldsymbol{x} = [\tilde{\boldsymbol{Z}}_N]^{-1}\tilde{\boldsymbol{b}}. \end{aligned} \tag{12}$$

Let $[\tilde{\boldsymbol{Z}}_N]^{-1}[\boldsymbol{\alpha}][\boldsymbol{Z}_{F1}] = [\boldsymbol{U}_1]$, $[\tilde{\boldsymbol{Z}}_N]^{-1}[\boldsymbol{\alpha}][\boldsymbol{Z}_{F2}] = [\boldsymbol{U}_2]$ and $[\tilde{\boldsymbol{Z}}_N]^{-1}[\boldsymbol{\alpha}][\boldsymbol{Z}_{F3}] = [\boldsymbol{U}_3]$ equation (12) can further be simplified as:

$$\boldsymbol{x} + [\boldsymbol{U}_1]\boldsymbol{x} + [\boldsymbol{U}_2]\boldsymbol{x} + [\boldsymbol{U}_3]\boldsymbol{x} = [\tilde{\boldsymbol{Z}}_N]^{-1}\tilde{\boldsymbol{b}}, \tag{13}$$

$$[\boldsymbol{I} + \boldsymbol{U}_1]\boldsymbol{x} + [\boldsymbol{U}_2]\boldsymbol{x} + [\boldsymbol{U}_3]\boldsymbol{x} = [\tilde{\boldsymbol{Z}}_N]^{-1}\tilde{\boldsymbol{b}}, \tag{14}$$

$$\begin{aligned} \boldsymbol{x} + [\boldsymbol{I} + \boldsymbol{U}_1]^{-1}[\boldsymbol{U}_2]\boldsymbol{x} + [\boldsymbol{I} + \boldsymbol{U}_1]^{-1}[\boldsymbol{U}_3]\boldsymbol{x} \\ = [\boldsymbol{I} + \boldsymbol{U}_1]^{-1}[\tilde{\boldsymbol{Z}}_N]^{-1}\tilde{\boldsymbol{b}}. \end{aligned} \tag{15}$$

Let $[\boldsymbol{I} + \boldsymbol{U}_1]^{-1}[\boldsymbol{U}_2] = [\boldsymbol{V}_2]$ and $[\boldsymbol{I} + \boldsymbol{U}_1]^{-1}[\boldsymbol{U}_3] = [\boldsymbol{V}_3]$ equation (15) can further be simplified as:

$$\boldsymbol{x} + [\boldsymbol{V}_2]\boldsymbol{x} + [\boldsymbol{V}_3]\boldsymbol{x} = [\boldsymbol{I} + \boldsymbol{U}_1]^{-1}[\tilde{\boldsymbol{Z}}_N]^{-1}\tilde{\boldsymbol{b}}, \tag{16}$$

$$\boldsymbol{x} + [\boldsymbol{I} + \boldsymbol{V}_2]^{-1}[\boldsymbol{V}_3]\boldsymbol{x} = [\boldsymbol{I} + \boldsymbol{V}_2]^{-1}[\boldsymbol{I} + \boldsymbol{U}_1]^{-1}[\tilde{\boldsymbol{Z}}_N]^{-1}\tilde{\boldsymbol{b}}. \tag{17}$$

Let $[\boldsymbol{I} + \boldsymbol{V}_2]^{-1}[\boldsymbol{V}_3] = [\boldsymbol{W}_3]$ and equation (17) can be written as:

$$\boldsymbol{x} + [\boldsymbol{W}_3]\boldsymbol{x} = [\boldsymbol{I} + \boldsymbol{V}_2]^{-1}[\boldsymbol{I} + \boldsymbol{U}_1]^{-1}[\tilde{\boldsymbol{Z}}_N]^{-1}\tilde{\boldsymbol{b}}, \tag{18}$$

$$\boldsymbol{x} = [\boldsymbol{I} + \boldsymbol{W}_3]^{-1}[\boldsymbol{I} + \boldsymbol{V}_2]^{-1}[\boldsymbol{I} + \boldsymbol{U}_1]^{-1}[\tilde{\boldsymbol{Z}}_N]^{-1}\tilde{\boldsymbol{b}}. \tag{19}$$

In the above equations $[\boldsymbol{I} + \boldsymbol{W}_3]^{-1}, [\boldsymbol{I} + \boldsymbol{V}_2]^{-1}$ and $[\boldsymbol{I} + \boldsymbol{U}_1]^{-1}$ can be solved independently at each level using a power series solution method with the expansion as below:

$$[\boldsymbol{I} + \boldsymbol{U}_1]^{-1} = [\boldsymbol{I} + [\tilde{\boldsymbol{Z}}_N]^{-1}[\boldsymbol{\alpha}][\boldsymbol{Z}_{F1}]]^{-1}, \tag{20}$$

$$[\boldsymbol{I} + \boldsymbol{V}_2]^{-1} = [\boldsymbol{I} + [\boldsymbol{I} + \boldsymbol{U}_1]^{-1}[\boldsymbol{U}_2]]^{-1}$$

$$= [\boldsymbol{I} + [\boldsymbol{I} + [\tilde{\boldsymbol{Z}}_N]^{-1}[\boldsymbol{\alpha}][\boldsymbol{Z}_{F1}]]^{-1}[\tilde{\boldsymbol{Z}}_N]^{-1}[\boldsymbol{\alpha}][\boldsymbol{Z}_{F2}]]^{-1}, \tag{21}$$

$$[\boldsymbol{I} + \boldsymbol{W}_3]^{-1} = [\boldsymbol{I} + [\boldsymbol{I} + \boldsymbol{V}_2]^{-1}[\boldsymbol{V}_3]]^{-1}$$

$$= [\boldsymbol{I} + [\boldsymbol{I} + [\boldsymbol{I} + \boldsymbol{U}_1]^{-1}[\boldsymbol{U}_2]]^{-1}[\boldsymbol{I} + \boldsymbol{U}_1]^{-1}[\boldsymbol{U}_3]]^{-1}$$

$$= [\boldsymbol{I} + [\boldsymbol{I} + [\boldsymbol{I} + [\tilde{\boldsymbol{Z}}_N]^{-1}[\boldsymbol{\alpha}][\boldsymbol{Z}_{F1}]]^{-1}[\tilde{\boldsymbol{Z}}_N]^{-1}[\boldsymbol{\alpha}][\boldsymbol{Z}_{F2}]]^{-1}$$

$$[\boldsymbol{I} + [[\tilde{\boldsymbol{Z}}_N]^{-1}[\boldsymbol{\alpha}][\boldsymbol{Z}_{F1}]]^{-1}[\tilde{\boldsymbol{Z}}_N]^{-1}[\boldsymbol{\alpha}][\boldsymbol{Z}_{F3}]]^{-1}. \tag{22}$$

From equations (20), (21), and (22), it can be observed that the solution of these equations is dependent on that level and the lower levels of the binary tree block interaction matrix. At each level, the inverse of the matrix system equation can be efficiently computed by using a fast power series solution [18]. The fast power series iterative solution converges in two fixed iterations. The solution process only depends on the matrix-vector product of the H-Matrix, thus retaining the complexity of $O(NlogN)$[18]. The ML solution can be computed at the desired level per the required accuracy. Our results show that the solution at the leaf level gives an accurate result leading to time and memory savings.

V. NUMERICAL RESULTS

In this section, we show the accuracy and efficiency of the proposed method. The simulations are carried out on 128 GB memory and an Intel (Xeon E5-2670) processor system for the double-precision data type. The H-Matrix computation is done with the ACA matrix compression error tolerance of 1e-3 [22] and solved with GMRES iterative solver with convergence tolerance of 1e-6 [12]. For a compressed or dense matrix $[\boldsymbol{Z}]$ if we want to expand $[1 + \boldsymbol{Z}]^{-1}$ in power series, the necessary and sufficient condition for convergence is $|\boldsymbol{Z}| < 1$ and we choose 0.1 for our simulations [25]. The conductor and dielectric geometry with dielectric constant ε_r is meshed with an element size less than $\lambda/10$ and $\lambda/(10\sqrt{\varepsilon_r})$ respectively. To show the accuracy of the proposed method, the RCS results are compared with full H-Matrix iterative solver [12]. In the further subsections, we demonstrate the far-field memory and computation time savings in along with in solution time saving with our proposed ML power series solution with different examples.

A. PEC square plate

To show the accuracy and efficiency on a PEC object in this subsection, we consider a square plate of size 15.0 λ along x and y axis meshed with 67,200 unknown edges. The square plate mesh is divided with binary tree division till level 6. The PEC S-EFIE H-Matrix is solved with ML the power series solution method and H-Matrix

iterative solver. The ML power series converges in 2 iterations, and the iterative solver solution converges in 686. Only the far-field matrix at leaf level 6 is computed for the ML power series solution, ignoring far-field computation from levels 1 to 5 of the binary tree.
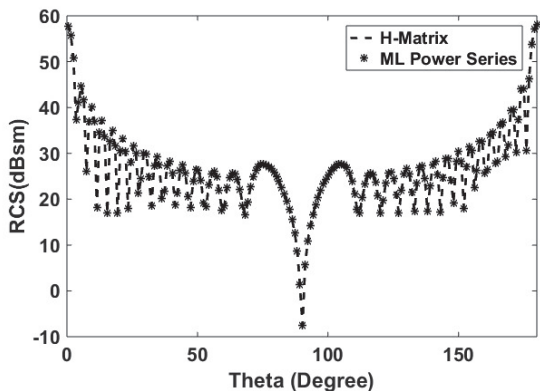
Fig. 2. Bi-static RCS of the PEC square plate with VV polarized plane wave incident at $\theta = 0°$, $\phi = 0°$, and observation angles $\theta = 0°$ to $180°$, $\phi = 0°$.

Figure 2 shows the Bi-static RCS of a PEC square plate, and from the figure it can be observed that the solution with the ML power series solver matches with the H-Matrix iterative solver. Table 1 shows the savings in memory, computation, and solution time of the ML power series solution method as compared with a conventional H-Matrix-based iterative solver.

Table 1: Matrix memory, fill and solution time for a PEC square plate

	Memory (GB)	Matrix Fill Time (H)	Solution Time (sec)
H-Matrix	5.04	1.24	500.85
ML Power Series	4.71	1.08	3.95

B. Dielectric slab

To show the accuracy and efficiency for a considerable size dielectric problem in this subsection, we consider a dielectric slab elongated along the y-axis with a height of $10.0\ \lambda$ length, $1.0\ \lambda$ width, and $0.1\ \lambda$ thickness and dielectric constant ($\varepsilon_r = 2.0$) meshed with 120,080 tetrahedral faces. The ML power series converges in 2 iterations, and the regular H-Matrix iterative solver converges in 33 iterations.

The dielectric slab mesh is divided with binary tree division till level 10. Only the far-field matrix at leaf level 10 is computed for the ML power series solution. The accuracy of the method for a Bi-static RCS is shown
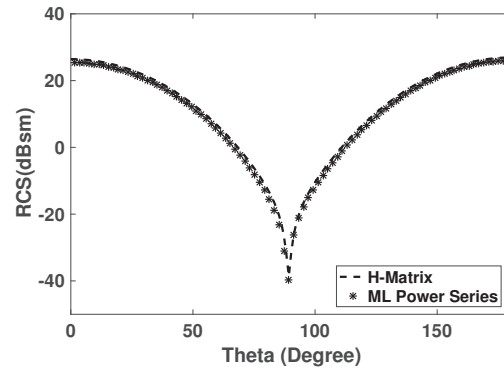
Fig. 3. Bi-static RCS of the dielectric slab with VV polarized plane wave incident at $\theta = 0°$, $\phi = 0°$, and observation angles $\theta = 0°$ to $180°$, $\phi = 0°$.

Table 2: Matrix memory, fill and solution time for a dielectric slab

	Memory (GB)	Matrix Fill Time (H)	Solution Time (sec)
H-Matrix	2.09	6.12	24.52
ML Power Series	0.50	1.46	7.50

in Fig. 3. Table 2 shows the significant matrix memory, matrix fill and solution time savings of the ML power series solution compared to the conventional H-Matrix-based iterative solver.
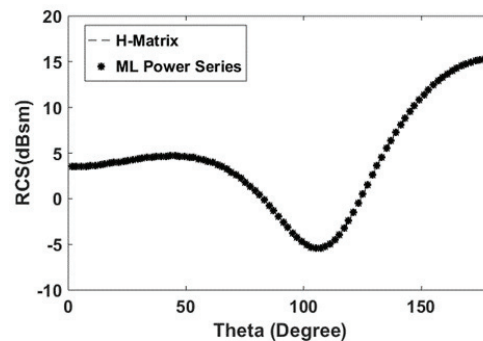
Fig. 4. Bi-static RCS of a dielectric hollow cylinder with VV polarized plane wave incident at $\theta = 0°$, $\phi = 0°$, and observation angles $\theta = 0°$ to $180°$, $\phi = 0°$.

C. Dielectric hollow cylinder

In this subsection, we consider a dielectric hollow cylinder elongated along the y-axis with a size of 6.0λ length, 0.4λ outer radii, and 0.05λ thickness with a dielectric constant ($\varepsilon_r = 2.0$), meshed with 158,830 tetrahedral faces. The ML power series converges in 2 iterations, and the H-Matrix iterative solver converges in 24 iterations.

The hollow cylinder mesh is partitioned with a binary tree division till level 8, and for the ML power series solution only the far-field matrix at leaf level 8 is computed. Figure 4 shows the close match in the bi-static RCS computed using the ML power series method and that with regular H-Matrix iterative solver. Table 3 shows the memory and time saving of the ML power series solution compared to the conventional H-Matrix iterative solver.

Table 3: Matrix memory, fill and solution time for a dielectric hollow cylinder

	Memory (GB)	Matrix Fill Time (H)	Solution Time (sec)
H-Matrix	3 .38	10.00	54.52
ML Power Series	0.44	1.26	16.16

VI. CONCLUSION

It can be observed from the illustrative examples in the previous sections that our proposed ML power series solution method gives considerable matrix memory, fill and solve time saving for significant size problems. The solution method is as accurate as the H-Matrix iterative solver. The savings may not be substantial for small-size mesh structures. Still, the method will give significant savings for large-size problems taken up for illustration and for complex and sizeable electrical problems like antenna arrays and complex composite structures. Also, the technique is entirely algebraic in nature and can apply to fast analytical solver-based methods like AIM and MLFMA. The matrix block in each level can be computed independently, and the solution of the method only depends on the matrix-vector product of the system matrix. Hence, the proposed method is amenable to efficient parallelization.

REFERENCES

[1] V. P. Padhy, Y. K. Negi, and N. Balakrishnan, "RCS enhancement due to Bragg scattering," *2012 International Conference on Mathematical Methods in Electromagnetic Theory, Kharkiv Ukraine*, pp. 443-446, IEEE, 28-30 Aug. 2012.

[2] Y. K. Negi, V. P. Padhy and N. Balakrishnan, "RCS enhancement of concealed/hidden objects at Terahertz (THz)," *27th Annual Review of Progress in Applied Computational Electromagnetics Williamsburg, Virginia, USA*, pp. 347-350, 27-31 March 2011.

[3] A. Taflove, *The Finite Difference Time Domain Method.*, Boston, Artech House, 1995.

[4] R. Harrington, *Field Computation by Moment Methods*, Malabar, Florida, RE Krieger Publishing Company, 1982.

[5] J.-M. Jin, *The Finite Element Method in Electromagnetics*, Hoboken New Jersey, John Wiley & Sons, 2015.

[6] W. C. Chew, E. Michielssen, J. Song, and J.-M. Jin, *Fast and Efficient Algorithms in Computational Electromagnetics*, Norwood, MA, USA: Artech House, Inc., 2001.

[7] E. Bleszynski, M. Bleszynski, and T. Jaroszewicz, "AIM: Adaptive integral method for solving large-scale electromagnetic scattering and radiation problems," *Radio Science*, vol. 31, no. 5, pp. 1225-1251, Sept.-Oct. 1996.

[8] J. R. Phillips and J. K. White, "A precorrected-FFT method for electrostatic analysis of complicated 3-D structures," *IEEE Transactions on Computer-aided Design of Integrated Circuits and Systems*, vol. 16, no. 10, pp. 1059-1072, Oct. 1997.

[9] S. Kapur and D. E. Long, "N-body problems: IES 3: Efficient electrostatic and electromagnetic simulation," *IEEE Computational Science and Engineering*, vol. 5, no. 4, pp. 60-67, Oct.-Dec. 1998.

[10] W. Hackbusch, "A sparse matrix arithmetic based on-matrices. Part I: Introduction to-matrices," *Computing*, vol. 62, no. 2, pp. 89-108, Apr. 1999.

[11] W. Hackbusch and B. N. Khoromskij, "A sparse H-matrix arithmetic, part II: Application to multi-dimensional problems," *Computing*, vol. 64, no. 1, pp. 21-47, Feb. 2000.

[12] Y. K. Negi, "Memory reduced half hierarchal matrix (H-matrix) for electrodynamic electric field integral equation," *Progress in Electromagnetics Research Letters*, vol. 96, pp. 91-96, Feb. 2021.

[13] Y. Saad, "ILUT: A dual threshold incomplete LU factorization," *Numerical Linear Algebra with Applications*, vol. 1, no. 4, pp. 387-402, Jul.-Aug. 1994.

[14] Y. K. Negi, N. Balakrishnan, S. M. Rao, and D. Gope, "Null-field preconditioner with selected far-field contribution for 3-D full-wave EFIE," *IEEE Transactions on Antennas and Propagation*, vol. 64, no. 11, pp. 4923-4928, Nov. 2016.

[15] Y. K. Negi, N. Balakrishnan, and S. M. Rao, "Symmetric near-field Schur's complement preconditioner for hierarchal electric field integral equation solver," *IET Microwaves, Antennas & Propagation*, vol. 14, no. 14, pp. 1846-1856, Nov. 2020.

[16] L. Greengard, D. Gueyffier, P.-G. Martinsson, and V. Rokhlin, "Fast direct solvers for integral equations in complex three-dimensional domains," *Acta Numerica*, vol. 18, pp. 243-275, May 2009.

[17] J. Shaeffer, "Direct solve of electrically large integral equations for problem sizes to 1 M unknowns," *IEEE Transactions on Antennas and Propagation*, vol. 56, no. 8, pp. 2306-2313, Aug. 2008.

[18] Y. K. Negi, N. Balakrishnan, and S. M. Rao, "Fast power series solution of large 3-D electrodynamic integral equation for PEC scatterers," *Applied Computational Electromagnetics Society (ACES) Journal*, pp. 1301-1311, Nov. 2021.

[19] S. M. Rao, "A new multi-level power series solution algorithm to solve electrically large electromagnetic scattering problems applicable to conducting bodies," *2021 International Conference on Electromagnetics in Advanced Applications (ICEAA)*, Honolulu, HI, USA, pp. 152-152, 09-13 Aug. 2021.

[20] S. Rao, D. Wilton, and A. Glisson, "Electromagnetic scattering by surfaces of arbitrary shape," *IEEE Transactions on Antennas and Propagation*, vol. 30, no. 3, pp. 409-418, May 1982.

[21] D. Schaubert, D. Wilton, and A. Glisson, "A tetrahedral modeling method for electromagnetic scattering by arbitrarily shaped inhomogeneous dielectric bodies," *IEEE Transactions on Antennas and Propagation*, vol. 32, no. 1, pp. 77-85, Jan. 1984.

[22] M. Bebendorf, "Approximation of boundary element matrices," *Numerische Mathematik*, vol. 86, pp. 565-589, Oct. 2000.

[23] S. Kurz, O. Rain, and S. Rjasanow, "The adaptive cross-approximation technique for the 3D boundary-element method," *IEEE Transactions on Magnetics*, vol. 38, no. 2, pp. 421-424, Aug. 2002.

[24] Y. K. Negi, V. P. Padhy, and N. Balakrishnan, "Re-compressed H-matrices for fast electric field integral equation," *2020 IEEE International Conference on Computational Electromagnetics (ICCEM)*, pp. 176-177, Singapore, 2020.

[25] S. M. Rao and M. S. Kluskens, "A new power series solution approach to solving electrically large complex electromagnetic scattering problems," *Applied Computational Electromagnetics Society (ACES) Journal*, pp. 1009-1019, Aug. 2021.

Yoginder Kumar Negi obtained the B.Tech degree in Electronics and Communic-ation Engineering from Guru Gobind Singh Indraprastha University, New Delhi, India, in 2005, M.Tech degree in Microwave Electronics from Delhi University, New Delhi, India, in 2007 and the PhD degree in engineering from Indian Institute of Science (IISc), Bangalore, India, in 2018.

Dr Negi joined Supercomputer Education Research Center (SERC), IISc Bangalore in 2008 as a Scientific Officer. He is currently working as a Senior Scientific Officer in SERC IISc Bangalore. His current research interests include numerical electromagnetics, fast techniques for electromagnetic application, bio-electromagnetics, high-performance computing, and antenna design and analysis.

B. Narayanaswamy received the B.E. degree (Hons.) in Electronics and Communi-cation from the University of Madras, Chennai, India, in 1972, and the Ph.D. degree from the Indian Institute of Science, Bengaluru, India, in 1979.

He joined the Department of Aerospace Engineering, Indian Institute of Science, as an Assistant Professor, in 1981, where he became a Full Professor in 1991, served as the Associate Director, from 2005 to 2014, and is currently an INSA Senior Scientist at the Supercomputer Education and Research Centre. He has authored over 200 publications in the international journals and international conferences. His current research interests include numerical electromagnetics, high-performance computing and networks, polarimetric radars and aerospace electronic systems, information security, and digital library.

Dr. Narayanaswamy is a fellow of the World Academy of Sciences (TWAS), the National Academy of Science, the Indian Academy of Sciences, the Indian National Academy of Engineering, the National Academy of Sciences, and the Institution of Electronics and Telecommunication Engineers.

Sadasiva M. Rao obtained his Bachelors, Masters, and Doctoral degrees in electrical engineering from Osmania University, Hyderabad, India, Indian Institute of Science, Bangalore, India, and University of Mississippi, USA, in 1974, 1976, and 1980, respectively. He is well known in the electromagnetic engineering community and included in the Thomson Scientifics' *Highly Cited Researchers List*.

Dr. Rao has been teaching electromagnetic theory, communication systems, electrical circuits, and other related courses at the undergraduate and graduate level for the past 30 years at various institutions. At present, he is working at Naval Research Laboratories, USA. He published/presented over 200 papers in various journals/conferences. He is an elected Fellow of IEEE.

Scattering and Diffraction Evaluated by Physical Optics Surface Current on a Truncated Cylindrical Conductive Cap

Mustafa Kara[1] and Mustafa Mutlu[2]

[1]Department of Electronics and Automation, Technical Sciences MYO
Ordu University, Ordu, 52200, Turkey
mustafa.kara@odu.edu.tr

[2]Department of Electronics and Automation, Technical Sciences MYO
Ordu University, Ordu, 52200, Turkey
mustafamutlu@odu.edu.tr

Abstract – In this study physical optics (PO) surface current is obtained by using the Malyughinetz solution to get the scattered field expression for a truncated cylindrical conductive cap satisfying the related boundary conditions given throughout this paper. This is done by using the inverse edge point method for the transformation from the Malyughinetz solution for the wave diffraction by a half plane to the wave diffraction by a truncated conductive cylinder. This transformation method can be used to examine the diffraction and scattering phenomena for curved surfaces having discontinuities as dealt with in this work. Total scattered field comprising the incident and scattered fields is plotted with respect to the observation angle for some parameters of the problem. The obtained results are examined numerically for the same parameters.

Index Terms – conductive surface, diffraction, physical optics, scattering, truncated cylindrical cap.

I. INTRODUCTION

Scattering and diffraction by the objects of curved shapes have been under investigation for decades. Franz and Klante examined the diffraction phenomenon by the variable-curvature surfaces by applying the integral equation method to a convex cylinder [1]. Hong presented a method to obtain successive terms in short wavelength asymptotic expansions of the diffracted field by a smooth convex surface on which a plane acoustic or electromagnetic wave is incident [2]. Bahar derived a solution for the diffracted fields around a convex cylindrical boundary having a varying radius of curvature and surface impedance [3]. In the study of Idemen and Felsen, whispering gallery mode diffraction of a thin, concave, cylindrically curved surface was analyzed by using the Fourier transform method [4]. Idemen and

Erdoğan examined the diffraction of creeping waves by a spherical reflector, and derived diffraction coefficient expressions [5]. In the study of Serbest, diffraction of whispering gallery modes by a conducting spherical reflector was examined, and diffraction or transformation coefficients were obtained [6]. Büyükaksoy studied the diffraction at high frequencies by the edge of a cylindrically curved surface whose convex and concave sides show soft and hard boundary conditions [7]. New diffraction coefficients for the mixed boundary conditions were also defined in the study. Hansen and Shore obtained the inremental length diffraction coefficients at the shadow boundaries for a perfectly electric conducting convex cylinder [8]. Yalçın investigated the scattering by a perfectly conducting cylindrical reflector by using the Modified Theory of Physical Optics (MTPO) [9]. By using the surface integrals of the MTPO, Umul investigated the scattering phenomenon by a cylindrical parabolic impedance reflector [10]. Umul transformed Malyughinetz solution for the scattering by a half screen of equal face impedances to a Physical Optics (PO) integral to employ it in the problem of diffraction by a truncated impedance cylinder [11]. Andronov examined the diffraction of a high-frequency plane wave by an infinite cylinder having a strongly prolate ellipse cross-section [12]. Andronov and Lavrov investigated the scattering by an elliptic cylinder having strongly elongated cross-section by obtaining uniform asymptotic expressions [13]. Başdemir investigated the diffraction of inhomogeneous plane waves for a truncated cylindrical cap [14]. Shanin and Korolkov analyzed the diffraction by a parabola by introducing a Volterra-type boundary integral equation [15]. We investigated the scattering of plane waves by a cylindrical, parabolic, perfectly electric conductor reflector [16]. In this study which will be a new work in the literature, our aim is to use the field expression of a plane wavediffracted by a half plane for

obtaining the PO surface current on the truncated cylindrical conductive cap. The novelty of this study is that, as a new approach, instead of solving the scattering problem in a conventional way, we will transform the solution of wave scattering problem by a half plane into PO integral via inverse edge point method for a truncated cylindrical conductive cap. PO current that can be used in wide variety of problems will be employed to express the scattered field. For scattering, PO method could be widely used in various situations including mesh-type antennas and cross-section applications.

II. THEORY

The geometry of the problem is given in Fig. 1 where the radius of the cylinder is a, and the incident plane wave is taken as

$$E_i = E_0 e^{jkx}, \qquad (1)$$

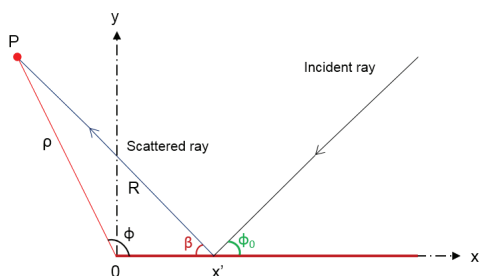where E_0 is the amplitude, and k is the wavenumber.

Fig. 1. Scattered beam geometry for the conductive half-plane.

The truncated cylindrical cap is located symmetrically with respect to the x-axis, $\phi \in [-\phi_0, \phi_0]$ and $z \in (-\infty, \infty)$. Boundary conditions for the conductive surface are given as

$$\vec{n} \times (\vec{H}_1 - \vec{H}_2)\,|_S = 0, \qquad (2)$$

and

$$\vec{n} \times (\vec{n} \times \vec{H}_1)\,|_S = R_m \vec{n} \times (\vec{E}_2 - \vec{E}_1)\,|_S, \qquad (3)$$

where $\vec{n}$ is the unit vector of the surface, and $\vec{E}$ and $\vec{H}$ are the electric and magnetic fields respectively. $\vec{E}_1$ and $\vec{H}_1$ are the fields on the convex side, and $\vec{E}_2$ and $\vec{H}_2$ are the ones on the concave side of the cylinder. The diffracted field in [18, 19], can be rewritten for a conductive half plane as

$$E_d = -\frac{E_0 2\cos(\frac{\phi}{2})\cos(\frac{\phi_0}{2})}{\sin\theta(\cos\phi + \cos\phi_0)} K_+(\phi, \theta) K_+(\phi_0, \theta)$$
$$\times \frac{exp(-j\frac{\pi}{4})}{\sqrt{2\pi}} \frac{exp(-jk\rho)}{\sqrt{k\rho}}, \qquad (4)$$

where

$$\sin\theta = 2R_m Z_0. \qquad (5)$$

R_m is the conductivity of the surface, and Z_0 is the characteristic impedance of free space. Scattered field is expressed as

$$E_s = E_0 \frac{kexp(-\frac{j\pi}{4})}{\sqrt{2\pi}}$$
$$\times \int_0^\infty J_{PO} \frac{exp(-jkR)}{\sqrt{kR}} exp(jkx'\cos\phi_0)dx', \qquad (6)$$

where J_{PO} is the physical optics surface current, and

$$R = \sqrt{\rho^2 + x'^2 - 2\rho x'\cos\phi}. \qquad (7)$$

Diffracted field at the edge point can be written as

$$E_d = -\frac{1}{jk} \frac{kE_0 exp(\frac{j\pi}{4})}{\sqrt{2\pi}}$$
$$\times J_{PO}(x' = 0) \frac{exp(-jk\rho)}{\sqrt{k\rho}} \frac{1}{\cos\phi + \cos\phi_0}. \qquad (8)$$

At the edge point J_{PO} is concluded as

$$J_{PO}(x' = 0) = 2\cos(\frac{\phi}{2})\cos(\frac{\phi_0}{2})K_+(\phi, \theta)K_+(\phi_0, \theta), \qquad (9)$$

where K_+ is the split function first given by Senior [17]. Split function is expressed by means of Malyughinetz function by Senior [18], and Senior and Volakis [19]. Split functions are used for the transition from geometrical optics fields to diffracted fields. K_+ has the form of

$$K_+(\alpha, \beta) = \frac{4\sqrt{\sin\beta}\sin(\frac{\alpha}{2})}{(1 + \sqrt{2}\cos(\frac{\frac{\pi}{2}-\alpha+\beta}{2}))(1 + \sqrt{2}\cos(\frac{\frac{3\pi}{2}-\alpha-\beta}{2}))}$$
$$\times (\frac{\psi_\pi(\frac{3\pi}{2} - \alpha - \beta)\psi_\pi(\frac{\pi}{2} - \alpha + \beta)}{(\psi_\pi(\frac{\pi}{2}))^2})^2, \qquad (10)$$

where $\psi_\pi(\delta)$ is the Malyughinetz function that is written as

$$\psi_\pi(a) = exp(-\frac{1}{8\pi} \int_0^a \frac{\pi\sin x - 2\sqrt{2}\pi\sin(\frac{x}{2}) + 2x}{\cos x}dx). \qquad (11)$$

In Fig. 2, β_e is the diffraction angle of the ray at the edge point, and incident ray is parallel to the x-axis. Scattered field is written as

$$E_s = E_0 \frac{kexp(-\frac{j\pi}{4})}{\sqrt{2\pi}}$$
$$\times \int_{-\phi_0}^{\phi_0} J_{PO} \frac{exp(-jkR)}{\sqrt{kR}} exp(jka\cos\phi_0)d\phi', \qquad (12)$$

where

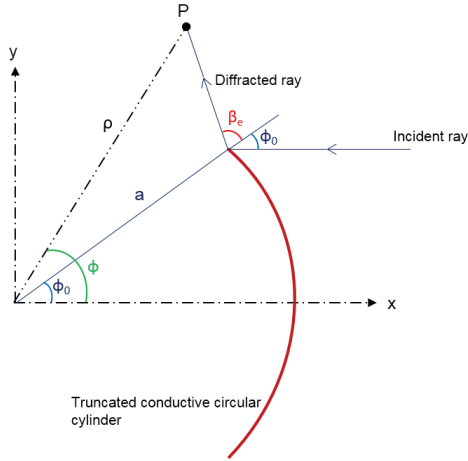$$R = \sqrt{\rho^2 + a^2 - 2\rho a'\cos(\phi - \phi')}. \qquad (13)$$

Fig. 2. Diffracted beam geometry for a truncated conductive circular cylinder.

Considering Fig. 1 at the edge point, it is written that $J_{PO}(\beta) = J_{PO}(\pi - \phi)$. At any point x', exact J_{PO} is expressed with respect to β as

$$J_{PO_{exact}}(\beta) = 2\sin(\frac{\beta}{2})cos(\frac{\phi_0}{2})K_+(\phi,\theta)K_+(\phi_0,\theta),$$

$$(14)$$

which can be used in the scattered field expression in equation (12). By considering the equations (8) and (14), the incident diffracted field can be concluded as

$$E_{id} = \frac{J_{PO_{exact}}(\beta)}{\sin\phi_0}f_1,$$

$$(15)$$

where

$$f_1 = E_0 sin(\frac{\beta_e + \phi_0}{2})exp(jka\cos(\phi_0))$$
$$\times exp(-jkR_e\cos(\beta_e + \phi_0))sign(\xi_{id})F[|\xi_{id}|],$$

$$(16)$$

and

$$\xi_{id} = -\sqrt{2kR_e}\sin(\frac{\phi + \phi_0}{2}),$$

$$(17)$$

where R_e is the distance between the edge and observation points. The reflected diffracted field is written as

$$E_{rd} = \frac{J_{PO_{exact}}(\beta)}{\sin\phi_0}f_2,$$

$$(18)$$

where

$$f_2 = E_0 cos(\frac{\beta_e - \phi_0}{2})exp(jka\cos(\phi_0))$$
$$\times exp(-jkR_e\cos(\beta_e - \phi_0))sign(\xi_{rd})F[|\xi_{rd}|],$$

$$(19)$$

and

$$\xi_{rd} = -\sqrt{2kR_e}\sin(\frac{\beta_e - \phi_0}{2}).$$

$$(20)$$

III. NUMERICAL RESULTS

In this section we will plot the total scattered field, which is the combination of incident and scattered fields, for some parameters of the problem. ρ is the observation distance, λ is the wavelength, and a is the radius of the cylinder cap. E_0 is taken as unity for simplicity. For the Figs. 3-6, total scattered fields are plotted with respect to the observation angle ϕ.

In Fig. 3, total scattered field variation according to theta is shown. $a = 2\lambda$, $\rho = 10\lambda$, and $\phi_0 = \pi/3$ are taken. For $\phi \in [-\pi/6, \pi/6]$ and $\phi \in [5\pi/6, 7\pi/6]$ total scattered field intensity almost does not change according to θ variation. But for For $\phi \in [\pi/6, 5\pi/6]$ and $\phi \in [7\pi/6, 11\pi/6]$, a change in the intensity occurs in a way that when the θ decreases, the intensity increases. As expected, intensity decays as the value of θ increases when considering equation (12) in which J_{PO} causes this variation. Also, an increase in θ implies an increase in the conductivity which results in a decrease in the total scattered field.
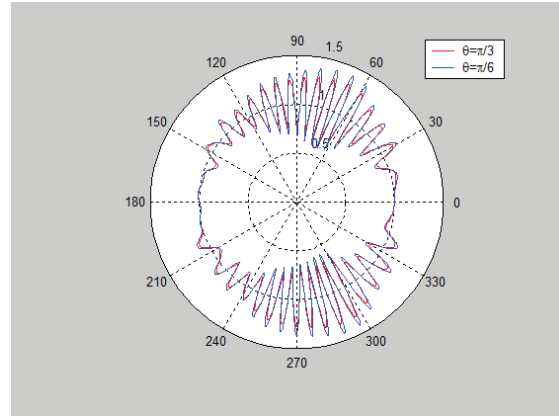
Fig. 3. Total scattered field variation for some θ values.

In Fig. 4, total scattered field is plotted according to cylinder radius a for the parameter values of $\rho = 6\lambda$, and $\phi_0 = \theta = \pi/3$. It is observed that between $\phi = -\pi/3$ and $\phi = \pi/3$ the field intensity decreases as the radius of the cylinder increases. The intensities between $\phi = -\pi/2$ and $\phi = \pi/2$ scattered field becomes negligible, and incident wave determines the resultant field.

In Fig. 5, $\phi_0 = \pi/3$, $a = 3\lambda$, and $\theta = \pi/6$ are taken. Total scattered field is observed with respect to ϕ as the observation distance changes. Scattered field intensity tends to decrease with the increase in the observation distance.

In Fig. 6, total scattered field is plotted with respect to ϕ for two ϕ_0 values when a and θ are kept the same as for Fig. 5, $\rho = 10\lambda$ is taken. For $\phi \in [-\pi/4, \pi/4]$ and $\phi \in [3\pi/4, 5\pi/4]$ intervals, scattered field does not change when $\phi_0 = \pi/3$ is replaced by $\pi/4$. However, it
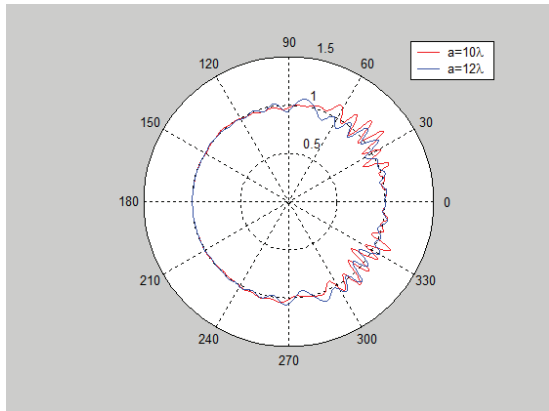
Fig. 4. Total scattered field variation for cylinder radius (*a*) values.
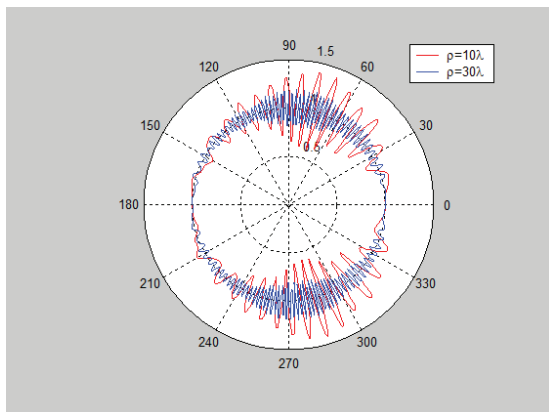
Fig. 5. Total scattered field variation according to observation distance ρ.
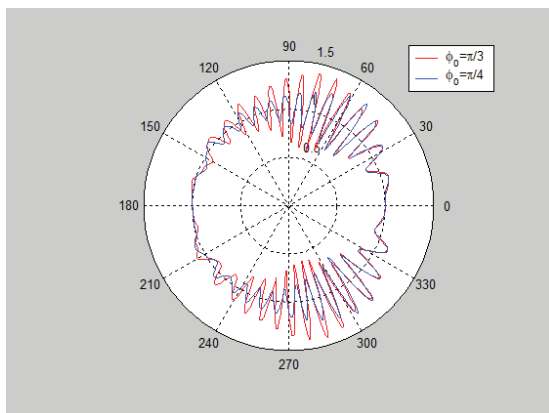
Fig. 6. Total scattered field variation according to angle of incidence ϕ_0.

is observed that for the intervals of $\phi \in [\pi/4, 3\pi/4]$ and $\phi \in [5\pi/4, 7\pi/4]$ field intensity at $\phi_0 = \pi/3$ decreases when ϕ_0 is replaced by $\pi/4$.

IV. CONCLUSION

In this work we obtained the exact physical optics (PO) surface current J_{PO} for a truncated conductive cylindrical cap by using the diffracted field expression for a conductive half plane. Diffracted field expression for the conductive half plane is obtained by employing the Malyughinetz solution which is used by Umul [11] to transform it to a PO integral for the diffraction problem of a truncated impedance cylinder. Ultimate scattered field is obtained by substituting the exact PO current J_{PO} into the scattering integral. Total scattered fields according to observation distance and radius of the cylinder cap are examined. It is concluded that for both parameters, total scattered field intensity approaches the intensity of incident plane wave as the observation distance or the cylinder radius increases. The intensity variation according to theta is observed as inversely proportional in some intervals of ϕ, and almost constant in other intervals. Finally, it is observed that as ϕ_0 increases, fringing in the intensity increases.

REFERENCES

[1] W. Franz and K. Klante, "Diffraction by surfaces of variable curvature," *IRE Transactions on Antennas and Propagation*, vol. 7, pp. 68-70, Dec. 1959.

[2] S. Hong, "Asymptotic theory of electromagnetic and acoustic diffraction by smooth convex surfaces of variable curvature," *Journal of Mathematical Physics*, vol. 8, no. 6, pp. 1223-1232, June 1967.

[3] E. Bahar, "Diffraction of electromagnetic waves by cylindrical structures characterized by variable curvature and surface impedance," *Journal of Mathematical Physics*, vol. 12, no. 2, pp. 186196, Feb. 1971.

[4] M. Idemen and L. B. Felsen, "Diffraction of a whispering gallery mode by the edge of a thin concave cylindrically curved surface," *IEEE Transactions on Antennas and Propagation*, vol. 29, no. 4, pp. 571-579, July 1981.

[5] M. Idemen and E. Erdogan, "Diffraction of the creeping waves generated on a perfectly conducting spherical scatterer by a ring source," *IEEE Transactions on Antennas and Propagation*, vol. 31, no. 5, pp. 776-784, Sep. 1983.

[6] A. H. Serbest, "Diffraction coefficients for a curved edge with soft and hard boundary conditions," *IEEE Proceedings*, vol. 131, no. 6, pp. 383-389, Dec. 1984.

[7] A. Buyukaksoy, "Diffraction coefficients related to cylindrically curved soft-hard surfaces," *Ann. Télécommun.*, vol. 40, no. 7, pp. 402-410, July 1985.

[8] T. B. Hansen and R. A. Shore, "Incremental length diffraction coefficients for the shadow boundary of

a convex cylinder," *IEEE Transactions on Antennas and Propagation*, vol. 46, no. 10, pp. 1458-1466, Oct. 1998.

[9] U. Yalcin, "Scattering from a cylindrical reflector: Modified theory of physical optics solution," *J. Opt. Soc. Am. A*, vol. 24, no. 2, pp. 502-506, Feb. 2007.

[10] Y. Z. Umul, "Scattering of a line source by a cylindrical parabolic impedance surface," *J. Opt. Soc. Am. A*, vol. 25, no. 7, pp. 1652-1659, July 2008.

[11] Y. Z. Umul, "Physical optics theory for the diffraction of waves by impedance surfaces," *J. Opt. Soc. Am. A*, vol. 28, no. 2, pp. 255-262, Feb. 2011.

[12] I. V. Andronov, "Diffraction at an elliptical cylinder with a strongly prolate cross section," *Acoustical Physics*, vol. 60, no. 3, pp. 237-244, May 2014.

[13] I. V. Andronov and Y. A. Lavrov, "Scattering by an elliptic cylinder with a strongly elongated cross section," *Acoustical Physics*, vol. 61, no. 4, pp. 383-387, July 2015.

[14] H. D. Basdemir, "Scattering of inhomogeneous plane waves by a truncated cylindrical cap," *Journal of Modern Optics*, vol. 62, no. 19, pp. 1555-1560, May 2015.

[15] A. V. Shanin and A. I. Korolkov, "Boundary integral equation and the problem of diffraction by a curved surface for the parabolic equation of diffraction theory," *Journal of Mathematical Sciences*, vol. 226, no. 6, pp. 817-830, Nov. 2017.

[16] M. Kara, "Scattering of a plane wave by a cylindrical parabolic perfectly electric conducting reflector," *Optik*, vol. 127, no. 10, pp. 4531-4535, Jan. 2016.

[17] T. B. A. Senior, "Diffraction by a semi-infinite metallic sheet," *Proceedings of the Royal Society A: Mathematical, Physical and Engineering Sciences*, vol. 213, pp. 436-458, Mar. 1952.

[18] T. B. A. Senior, "Half plane edge diffraction," *Radio Sci.*, vol. 10, pp. 645-650, June 1975.

[19] T. B. A. Senior and J. L. Volakis, *Approximate Boundary Conditions in Electromagnetics*, London, The Institution of Electrical Engineers, 1995.

Mustafa Kara received the Ph.D. degree in electronics and communication engineering from Çankaya University, Ankara, Turkey in 2017. Since 2006 he has been at Ordu University, Ordu, Turkey, where he is currently the assistant professor with the School of Technical Sciences. His research interests include diffraction of plane waves by resistive half planes between isorefractive media, scattering of evanescent waves by a cylindrical parabolic reflector, scattering of inhomogeneous plane waves by a perfectly electric conducting half plane, and diffraction by an offset-fed parabolic reflector.
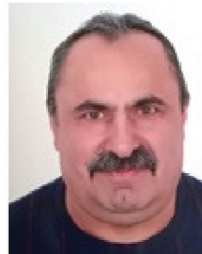
Mustafa Mutlu received his B.Sc. degree in Electrical-Electronic Engineering from the Karadeniz Technical University in 1990. He received an M.Sc. degree in Electrical-Electronic Engineering from the Karadeniz Technical University in 2010. He received a Ph.D. degree in Electrical-Electronic Engineering from the Ondokuz Mayıs University in 2021. He has been working at the Vocational School of Technical Sciences at Ordu University. His research interests include microstrip antennas, radio-TV systems, telecommunications, and RF circuits.

Synthesis of Elliptical Antenna Array using Hybrid SSWOA Algorithm

D. Prabhakar[1], K. Srinivas[2], S. Ratna Spandana[3], D. Anusha[4], M. V. Srikanth[5], and Y. Rama Krishna[1]

[1]Department of ECE
Seshadri Rao Gudlavalleru Engineering College (A), Seshadri Rao Knowledge Village, Gudlavalleru
Andhra Pradesh, 521356 India
prabhakar.dudla@gmail.com, yrk.gec@gmail.com

[2]Department of AI & DS
Seshadri Rao Gudlavalleru Engineering College (A), Seshadri Rao Knowledge Village, Gudlavalleru
Andhra Pradesh, 521356 India
kalyanapusrinivascse@gmail.com

[3]Department of ECE
Vijaya Institute of Technology for Women, Vijayawada, Andhra Pradesh, 521108 India
spandana.suriteti@gmail.com

[4]Department of E & I
V.R. Siddhartha Engineering College, Vijayawada, Andhra Pradesh, 520007 India
dasarianusha405@gmail.com

[5]Department of ECE
Usha Rama College of Engineering and Technology, Telaprolu, Andhra Pradesh, 521109 India
sree.02476@gmail.com

Abstract – In terms of research, the elliptical antenna arrays (EAA) synthesis is relatively novel. As it does not have to be circular in construction, this novel synthesis can maneuver the primary beam in the right direction, making it easier to realize. The amplitude and angular location of the ellipse, as well as the eccentricity of the ellipse, are all taken into account in the optimization process. The proposed hybrid algorithm is the SSWOA (Salp Swarm Whale Optimization Algorithm), which combines the Salp Swarm Optimization Algorithm (SSA) with the Whale Optimization Algorithm (WOA). The SSA algorithm serves as a guide, while the WOA algorithm serves as a helper in this method. We discover that optimization has a faster convergence time and high convergence accuracy when considering the benefits of SSA and WOA and applying them to the synthesis of antenna array layouts. If Griewank, Rosenbrock, Sphere, and Rastrigin test functions are used, it's worth noting that the hybrid method outperforms both WOA and SSA.

Index Terms – elliptical antenna array (EAA), Griewank, pattern synthesis, speed of convergence, sphere, rastrigin, Rosenbrock.

I. INTRODUCTION

The single antenna structure of antenna arrays gives it a great advantage in its wide usage, especiallyin defence applications, for example, sonar, radar, communication, and navigation systems. Higher levels of gain and directivity can be provided by these antenna arrays. Generally, the antenna arrays are categorized based on geometrical differences. Concentric circular, planar, linear, and circular, besides elliptical arrays, can be cited as specimens of these clusters. Nevertheless, in their research area, elliptical antenna arrays are comparatively novel [1–6]. Various means are adapted to synthesize the elliptical antenna arrays. The majority of this work is focused on linear and circular antenna arrays. Nevertheless, it is a widely known fact that elliptical antenna arrays possess radiation properties just like that of circular antenna arrays. The entire space is occupied by the elliptical antenna arrays because of their radiation pattern; furthermore, the primary beam of the array can be changed to the desired direction. Linear antenna, rectangular arrays, and elliptical antenna arrays should not be coupled together as the latter is less sensitive. This is because they lack the edge elements [7–8]. The elliptical antenna array (EAA) synthesis is the combination

of the position only, the amplitude only, or amplitude position techniques. Of these, the most used technique is the position only technique. In these three distinct algorithms namely the SADE, i.e., self-adaptive differential evolution, the BBO, i.e. Biogeography-Based Optimization, in addition to Firefly algorithms (FA),[4] are used to identify the optimal position of elements on the ellipse circumference which has the capacity of bringing down the maximum side lobe level (SLL) with fixed Beam Width between First Nulls (BWFN). The amplitude technique is explored by making use of the non-uniform current distribution, where the element position is stationary and cannot be changed. Further, by comparing BSA with BBO, FA, genetic algorithm (GA), and differential evolution(DE) the performance of thealgorithm is evaluated.

In this paper, EAA radiation synthesis is designed using a hybrid algorithm of SSWOA. The SSA, i.e., Salp Swarm Optimization combined with WOA, i.e., Whale Optimization Algorithm is a newly suggested algorithm. In this algorithm, the SSA algorithm acts as a guide while the WOA algorithm serves the role of an aid. With the aim of preventing a premature convergence and exploring wholly the problem of hyperspace, the leader updating the neighbour's best point is measured. Likewise, after the salps point updating, by employing WOA to improve the optimum searchability, the well-known point hasevolved. A combination of these algorithms enhances the diversity of the offspring,as well as maintaining the search-balance.

This paper is organized as follows:The presentation of the radiation synthesis model employing a hybrid algorithm of SSWOA for EAA is dealt with in section II. In section III the comparisons and numerical experiments on the EAA pattern synthesis are illustrated. Section IV offers the concluding section of this paper.

II. METHODOLOGYPROPOSED

This section proposes the hybrid algorithm of SSWOA for radiation pattern synthesis of the EAA. The algorithm of SSWOA being proposed is a blend of WOA as well as SSA. In this, the SSA algorithm effactually guides the evolution, while the WOA algorithm serves as the assistant's role. With a view to averting an untimely convergence and with the view to fully exploring the problem in hyperspace, the leader updating the best position is wellthoughtout. A unique function is used to govern the algorithm proposed as a continuation of the above. An elaborative procedure of the algorithm being proposed is clearly explained in the following subsection.

A. The SSWOA algorithm

The SSWOA method is described and used in this part to create patterns for elliptical antenna arrays. It is thought of as a global optimization problem,

$$\min \quad f(X) = f(X_1, X_2, X_3, \ldots, X_d);$$
$$for \quad X_i^{\min} \leq X_i \leq X_i^{\max}, \qquad (1)$$

where $i = 1, 2, 3, \ldots, d$ the number of optimized variables denoted as $dX_i^{\max}$ is the higher bound and $X_i^{\min}$ is the lower bound of X_i respectively.

As suggested in 2017 by Mirjalili [9], SSA is a new type of algorithm for resolving single-objective as well as multi-issues. The main motivation for the SSA is the swarming behaviour of salps when voyaging or foraging in the oceans. Finally, this SSA produces accurate and the best possible or even near-optimal arrangements in the optimization process. Particularly in this investigation, to give the optimal result competently, the investigative behaviour of SSA is increased by WOA [10–11]. The WOA is a natural and meta-heuristic optimization algorithm, which is deduced from characteristics of humpback whales. The following steps delineate the complete process of the hybrid algorithm suggested.

Stage 1: Initiating

In the initial stage of the SSA, the places of the salps are arbitrarily instated in the dimensional space which is communicated as,

$$X_i = rand * (X_i^{max} - X_i^{min}) + L_i \quad for \ i = 1, 2, 3 \ldots \ldots d. \qquad (2)$$

Stage 2: Appraisal

In this step, the suitability of each explore agent is appraised. The subsequent equation provides the vital objective function,

$$fitness = \min\{f(X)\}. \qquad (3)$$

Stage 3: The procedure of search employing

Layer 1: Explorative Stage (searching for quarry)

In the Explorative Stage, the location of a search agent gets modernized.

$$B = |\overrightarrow{c} \cdot X_{rand}(i) - X(i)|, \qquad (4)$$

$$X(i+1) = X_{rand}(i) - \overrightarrow{d} \cdot B. \qquad (5)$$

The probing extract in equations (4) and (5) and by the shrinking system the encompassing quarry in equations (6) and (7) are employed if $\overrightarrow{d}. \geq 1$.

Layer 2: Encompassing quarry

To discover an optimal solution proficiently, the probing performance of the SSA is boosted by the WOA, by the subsequent equation.

$$B = |\overrightarrow{c} \cdot X^* - X|, \qquad (6)$$
$$X(i+1) = X^* - \overrightarrow{d} \cdot B, \qquad (7)$$

where, $\overrightarrow{c}$ and $\overrightarrow{d}$ are considered as vector coefficients, and I as current iteration, the finest value of location

Fig. 1. Steps of proposed SSWOA algorithm.

B. Elliptical antenna array (EAA) pattern synthesis array factor formulation

In this subsection, the geometry of EAA and the corresponding AF are explored, leading to array optimization in the following subsections. The EAA is a kind of antenna array in which the elements of the antenna are placed at the boundary of an ellipse. Figure 2 illustrates an instance of N-element EAA lying in the x-y plane and has its midpoint positioned at the origin [12].
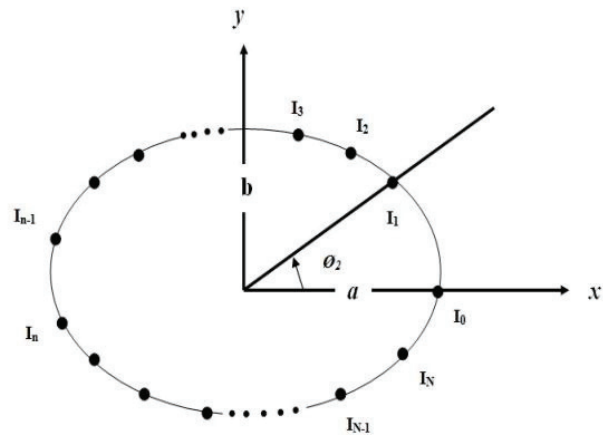
Fig. 2. N-element EAA.

Array factor for the EAA portrayed in Fig. 2 is given by:

$$\text{AF}(\theta,\varnothing) = \sum_{(n=1)}^{N} I_n \exp(j[k\sin(\theta)](a\cos(\varnothing_n)\cos(\varnothing) + b\sin(\varnothing_n)\sin(\varnothing) + \alpha_n]). \quad (11)$$

Where:

a is the semi-major axis of the ellipse
b is the semi-minor axis of the ellipse
I_n is excitation amplitude of nth element
$k=2\pi/\lambda$ (wave number)
θ is Elevation angle
$\varnothing_n$ is angular position of the nth element,

$$\varnothing_n = \frac{2\pi(n-1)}{N}$$

$\varnothing$ is azimuth angle
α_n is excitation phase of the nth element

$$\alpha\_n = k\sin(\theta 0)(a\cos(\varnothing n)\cos(\varnothing 0 + b\sin(\varnothing n)\sin[(\varnothing 0)]. \quad (12)$$

The eccentricity (e) of the ellipse is,

$$e = \sqrt{1 - \frac{b^2}{a^2}}. \quad (13)$$

If the e lies between 0 and 1, when e is '0' then e becomes a circle, when e is '1', then it becomes a line.
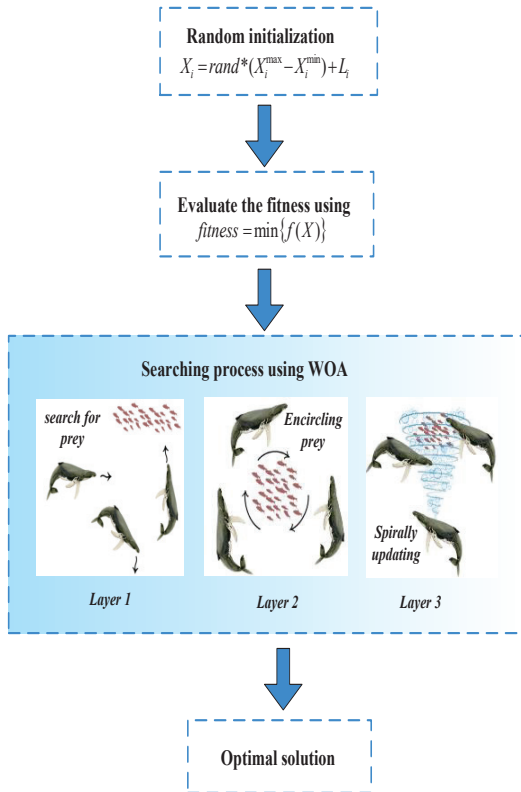
vector up to now is symbolized like X^* and X denotes the location vector.

The vector coefficients $\overrightarrow{c}$ and $\overrightarrow{a}$ are expressed as,

$$\overrightarrow{c} = 2R, \quad (8)$$

$$\overrightarrow{a} = 2A \times (R - A). \quad (9)$$

At this juncture, the random numeral in the middle of [0, 1] is specified like R and the changeable A is linearly diminishing as of [2-0].

Layer 3: Location apprising

The updating spiral location is represented as,

$$X(i+1) = \begin{cases} X_{rand}(i) - \overrightarrow{a} \cdot B; & if\ P < 0.5 \\ B \cdot e^{hl}\cos(2\pi l) + X_{rand}(i); & if\ P \geq 0.5 \end{cases}, \quad (10)$$

where the constant for portraying the spiral shape has been designated as h, the random numeral between [0, 1] is designated as P and l is [-1, 1].

Step 4: Termination procedure

When the procedure is accomplished, the projected technique chooses the optimum result or as well comes flip side to step 2. Figure 1 displays the steps of the projected hybrid algorithm of SSWOA. Thus, the grouping of SSA and WOA algorithms improves the variety of the progeny. Likewise, the desired search ability of the algorithm is heightened.

C. Radiation pattern synthesis using hybrid algorithm of SSWOA

Here, the radiation pattern synthesis of the array is discussed in detail to show the suggested hybrid algorithm. The array pattern is obtained through the superposition rule, where the radiation pattern of all active elements is extracted and stored. Several sub-goals put together are the primary objectives of the antenna array design to insert various objectives into one fitness function. This fitness function may be defined as,

$$\text{Fitness function} = F_{f1} + F_{f2} + F_{f3} + F_{f4} + F_{ff} + F_{f6}. \tag{14}$$

At this point,

$$F_{f1} = |\phi_0 - \phi_d|, \tag{15}$$

$$F_{f2} = |\theta_0 - \theta_d|, \tag{16}$$

$$F_{f3} = \begin{cases} |g - g_d| & ; \, if \, g \leq g_d \\ 0 & ; \, if \, g > g_d \end{cases}, \tag{17}$$

$$F_{f4} = \begin{cases} |MSL_L - SL_{L_d}| & ; \, if \, MSL_L \geq SL_{L_d} \\ 0 & ; \, if \, MSL_L < SL_{L_d} \end{cases}, \tag{18}$$

$$F_{f5} = \begin{cases} |NUL_L - NUL_{L_d}| & ; \, if \, NUL_L \leq NUL_{L_d} \\ 0 & ; \, if \, NUL_L > NUL_{L_d} \end{cases} \tag{19}$$

$$F_{f6} = \begin{cases} |HP_{BW} - HP_{BWd}| & ; \, if \, HP_{BW} \geq HP_{BWd} \\ 0 & ; \, if \, HP_{BW} < HP_{BWd} \end{cases} \tag{20}$$

The subsequent section displays the efficacy of the algorithm proposed with some numerical experimentation.

III. NUMERICAL RESULTS AND DISCUSSION

In this part, the adequacy of the projected calculation is checked to employ certain test capacities. At this point, we utilized four test capacities and these are utilized as central capacities for advancement techniques like the SSA besides the WOA. The capacities are clarified as follows,

$$Sphere_{(F_1(x))} = \sum_{i=1}^{N} X_i^2;$$

$$for \, |X_i| \leq 100, \tag{21}$$

$$Rosenbrock_{(F_3(x))} = \sum_{i=1}^{N-1} \left[100(X_{i+1} - X_i^2)^2 + (1 - X_i)^2 \right];$$

$$for \, |X_i| \leq 30, \tag{22}$$

$$Rastrigin_{(F_4(x))} = \sum_{i=1}^{N} \left[X_i^2 - 10\cos(2\pi X_i) + 10 \right];$$

$$for \, |X_i| \leq 10, \tag{23}$$

$$Griewank_{(F_2(x))} = \left\{ 1/4000 \sum_{i=1}^{N} X_i^2 - \prod_{i=1}^{N} \cos(X_i / \sqrt{i}) + 1 \right\};$$

$$for \, |X_i| \leq 600. \tag{24}$$

For comparison, SSA, WOA and SSWOA are simulated by utilizing the mentioned four test functions in 3D dimensions. The fitness or cost estimation of the result is characterized as the calculated *F(X)*. The deviation curve of the cost value employing several iterations is revealed in Figs. 3–6.
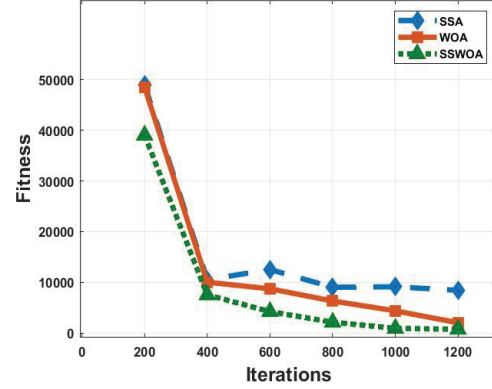

Fig. 3. The sphere function's average fitness value by way of diverse algorithms.
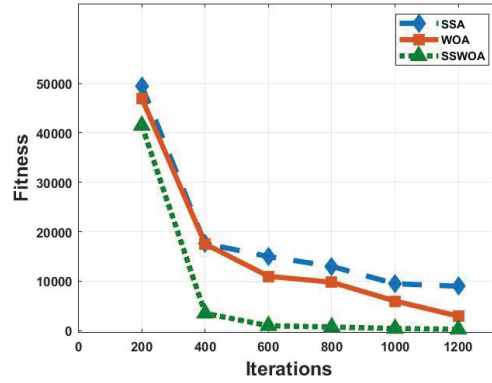

Fig. 4. The Griewank function's average fitness value employing diverse algorithms.
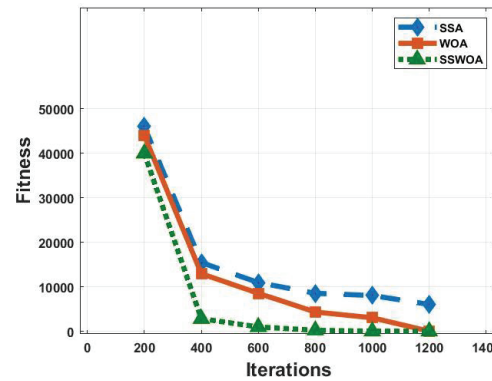

Fig. 5. The Rosenbrock function and its average fitness value employing several algorithms.
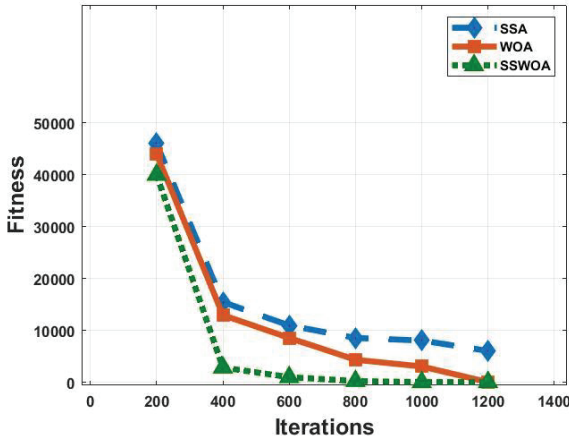
Fig. 6. Rastrigin function and itsaverage fitness value utilizing several algorithms.

For these algorithms, the population size is alike. Employing different kinds of algorithms, the average fitness value of the sphere function is revealed in Fig. 3. The cost values of the SSA, WOA, and SSWOA algorithms steadily decrease by employing raising iterations. As per the illustration, it can be detected and designed that hybrid SSWOA algorithm is better at 20.408%, 28.57%, 66.39%, 76.65%, 90.1%, 91.65% when compared with standard SSA and 19.58%, 24.99%, 66.39%, 76.65%, 99.01%, 91.65% when compared with standard WOA with the number of iterations.

The Griewank function's average fitness value with many iterations is illustrated in Fig. 4. It is understood from Fig. 4 that, when compared with standard SSA, the suggested hybrid method has lower fitness of 16.16%, 80.00%, 93.32%, 94.22%, 99.52%, 96.83%. While compared with WOA, the adopted hybrid method has lower fitness of 11.70%, 79.93%, 90.9%, 92.34%, 92.48%, and 90.34% with rising iteration. The simulated results show that the suggested hybrid method is superior to the single algorithm and has a much better balance between exploitation and exploration ability.

The Rosenbrock function's average fitness value is displayed in Fig. 5 by making use of many algorithms. The projected technique has a healthier fitness value of 13.04%, 81.28%, 90.44%, 99.6%, 98.87%, 98.53% and 9.09%, 77.69%, 87.78%, 93.16%, 97.06%, 1.10% as compared with standard SSA and WOA. Figure 6 shows the average fitness value of the Rastrigin function. While we compare it by standard SSA and WOA, the suggested method evinces superior fitness value of 41.49%, 45.16%, 58.16%, 73.14%, 94.09%, 91.68% and 37.94%, 40.48%, 55.99%, 69.68%, 93.135%, 89.14%.

Figure 7 illustrates the antenna's gain curve across various frequencies when employing different algorithms. Meanwhile, Fig. 8 showcases the reflection coefficient s_{11} under diverse phase angles, each assessed through various algorithms. Based on these graphical representations, it becomes evident that the proposed hybrid algorithm outperforms both SSA and WOA.

From the obtained results, it is clearly shown that the hybrid algorithm proposed has more energetic investigating capability and quicker convergence speed when it is compared with the standard of the SSA or the WOA. Figures 9 and 10 clearly show how the excitation amplitude and phase of the element are obtained by using SSWOA.

Fig. 7. The performance comparisons of the pattern of gain utilizing diverse algorithms.
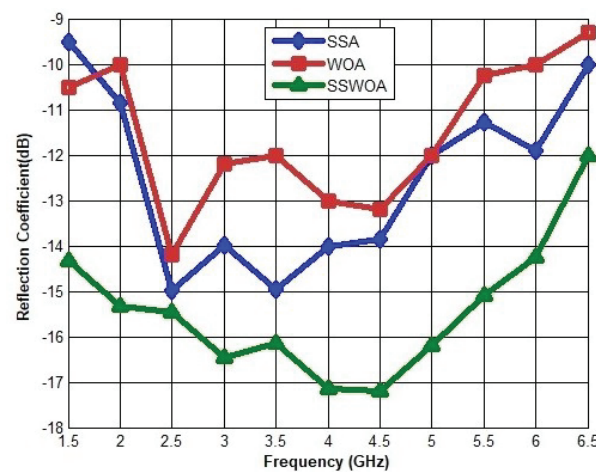
Fig. 8. The performance comparisons of the reflection coefficient S_{11} (dB) utilizing diverse algorithms.

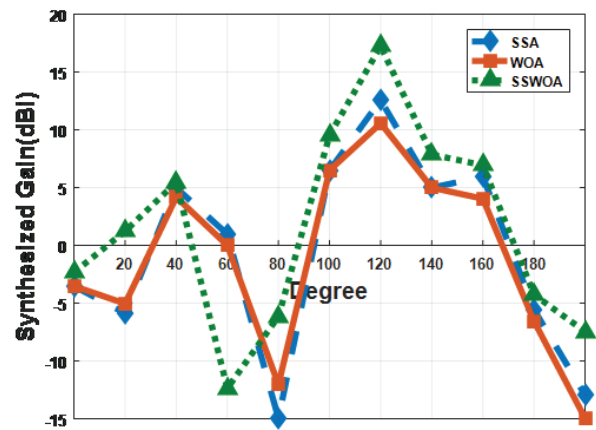Table 1: Comparison table from existing works

Author	Algorithms	Iterations	Fitness	Angle
Sharaqa and Dib [4]	Self-Adaptive Differential Evolution (SADE)	800	NR	300
Sharaqa and Dib [4]	Biogeography-Based Optimization (BBO)	800	NR	300
Sharaqa and Dib [4]	Firefly Algorithm (FA)	800	NR	300
Guney et al. [8]	Backtracking Search (BSA)	1400	NR	300
Khodier [12]	Cuckoo	300	10	300
Proposed	SSWOA	1200	800	NR

NR-Not Reported
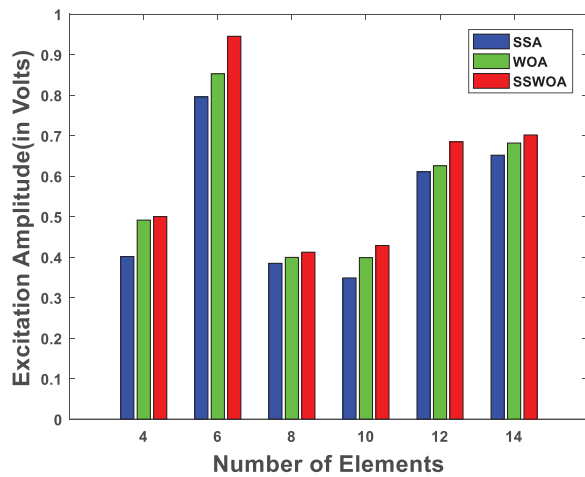
Fig. 9. Amplitude excitation using SSWOA.
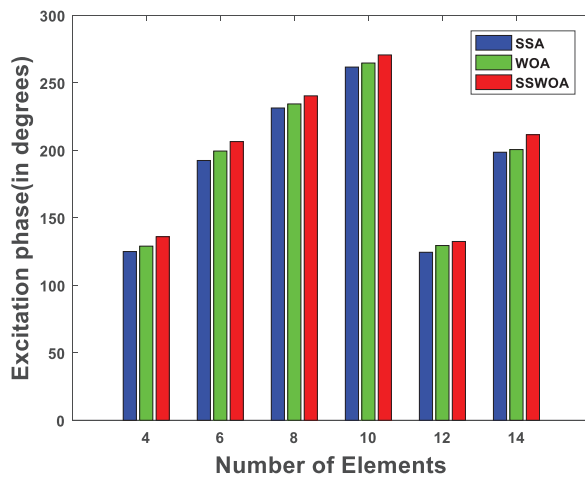
Fig. 10. Phase excitation using SSWOA.

IV. CONCLUSION

It may be stated that a hybrid SSWOA optimization algorithm can be suggested for the radiation pattern syn-thesis of EEA. The above-suggested method only needs simple mathematical processing. Moreover, it is effec-tive to put into practice. In EEA pattern synthesis, the numerical results do demonstrate that the suggested algo-rithm is efficient and achieves the best possible design with high accuracy as well as fast convergence swiftness. Further, the results show that the suggested technique performs better when it comes to the sphere, Rastrigin, Griewank, Rosenbrock, and test functions. The method proposed clearly shows a superior excitation amplitude and phase for a varying number of elements.

REFERENCES

[1] H. Yu and C.-W. Su, "Characteristics of fre-quency scanning elliptical array," *IEEE Antennas and Propagation Society Symposium Digest*, vol. 3, pp. 1416-1419, June 1991.

[2] A. A. Lotfi Neyestanak, M. Ghiamy, M. Naser-Moghaddasi, and R. A. Saadeghzadeh, "Investi-gation of hybrid elliptical antenna arrays," *IET Microwaves, Antennas & Propagation*, vol. 2, no. 1, pp. 28-34, 2008.

[3] R. A. Sadeghzadeh, A. A. Lotfi Neyestanak, M. Naser-Moghadasi, and M. Ghiamy, "A comparison of various hybrid elliptical antenna arrays," *Iranian Journal of Electrical and Computer Engineering*, vol. 7, no. 2, pp. 98-106, 2008.

[4] A. Sharaqa and N. Dib, "Position-only side lobe reduction of a uniformly excited elliptical antenna array using evolutionary algorithms," *IET Microwaves, Antennas & Propagation*, vol. 7, no. 6, pp. 452-457, 2013.

[5] A. Samanzare, "Elliptical antenna array pattern synthesis with fixed side lobe level and suitable main lobe beam width by genetic algorithm," *Majlesi Journal of Telecommunications Devices*, vol. 2, no. 1, pp. 1-8, 2013.

[6] A. Sharaqa and N. Dib, "Design of linear and elliptical antenna arrays using biogeography-based optimization," *Arabian Journal for Science and Engineering*, vol. 39, no. 4, pp. 2929-2939, 2014.

[7] R. J. Mailloux, *Phased Array Antenna Handbook*, Artech House, Boston, London, 2017.

[8] K. Guney and A. Durmus, "Elliptical antenna array synthesis using backtracking search optimisation algorithm," *Defence Science Journal*, vol. 66, no. 3, pp. 272-277, 2016.

[9] S. Mirjalili, A. H. Gandomi, S. Z. Mirjalili, and S. Saremi, "Salp Swarm Algorithm: A bio-inspired optimizer for engineering design problems," *Advances in Engineering Software*, vol. 114, pp. 163-191, 2017.

[10] S. Mirjalili and A. Lewis, "The whale optimization algorithm," *Advances in Engineering Software*, vol. 95, pp. 51-67, 2016.

[11] D. Prabhakar and M. Satyanarayana, "Sidelobe pattern synthesis using hybrid SSWOA algorithm for the conformal antenna array," *Engineering Science and Technology, an International Journal*, vol. 22, no. 6, pp. 1169-1174, Dec. 2019.

[12] M. Khodier, "Optimization of elliptical antenna arrays using the cuckoo search algorithm," *IEEE-APS Topical Conference on Antennas and Propagation in Wireless Communications (APWC)*, Spain, pp. 143-147, 2019.

Dudla Prabhakar completed his M.Tech. degree from Andhra University in 2003 and Ph. D. degree from Andhra University in 2017. He is currently working as an Associate Professor, in the Department of ECE, Seshadri Rao Gudlavalleru Engineering College (A), Gudlavalleru. His areas of research interest are EMI/EMC, Antenna Array Synthesis and Applied Electromagnetic applications. He has published papers in various journals/proceedings in the field of Antenna Arrays and EMI/EMC.

Kalyanapu Srinivas completed his M.Tech. and Ph.D. in Computer Science Engineering from Acharya Nagarjuna University, Guntur. Currently, he is head of department of AI&DS at Seshadri Rao Gudlavalleru Engineering College (A), Gudlavalleru. He has more than 40 publications in reputable international journals under his belt. He also has 4 patents to his credit. His areas of interest are Software Testing, Data Mining, AI, Machine Learning, Fuzzy Systems and Operating Systems.

S. Ratna Spandana completed her M.Tech. degree from JNTUK, Kakinada in 2021. She is currently working as an Assistant Professor, in the Department of ECE, Vijaya Institute of Technology for Women, Vijayawada. She is interested in the area of communication systems.

D. Anusha completed her M.Tech. in the specialization of embedded systems. She is currently working as an Assistant Professor in Velagapudi Ramakrishna Siddhartha Engineering College, Kanuru, Vijayawada. She is pursuing her Ph.D. from Puducherry Technological University, Puducherry.

M. V. Srikanth is a Research Scholar, pursuing a Ph.D. in the field of Image Processing from Jawaharlal Nehru Technological University, Kakinada, Andhra Pradesh, India. He is working as an Assistant Professor in the department of ECE, Usharama College of Engineering and Technology, Vijayawada.

Y. Ramakrishna received his Ph.D. in Smart Antennas from JNT University, Kakinada in 2015 and his Master's Degree in Microwave Engineering from Acharya Nagarjuna University, Guntur in 2005. He is working as a Professor at Seshadri Rao Gudlavalleru Engineering College, Gudlavalleru. His research interests include microwave antennas, optical communications, mobile communications and smart antennas.

Application of Artificial Neural Network Base Enhanced MLP Model for Scattering Parameter Prediction of Dual-band Helical Antenna

Ahmet Uluslu

Department of Electronics and Automation
Istanbul University-Cerrahpaşa, Istanbul, 34500, Turkey
auluslu@iuc.edu.tr

Abstract – Many design optimization problems have problems that seek fast, efficient and reliable based solutions. In such cases, artificial intelligence-based modeling is used to solve costly and complex problems. This study is based on the modeling of a multiband helical antenna using the Latin hypercube sampling (LHS) method using a reduced data enhanced multilayer perceptron (eMLP). The proposed helical antenna is dual-band and has resonance frequencies of 2.4 GHz and 2.75 GHz. The enhanced structure of the artificial neural network (ANN) was tested using 4 different training algorithms and a maximum of 10 different MLP architectures to determine the most suitable model in a simple and quick way. Then, performance comparison with other ANN networks was made to confirm the success of the model. Considering the high cost of antenna simulations, it is clear that the proposed model will save a lot of time. In addition, thanks to the selected sampling model, a wide range of modeling can be done with minimum data. When the target and prediction data are compared, it is seen that these data overlap to a large extent. As a result of the study, it was seen that the ANN modeling and the 125 samples used, were as accurate as an electromagnetic (EM) simulator for other input parameters in a wide range selected.

Index Terms – ANN, design modeling, dual-band, enhanced algorithm, helical antenna.

I. INTRODUCTION

An antenna is the name given to a metal device or converter manufactured to receive radio waves [1]. There are many types such as dipole, monopole, microstrip, satellite, periodic and array antenna. Helical antennas consist of a coil with a constant pitch of turns placed on a cylindrical surface, fed by a special cable and connected to a conductive plane [2]. A result of this structure is that the antenna size can decrease. Today, mobile stations count for a large share among the places where helical antennas are widely used. The performance of the mobile station is directly dependent on the performance of the helical antenna. Helical antennas are often preferred in portable devices such as mobile phones because they occupy less space and have broadband. The helical antenna, originally designed by Kraus, was used to detect radiation [3]. Due to its broadband advantage, it has also been popular in satellite systems for a while. Helical antennas are available in various designs according to their usage areas [4–7]. In addition, studies on underwater communication are substantial [8–10]. Just like in mobile phones, 2.4 GHz radio frequency is used in underwater applications [11–13]. In recent years, artificial intelligence (AI) algorithms have been used in many high-performance circuit designs. They have been frequently used in many different microwave circuit designs [14], such as unit cell models [15–16] for large-scale reflective array antenna designs and modeling of microstrip transmission lines [17–18]. In a few recent studies, there are AI-based models of antennas [19–20]. The first of these studies was carried out for the capacitive feed antenna [19]. The total number of samples in the study is 51,300. In the other study, modeling of microstrip antenna was discussed [20]. However, in this study, basing the gap width and number of steps on user preference increased the total number of samples used, causing it to be 18,450. Normally, the desired features of antenna design are obtained by experimentation. However, this method is quite costly when the antenna simulation time is taken into account. In the study, the solution of the design optimization problem of a dual-band helical antenna with an elliptical geometric structure, which has pioneered many design problems, is proposed using a fast, efficient, accurate and reliable based model with a low cost. MATLAB 2021a program was used for antenna electromagnetic (EM) simulations. An artificial neural network (ANN) model is designed to predict the variation of the S_{11} (dB) parameter of a helical antenna with resonance frequencies of 2.4 GHz and 2.75 GHz along the frequency band determined in different sizes.

In section II of the study, the parameters for the design of the helical antenna will be analyzed. In section III the data reduction with the Latin hypercube sampling (LHS) method and the details of the proposed network model will be discussed. In section IV the results of the study will be presented and the performance comparison with different ANN networks will be given. In section V, the paper will be concluded with evaluations and suggestions on the overall study.

II. DESIGN PROCESS OF HELICAL ANTENNA

Helical antennas have a circular polarization feature preferred in broadband VHF and UHF bands. In short, it can be defined as the practical configuration of the EM radiator. It consists of a coil of pipe or a thick copper wire wound like the thread of a screw. Most of the time the helix is resting on a base as shown in Fig. 1. The parameters used to define the helical antenna geometry are given in Table 1 along with their definitions and design used values.
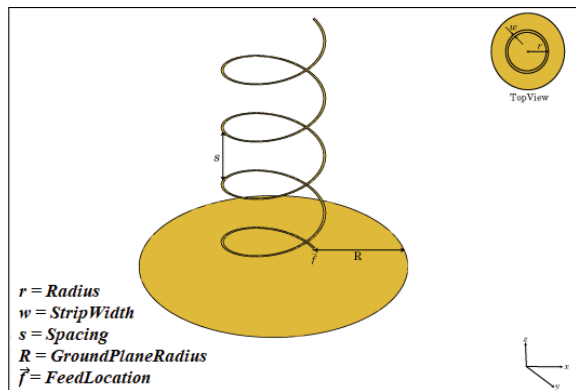

Fig. 1. Physical parameters of helical antenna.

Table 1: Helix design parameters

Parameter	Value	Definition
Radius	-	Radius of turns
Width	-	Strip width
Turns	-	Number of turns of helix
Spacing	35 (mm)	Spacing between turns
Winding Direction	CW	Direction of helix turns (windings)
Ground Plane Radius	75 (mm)	Ground plane radius
Feed Stub Height	1.0000e-03 (m)	Feeding stub height from ground
Conductor	PEC	Type of metal material

III. PROPOSED METHOD
A. Dataset reduction using the Latin hypercube sampling method

ANNs can be trained due to their structure. They keep the data obtained during training as the connection weight between nerve cells. This process can also be defined as the determination of connection weights. These weights store the information that will be needed during the calculation of the test data of the network [21]. It is ensured that the training cost is very low in order for the network to determine the most optimal connection weights. Here, the low rate of error in the test result is directly proportional to the training error. Therefore, the training error should be kept low as a priority. Here, the data set selection is of great importance. Input parameter ranges to be used to determine the optimum results of the network in the desired frequency band range have been determined based on the optimization study carried out in the case studies [22–23]. In these studies, the design of the helical antenna with optimization algorithms was discussed [22–23]. However, as it is well known, optimization processes are both costly and long-term processes. Therefore, in many studies, the modeling process with the optimum data set gives results in a short time as well as its low cost. Here, data reduction is among the methods frequently used in such applications to further reduce the cost. For this reason, using a sampling technique called LHS, the widest range of data set was extracted. LHS is a popular stratified sampling technique first proposed by MacKay [24] and further developed by Iman and Conover [25]. It is a sampling method of random designs that try to be evenly distributed in the design space. With the LHS, one must first decide how many sample points to use, and remember in which row and column the sample point is taken for each sample point. This configuration is similar to having N rooks on a chessboard without threatening each other [24–25]. Training models in deep learning can be divided into 3 classes in general. These are named as underfit model, overfit model and good fit model. Of these, the overfit model that learns the training dataset very well, performs well in the training dataset, but cannot perform well in the test sample. This common overfitting issue was overcome by choosing the LHS model.

Here, 3 different design parameters of a dual band helical antenna are extracted in the intervals and number of samples indicated in Table 2. In addition, a total of 100 frequency samples with equal step spacing in the 1.5-3.5 GHz band range were selected. All these processes were performed by a computer with 8th generation Intel Core i7 CPU, 3.20 GHz processor and 8 GB RAM.

Table 2: Test and training data sets

Parameter	Range	Sampling Method	Number of Samples
Radius (r) (mm)	20–30	Latin hypercube	5
Width (w) (mm)	1–4	Latin hypercube	5
Turns (t)	1–4	Latin hypercube	5
Frequency (GHz)	1.5–3.5	Linear	100
Total Sample (number of samples X frequency)	-	-	125x100

B. eMLP model

ANNs are frequently encountered in design problems because of their successful performance. Multilayer perceptron (MLP) neural network is one of the most popular among ANNs. The choice of training algorithm type (*trainlm*, *trainbr* etc. [27–30]) and architecture (number of hidden layers and neurons) used in the problems solved using this network model is one of the most important points. It is very difficult to predict which of these choices will be closer to the target. There are various studies on this subject [31–35]. A new trained constructive model has been proposed to obtain the minimum mean error value with optimum cost by training ANNs [36]. Here, this suggestion is further developed, using a small number of models and a certain number of hidden layers and neurons. In the study, mean error values are recorded throughout the learning process. When this value does not catch a new decrease during the training period, it is concluded that the network has reached saturation. At the same time, other architectural results are recorded and the threshold value is determined. According to this threshold value, the model determines how many MLP architectures it will create in total for each training algorithm. In addition, the maximum value for the architecture experiment is determined by the user. For each architecture, the number of hidden layers and neurons is automatically adjusted according to the average error value of the algorithm. This enhanced multilayer perceptron (eMLP) model provides great convenience for the user compared to the standard architecture [31–32], [36–37].

In this designed eMLP model, first the model parameters are set. These are the training algorithm types to be used: *trainbr*, *trainlm* etc. [26–30]. MLP architecture consists of parameters such as the number of hidden layers, the number of neurons to be used in the hidden layers, and the maximum number of architectural trials. In the next process, the modeling process is started for the determined training algorithms and architectures.

Mean absolute error (MAE)/Mean squared error (MSE)'s generated as a result of each modeling process are recorded. The system compares the MSE ratio with the previous result and decides whether to continue with the new architecture. In short, it is expected to reach saturation. This process is repeated separately for each training algorithm set at the beginning. As a result of all these processes, the training algorithm/architecture with the minimum MSE is accepted as the best model. All these steps are presented in Fig. 2 as a flow chart. In addition, the black box model of the ANN is shown in Fig. 3.

MSE and MAE can be counted among the main performance indicators used in the performance evaluations of ANN and machine learning (ML) methods [20], [35]. MSE gives an absolute number of how much the predicted results differ from the actual number. Not much insight can be interpreted from a single result, but it gives a real number to compare with other model
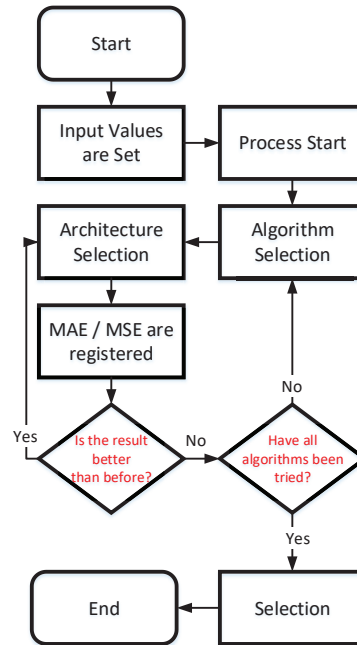

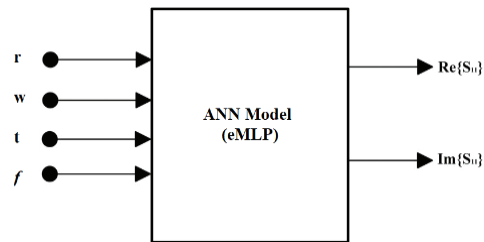Fig. 2. Flow chart of the modeling process for eMLP.

Fig. 3. ANN model for training the S_{11} (dB) parameter of the helical antenna.

results and helps with the choice of the best regression model. The MAE sums the absolute error value, a more direct representation of the sum of the error terms. It is more suitable for comparing the results of other studies with or without normalization. In the study, both performance evaluation results are given as a table.

For the proposed model for each mean error value the training depends on two parameters: algorithm type and architecture (hidden layer counts and neuron counts). The purpose of this model is to find the result with the best mean error simply and quickly.

IV. CASE STUDY

The study consists of three main parts. The first stage includes the study results for the training algorithms/architectures determined for the proposed eMLP model. Here, the most successful training algorithm/architecture is determined, and the second step is to compare the performance of the proposed model with other ANN models. As a final step, in order to reveal that the study is applicable in real life, a design was made with a selected model using the 3D EM simulation tool CST program.

A. Experimental work for eMLP

In this part of the study, a multi-band helical antenna design with 3 different design parameters based on eMLP, and modeling in the 1.5-3.5 GHz band will be studied. The proposed antenna has dual bands with resonance frequencies of 2.4 GHz and 2.75 GHz. Based on the helical antenna ANN model in Fig. 2, there are 3 input variables that will directly affect the output parameter S_{11} (dB). When frequency is added to these, there are a total of 4 input parameters specified in Table 2. In the study, firstly, the ranges for the design parameters are determined. Then, the input data set is created with the LHS method. S_{11} results for the selected input data set are determined with the help of an EM simulator. By combining all these data, half of the input/output data set is separated as training data and the other half as test data, and the modeling process is started using eMLP. As a result of all these operations, the model with the minimum average error is considered the optimal result. All this is presented as a flowchart in Fig. 4.

The MSE and MAE values for the training and test, which are the result of the study performed in line with the steps given in order as the flow chart in Fig. 4, are given numerically in Table 3. According to the results indicated in Table 3, it is seen that the increase in the number of hidden layers and neurons in the architecture increases the modeling time. When we compare the training algorithms with the same architecture in terms of modeling time, it is seen that the fastest training algorithm is '*trainrp*'. However, in architecture, it is seen that increasing the number of hidden layers and neurons does not always cause a decrease in the error
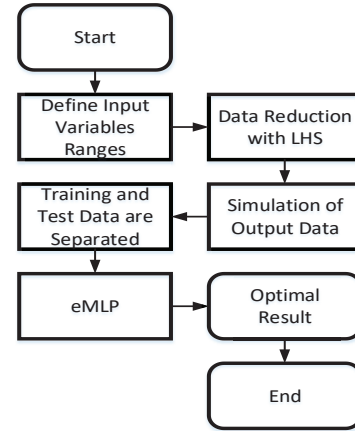

Fig. 4. Flow chart of modeling process of LHS and eMLP based helical antenna.

Table 3: General comparison of MAE and MSE based eMLP models

Training Algorithm	Architecture	Train Error (MSE)	Test Error (MSE)	Train Error (MAE)	Test Error (MAE)	Time (sec.)
trainbr	5 10	6.08	7.77	1.37	1.40	11.2
	10 15	6.08	7.77	1.37	1.40	21.7
	15 20	6.08	7.77	1.37	1.40	45.7
	5 10 15	0.12	97.6	0.24	0.66	26.7
	5 15 20	0.03	0.46	0.11	0.15	53.7
	10 15 20	0.02	1.34	0.09	0.18	72.4
	5 10 15 20	0.03	0.32	0.11	0.15	83.4
	10 10 15 20	**0.02**	**0.21**	**0.09**	**0.13**	**101.7**
	10 15 15 20	0.01	0.22	0.08	0.14	135.9
trainlm	5 10	0.69	1.18	0.51	0.55	9.6
	10 15	0.16	0.39	0.26	0.29	21.4
	15 20	0.03	0.22	0.12	0.16	41.5
	5 10 15	0.14	0.70	0.25	0.31	25.0
	5 10 15 20	0.02	0.44	0.09	0.16	47.2
	10 10 15 20	0.02	0.37	0.10	0.18	5.0
	10 15 15 20	0.01	0.84	0.08	0.16	13.9
trainrp	5 10	6.12	7.99	1.37	1.44	2.7
	10 15	6.05	7.76	1.36	1.38	3.4
	15 20	5.68	7.39	1.36	1.40	4.1
	5 10 15	6.00	7.68	1.35	1.38	4.0
	5 15 20	6.08	8.61	1.37	1.60	4.8
	10 15 20	2.80	4.10	0.91	0.96	5.2
trainscg	5 10	6.07	7.77	1.37	1.40	4.6
	10 15	6.06	7.77	1.37	1.41	6.0
	15 20	6.00	7.71	1.36	1.42	7.6
	5 10 15	6.07	7.77	1.37	1.40	7.3
	10 15 20	5.99	7.75	1.35	1.38	9.8
	5 10 15 20	6.08	7.78	1.37	1.40	11.2
	10 10 15 20	6.07	7.79	1.38	1.42	11.9
	10 15 15 20	3.02	5.15	0.97	1.16	12.9

rate. This situation varies according to the selected training algorithm. In addition, the importance of the eMLP model in finding the optimal architecture is clearly seen. In the study, a maximum of 10 different MLP architecture experiments were made for 4 different training algorithms. Here, it is appropriate to select 10 as the maximum value, since the modeling is terminated before reaching 10 different trials for each training algorithm. As a result of the study, values with a lower error were obtained as a result of modeling with the

'*trainbr*' training algorithm. In the '*trainbr*' training algorithm, which has the most successful results, it is seen that it has a 4 hidden layer MLP architecture with '10-10-15-20' neurons. The results obtained as a result of this most successful model are given graphically in Figs. 5 (a), (b) and (c) as the variation of S_{11} (dB)
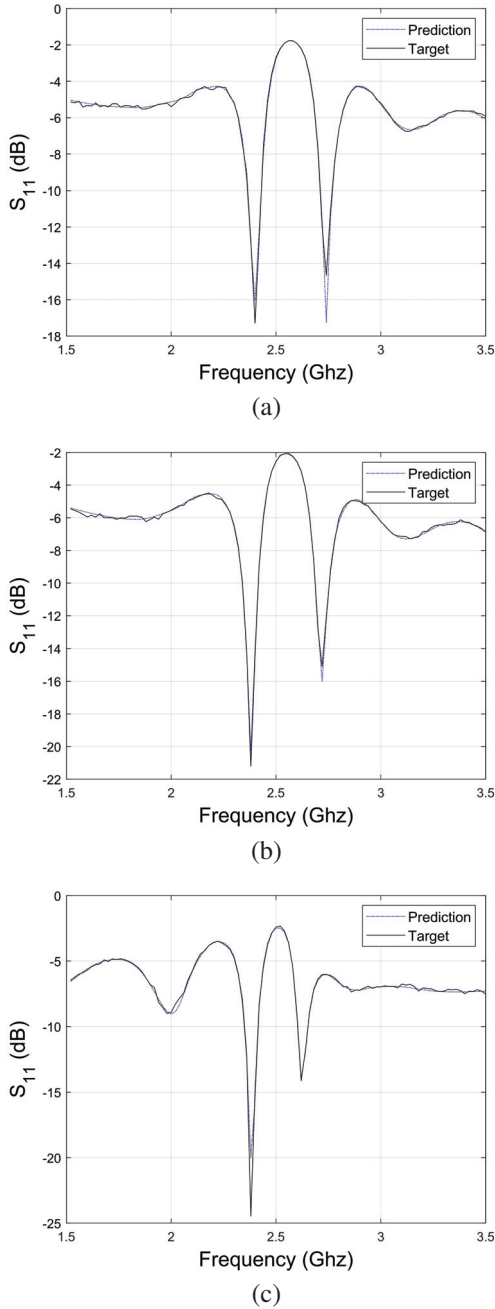
with frequency as target and prediction data. As can be seen from the graphics, a high success rate has been achieved.

B. Performance comparison with other ANN models

Of course, these very low error rates obtained from the study do not directly confirm the success of the study. In order to support the success of the proposed model, performance comparisons were made with other widely used ANNs. Here, modeling studies were carried out with 3 different neural networks apart from eMLP. Since the radial basis (RB) model does not take any input parameters, it is used directly. In the radial basis function (RBF) and general regression neural network (GRNN) models, experiments were made for different spread parameters, and the result with the lowest error was selected. The most successful results obtained are graphically presented as the variation of S_{11} (dB) with frequency in Figs. 6 (a), (b) and (c) for 4 different ANNs. In addition, error rates and time are given numerically in Table 4. As can be seen from the results, the closest results to the target line were obtained with the eMLP model. Although GRNN is lower in time cost, this situation can be ignored since it is in the order of seconds.

Table 4: Performance comparison of ANN models based on MEA/MSE

ANN	Train Error (MSE)	Test Error (MSE)	Train Error (MAE)	Test Error (MAE)	Time (sec.)
GRNN	1.16	1.77	0.67	0.70	94.2
RBE	1.80	3.85	0.79	1.00	168.7
RB	3.40	4.66	1.04	1.10	192.4
eMLP	**0.02**	**0.21**	**0.09**	**0.13**	**101.7**

(a)

(b)

(c)

Fig. 5. eMLP model performance parameter of return loss (S_{11}) for antenna: (a) r=27 (mm), w=1.5 (mm), t=2.6, (b) r=27 (mm), w=2 (mm), t=2.6, and (c) r=27 (mm), w=2.5 (mm), t=3.3.
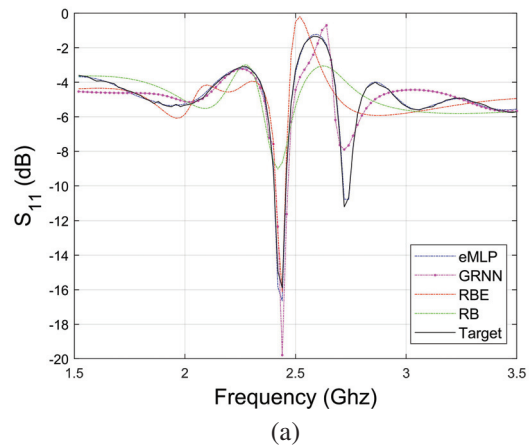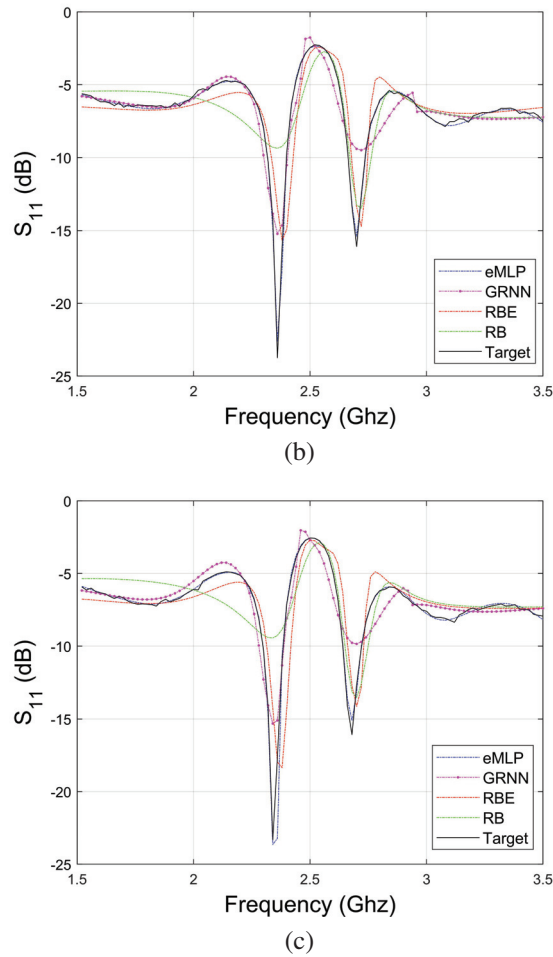

(a)

Fig. 6. *Continued*

(b)

(c)

Fig. 6. Comparison of different ANN model performance parameter of the return loss (S_{11}) of the antenna: (a) r=27 (mm), w=1 (mm), t=2.95, (b) r=27 (mm), w=2.5 (mm), t=2.6, and (c) r=27 (mm), w=3 (mm), t=2.60.

C. Simulation verification with 3D design program

One of the most successful results was selected and modeled in the 3D EM simulation tool CST microwave studio program. The results from the EM program show that the gain is 11.9 dB for 2.4 GHz and 9.81 dB for 2.75 GHz. Also, the far field gain for 2.4 GHz and 2.75 GHz is shown in Figs. 7 (a) and (b), respectively. The similarity of the simulation results revealed that this antenna is applicable to the real error. In addition, the antenna simulation time takes an average of 45-50 seconds for 1 sample. If it is calculated that the modeling process is done for 62 samples, this time is approximately 50 minutes. In the eMLP model, this process can be done in about 102 seconds.
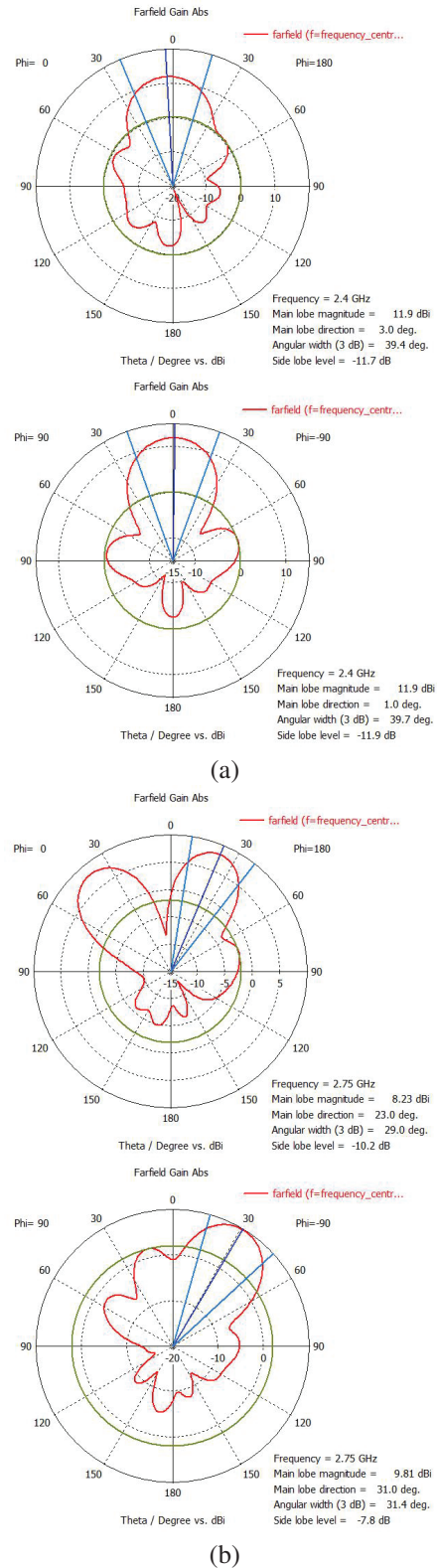

(a)

(b)

Fig. 7. Farfield gain of helical antenna for (a) 2.4 GHz and (b) 2.75 GHz.

V. CONCLUSIONS

Here, a fast, accurate and reliable solution to the design problem, which is very costly for antenna designers, is provided by using the proposed eMLP model for multi-band helical antenna design. Return loss (S_{11}) of less than -10 dB was observed throughout the process at approximately 2.4 and 2.75 GHz resonance frequencies. Data reduction was made by using the LHS method in the selection of the data set. Thus, the total number of samples was kept to a minimum. Successful results were obtained with the proposed eMLP model using this data set. To confirm this success, performance comparisons of different ANN types were made. With this method, the very costly trial-and-error method, used in antenna design, is obsolete. In addition, instead of starting the design with a standard geometry, starting with optimized value ranges from a previous study enabled the problem to achieve clearer results. In addition, the design created in the CST program was used to compare the MATLAB results with another 3D EM simulation tool which revealed that it is applicable in real life. Therefore, as a result of the study, it has been seen that the proposed model is both more economical in terms of calculation and as accurate and safe as the EM simulator in the design of the dual band helical antenna. In addition, the proposed model is not limited to the helical antenna, the model can also be successfully applied to other design optimization problems by changing the network model.

REFERENCES

[1] C. A. Balanis, *Antenna Theory: Analysis and Design*, 3rd ed. New Jersey, John Wiley & Sons, 2005.

[2] Y. Liang, J. Zhang, Q. Liu, and X. Li, "High-power dual-branch helical antenna," *IEEE Antennas and Wireless Propagation Letters*, vol. 17, no. 3, pp. 472-475, Mar. 2018

[3] J. D. Kraus, *Antennas*, 2nd ed. McGraw-Hill College, Mar. 1988.

[4] X. Tang and J. Zhang, "A strip-helical dipole antenna with wide bandwidth and high gain," *International Symposium on Antennas and Propagation (ISAP)*, Okinawa, Japan, pp. 82-83, Oct. 2016.

[5] S. I. H. Shah, S. Gosh, M. M. Tentzeris, and S. Lim, "A novel bio inspired pattern reconfigurable quasi-yagi helical antenna using origami DNA," *International Symposium on Antennas and Propagation (ISAP)*, Busan, Korea (South), pp. 1-2, Oct. 2018.

[6] S. H. Eedala, S. Elakiyaa, R. Nethra, R. Asha, and M. Jayakumar, "Design of helical array antenna based ground terminal for satellite communication on the move," *4th International Conference on Electronics, Communication and Aerospace Technology (ICECA)*, Coimbatore, India, pp. 559-563, Nov. 2020.

[7] F. Hyjazie, W. Tong, and H. Boutayeb, "Multi/wide band printed quad helical antenna," *IEEE International Symposium on Antennas and Propagation and North American Radio Science Meeting*, Montreal, QC, Canada, pp. 1893-1894, July 2020.

[8] M. Barbeau, J. Garcia-Alfaro, E. Kranakis, and S. Porretta, "The sound of communication in underwater," *Ad Hoc Networks*, vol. 223, pp. 13-23, Jan. 2018.

[9] I. F. Akyildiz, D. Pompili, and T. Melodia, "Underwater acoustic sensor networks: Research challenges," *Hindawi*, vol. 3, no. 3, pp. 257-279, May 2005.

[10] M. Subha and K. S. Divya, "Technologies used in underwater wireless communication," *International Journal of Innovative Research in Computer and Communication Engineering*, vol. 5, no. 6, pp. 91-95, July 2017.

[11] A. N. Jaafar, H. Ja'afar, I. Pasya, Y. Yamada, R. Abdullah, M. A. Aris, and F. N. M. Redzwan, "Analysis of helical antenna for wireless application at 2.4 GHz," *IEEE Asia-Pacific Conference on Applied Electromagnetics (APACE)*, Melacca, Malaysia, pp. 1-5, Nov. 2019.

[12] N. Destria, M. Artiyasa, S. Gumilar, R. Azhari, A. Badrudin, M. A. Maulidan, and J. A. Pradiftha, "Design of 2.4 GHz helix antenna for increasing wifi signal strength using managal and wirelesmon application," *International Conference on Computing, Engineering, and Design (ICCED)*, Kuala Lumpur, Malaysia, pp. 1-5, Nov. 2017.

[13] M. Márton, Ľ. Ovseník, J. Turán, M. Špes, and J. Urbanský, "Comparison of helix antennas operated on 2.4, 5.2 and 9.2GHz for FSO/RF hybrid system," *29th International Conference Radioelektronika*, Pardubice, Czech Republic, pp. 1-4, Apr. 2019.

[14] F. Güneş, P. Mahouti, S. Demirel, M. A. Belen, and A. Uluslu, "Cost-effective GRNN-based modeling of microwave transistors with a reduced number of measurements," *International Journal of Numerical Modelling: Electronic Networks, Devices and Fields*, vol. 30, no. 3-4, Aug. 2017.

[15] F. Güneş, S. Demirel, and S. Nesil, "A novel design approach to X-band Minkowski reflectarray antennas using the full-wave EM simulation-based complete neural model with a hybrid GA-NM algorithm," *Radioengineering*, vol. 23, no. 1, pp. 144-153, Apr. 2014.

[16] P. Mahouti, F. Gunes, A. Caliskan, and M. A. Belen, "A novel design of non-uniform reflectarrays with symbolic regression and its realization using 3-D printer," *Applied Computational Electromagnetics Society (ACES) Journal*, vol. 34, no. 2, pp. 280-285, Feb. 2019.

[17] D. Krishna, J. Narayana, and D. Reddy, "ANN models for microstrip line synthesis and analysis," *World Academy of Science, Engineering and Technology, International Science Index 22, International Journal of Electrical, Computer, Energetic, Electronic and Communication Engineering*, vol. 2, no. 10, pp. 2343-234, Oct. 2008.

[18] P. Mahouti, F. Güneş, M. A. Belen, and S. Demirel, "Symbolic regression for derivation of an accurate analytical formulation using 'Big Data' an application example," *Applied Computational Electromagnetics Society (ACES) Journal*, vol. 32, no. 5, pp. 372-380, May 2017.

[19] N. Calik, M. A. Belen, and P. Mahouti, "Deep learning base modified MLP model for precise scattering parameter prediction of capacitive feed antenna," *International Journal of Numerical Modelling: Electronic Networks, Devices and Fields*, vol. 33, no. 2, Sep. 2019.

[20] P. Mahouti, "Design optimization of a pattern reconfigurable microstrip antenna using differential evolution and 3D EM simulation-based neural network model," *International Journal of RF and Microwave Computer-Aided Engineering*, vol. 29, no. 8, Aug. 2019.

[21] Z. Şen, *Yapay Sinir Ağları İlkeleri*, İstanbul, Su Vakfı Yayınları, 2004.

[22] M. Kalkancı and A. Günday, "Triangular bowtie antenna design and modelling," *Research & Reviews in Engineering*, Gece Publishing, May 2021.

[23] N. Timürtaş, "Honey Bee Mating Optimization About to Design Antennas," *Yıldız Teknik Üniversitesi / Fen Bilimleri Enstitüsü / Elektronik ve Haberleşme Mühendisliği Ana Bilim Dalı / Haberleşme Bilim Dalı*, Yıldız, 2018.

[24] M. MaKa, R. Beckman, and W. Conover, "A comparison of three methods for selecting values of input variables in the analysis of output from computer code," *Technimeterics*, vol. 21, no. 1, pp. 239-245, May 1979.

[25] R. Iman and W. Conover, "Small sample sensitivity analysis techniques for computer models, with an application to risk assessment," *Communications in Statistics-Theory and Methods*, vol. 9, no. 17, pp. 1749-1842, Jan. 1980.

[26] A. D. Anastasiadis, G. D. Magoulas, and M. N. Vrahatis, "New globally convergent training scheme based on the resilient propagation algorithm," *Neurocomputing*, vol. 64, pp. 253-270, Mar. 2005.

[27] D. J. C. MacKay, "Bayesian interpolation," *Neural Computation*, vol. 4, no. 3, pp. 415-447, May 1992.

[28] D. Pham and S. Sagiroglu, "Training multilayered perceptrons for pattern recognition: A comparative study of four training algorithms," *International Journal of Machine Tools and Manufacture*, vol. 41, no. 3, pp. 419-430, Feb. 2001.

[29] S. Ali and K. A. Smith, "On learning algorithm selection for classification," *Applied Soft Computing*, vol. 6, no. 2, pp. 119-138, Jan. 2006.

[30] F. D. Foresee and M. T. Hagan, "Gauss-Newton approximation to Bayesian learning," *Proceedings of International Conference on Neural Networks (ICNN'97),* Houston, TX, USA, pp. 1930-1935, June 1997.

[31] N. Çalik, M. A. Belen, P. Mahouti, and S. Koziel, "Accurate modeling of frequency selective surfaces using fully-connected regression model with automated architecture determination and parameter selection based on bayesian optimization," *IEEE Access,* vol. 9, pp. 38396-38410, 2021.

[32] S. Masmoudi, M. Frikha, M. Chtourou, and A. B. Hamida, "Efficient mlp constructive training algorithm using a neuron recruiting approach for isolated word recognition system," *International Journal of Speech Technology*, vol. 14, no. 1, pp. 1-10, Mar. 2011.

[33] W. B. Soltana, M. Ardabilian, L. Chen, and C. B. Amar, "A mixture of gated experts optimized using simulated annealing for 3d face recognition," *International Conference on Image Processing*, Brussels, Belgium, pp. 3037-3040, Sep. 2011.

[34] H. Boughrara, L. Chen, C. B. Amar, and M. Chtourou, "Face recognition under varying facial expression based on perceived facial images and local feature matching," *International Conference on Information Technology and e-Service*, Sousse, Tunisia, pp. 1-6, Mar. 2012.

[35] P. Mahouti, F. Güneş, S. Demirel, A. Uluslu, and M. A. Belen, "Efficient scattering parameter modeling of a microwave transistor using generalized regression neural network," *20th International Conference on Microwaves, Radar and Wireless Communications (MIKON)*, Gdansk, Poland, pp. 1-4, June 2014.

[36] H. Boughrara, M. Chtourou, and C. B. Amar, "Mlp neural network-based face recognition system using constructive training algorithm," *International Conference on Multimedia Computing and System ICMCS*, Tangiers, Morocco, pp. 233-238, May 2012.

[37] H. Boughrara, M. Chtourou, C. Amar, and L. Chen, "Face recognition based on perceived facial images and mlp neural network using constructive training algorithm," *IET Computer Vision Journal,* vol. 8, no. 6, pp. 729-739, Dec. 2014.

Ahmet Uluslu received his Ph.D. from Istanbul Yıldız Technical University Electronics and Communication Engineering Department in 2020. He completed his master's degree at the Department of Electromagnetic Fields and Microwave Techniques from the same university. He is currently working as an associate professor at Istanbul University-Cerrahpaşa Electronics and Automation Department. His current research areas are microwave circuits, especially optimization techniques of microwave circuits, antenna design optimization-modeling, surrogate-based optimization and artificial intelligence algorithm applications.

A Simple Interference and Power-based Direction of Arrival Measuring System for Modern Communication

Nga Vu[1,2†], Thinh Le[1,3†], Minh Dinh[1,4], and Minh Thuy Le[1*]

[1]School of Electrical and Electronic Engineering
Hanoi University of Science and Technology, 11515, Vietnam

[2]École normale supérieure Paris-Saclay
Université Paris-Saclay, 91190, France

[3]College of Engineering
University of North Texas, 76205, Texas, USA

[4]Department of Electrical and Computer Engineering
University of Southern California, 90089, California, USA
[*]Corresponding author: thuy.leminh@hust.edu.vn
[†]These authors contributed equally to the work.

Abstract – In this paper, we present a system specialized for measuring the direction-of-arrival (DoA) of electromagnetic waves with noticeable simplicity. Unlike common methods, which are based heavily on complex computation and signal processing, our proposed system is considerably simpler, both in terms of design and operating theory. Our design consists of two directional antennas for collecting incident waves, a system of Wilkinson power combiners and dividers in which the waves collected by the antennas interfere, a result-processing block consisting of power amplifiers, rectifiers, and a microcontroller unit that respectively converts the interferometric radio-frequency (RF) signal into direct-current (DC) signal, measures its corresponding power before calculating the incident angle solely based on a simple trigonometric equation. The system yields a high accuracy of less than 7.5^o with the incident angle ranging from -60° to 60°.

Index Terms – antennas, direction-of-arrival, interferometry, power amplifier, Wilkinson power divider.

I. INTRODUCTION

Measuring the direction-of-arrival (DoA) has attracted extensive concern from researchers since the first days of the microwave. In recent years, DoA estimation plays a crucial role due to its diverse application, especially in modern wireless communication. One well-known example that needs DoA measurement is wireless power transfer (WPT) in which power is transmitted via electromagnetic waves. Moreover, recently, integrating WPT with wireless communication has been flourishing [1–3]. However, a common challenge for such a strategy is the low efficiency [4], [5] because the receiver direction is unknown. Thus, measuring the DoA to adjust the receivers' direction is essential to increase efficiency of the system. One of the most efficient solutions for this issue is integrating the DoA system to maximize the transmitted energy to receivers while minimizing the transmitting power to interference sources. The other application of DoA estimation is passive remote sensing where the receiving signals have different amplitudes and phases due to the reflecting surface. In such cases, DoA estimation must be employed to detect the direction of receiving signals, from which the reflecting surface information is determined.

Based on the main parameters of a signal, the direction-finding method can be categorized into power-based, frequency-based, and phase-based. One of the most common power-based direction-finding methods is the Watson-Watt principle. This structure contains two crossed-loop antennas and a reference one. The incident angle is determined by the voltage ratio between the two receiving antennas. Although this method has a simple principle and the system is compact, it has a low resolution. The frequency-based method can be realized by using the Doppler principle that is the frequency of incident wave changes when the receiving point moves. Therefore, by determining the instantaneous frequency shift of a receiving antenna, the DoA can be calculated [6]. Although this method has better performance than the Watson-Watt method, it requires an extensive response time because of the huge number

of receiving antenna elements. Finally, the phase-based direction-finding can be realized by interferometry in which the DoA can be determined by measuring the power of output signals of an interferometer thanks to the direct relation between DoA and phase difference between antenna elements. In [7], the DoA error is around 1° within the range of 12° to 90°. Besides, the subspace DoA estimation such as multiple signal classification (MUSIC) and estimation of signal parameters via rotational invariance technique (ESPRIT). They are both well-known for high accuracy and high-resolution DoA estimation methods [8]. Another algorithm used in uniform circle array was proposed in [9] and another new one based on Pencil Method used for the uniform rectangular array was mentioned in [10]. However, they all require a certain complexity of a massive number of receiving antennas. The interferometry method requires the use of Michelson interferometers, which work well for optical spectrum, but become very bulky when scaling to the RF frequencies. Thus, they are not considered a suitable solution for low-power, easily integrated into other systems.

To satisfy the requirements of an easily integrated DoA system that has a small and simple structure and low-power consumption, in this project, we introduce a simple power-based DoA system consisting of a direction-finding unit and a data processing unit. The

first part contains two basic receiving antennas which receive the incident waves and a network of Wilkinson power combiners and dividers (WPDs), in which the waves received by the antennas interfere. The other part contains low-noise amplifiers, RF rectifiers, DC amplifiers, and a microcontroller unit. The angle of incident waves is determined based on the power of output signals of the DoA unit in the proposed DoA system. The system's error is less than 7.5^o in the measuring range of -60° to 60°.

II. PROPOSED DoA SYSTEM

This section presents explicitly the structure as well as the working principle of the proposed system. By analyzing the principle, this work provides the equation needed for calculating the DoA of the incident wave.

The system composes of a DoA sensor unit which has two receiving antennas and a network of power dividers and a power combiner, a data processing and measuring unit composes of three RF low noise amplifiers (LNA), three RF rectifiers, a DC amplifier circuit, a microcontroller, and finally a computer to process signals. The system operates at 2.6 GHz. The signal path is denoted by the black arrow in Fig. 1. The workflow of the system is as follows: Incident waves come to the DoA sensor unit. The signals received by the two antennas
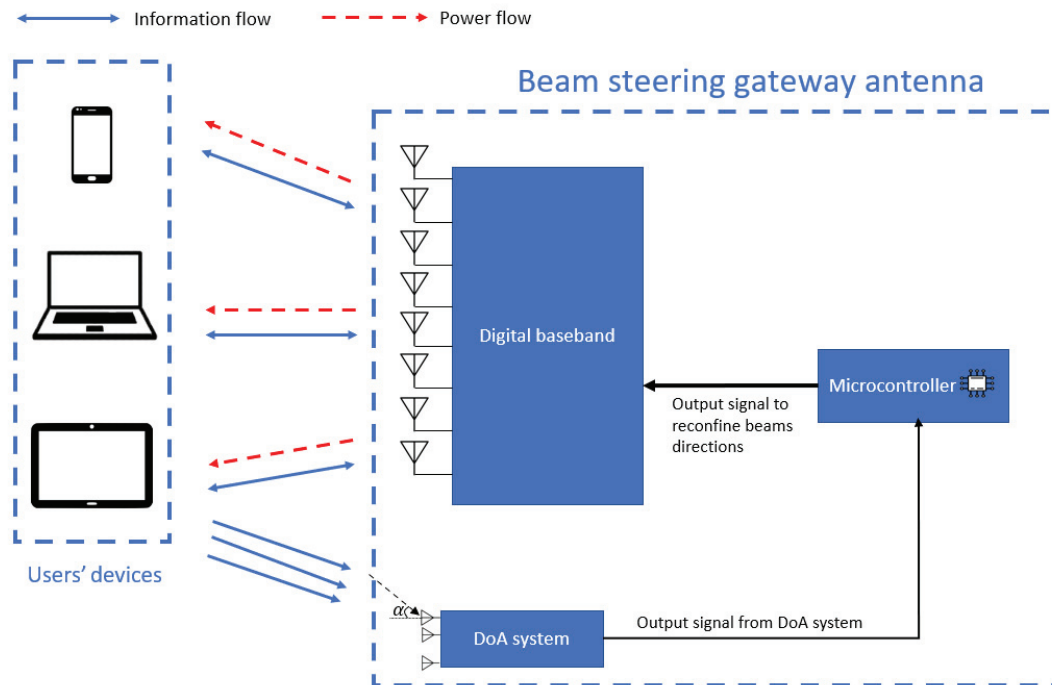

Fig. 1. Integrated DoA system in Simultaneous Wireless Information and Power Transfer (SWIPT) technology applied for beam steering gateway antenna.

interfere and go out at the three output ports. These three output waves go into the data processing and measuring unit. In this unit, the waves are rectified and amplified twice (once by the LNA and then by DC amplifier) so that the analog-to-digital converter (ADC) of the microcontroller (MCU) can detect the signals. The DoA can be evaluated and displayed on a computer's screen.

A. DoA sensor unit

The structure of the proposed DOA sensor unit is illustrated in Fig. 2. This unit consists of two directional receiving antennas separated from each other by a distance of d mm along with WPDs. When incident waves arrive with the incident angle α, the received power at ports 1, 2, and 3 are P_1, P_2, and P_3, respectively. Signal paths from antenna 1 and antenna 2 in the DOA sensor are denoted by the red and blue lines.

Received signals from two antennas go through two power divider circuits. Thus, half of the received powers by antenna 1 and antenna 2 go to port 1 and port 2, respectively. Whereas the other two halves continuously go through a power combiner. Here, the signals from antenna 1 and antenna 2 interfere with each other. As a result, the output signal at port 3 is the summation of the half-received power of port 1 and the one of port 2. By measuring magnitudes of output power at output ports, the DoA α will be calculated via a simple equation.

Let us label the received power on antenna 1 and antenna 2 as P and P', respectively. When this power goes through the power dividers, it is easily deduced that the magnitudes of the power at port 1 and port 2 are $P_1 = P/2$ and $P_3 = P'/2$, respectively. The output signal of port 3 is the sum of interference of the
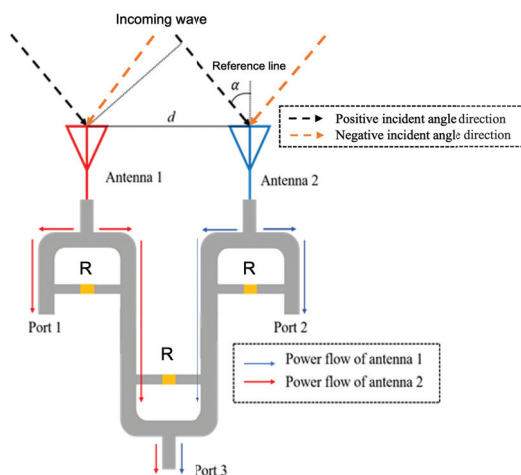
two components from power dividers which is $P_1/2$ and $P_2/2$, respectively. The phase difference between the two receiving signals is:

$$\Delta\phi = \frac{2\pi d \sin\alpha}{\lambda_0}, \tag{1}$$

where d is the distance between two receiving antennas and α is the angle of the incident wave and λ_0 is the wavelength of incident waves. The corresponding currents going from antenna 1, antenna 2, and at ports 3 are I_1, I_2, and I_3. The total current I_3 is the vector summation of I_1 and I_2. Therefore, I_3 is calculated by the Cosine rule as:

$$I_3^2 = I_1^2 + I_2^2 + 2I_1I_2\cos\Delta\phi. \tag{2}$$

To determine the power and currents on the power combiner, we analyze a Wilkinson circuit including quarter wavelength transformers with characteristic impedance $\sqrt{2}Z_0$ (Z_0 is the impedance of terms at ports) and an isolating resistor $2Z_0$ in even and odd modes with respect to the source at port 2. In the even mode, because of the symmetry, the symmetric plane of the circuit is open circuited, as illustrated in Fig. 3. Because both halves of the circuit are the same, for simplicity, we consider one of them. Ignoring open components, the circuit only includes the quarter wavelength transformer and the load $2Z_0$, which is shown in Fig. 3.

The input impedance seen from port 2 is:

$$Z_i = \sqrt{2}Z_0 \frac{2Z_0 + j\sqrt{2}Z_0\tan(\frac{2\pi}{\lambda}\frac{\lambda}{4})}{2Z_0 + j\sqrt{2}Z_0\tan(\frac{2\pi}{\lambda}\frac{\lambda}{4})} = Z_0. \tag{3}$$

Thus, in this mode, no current goes through the isolation resistor, the signal only goes on the quarter wavelength transformer and the load at port 1. On the other hand, in the odd mode, the symmetric plane of the circuit becomes short-circuited as shown in Fig. 3 and the upper half is illustrated in Fig. 3. The quarter wavelength transmission line with a short-circuited end is equivalent to an open circuit. So, the circuit only has the resistor Z_0. It means that in the odd mode signal, the current only goes through the isolation resistor. To sum up, the current going out at port 1 with the source at port 2 is the current in the even mode and the input impedance seen from port 2 is Z_0. Moreover, each output port of the power divider is connected to an LNA which has input impedance of 50Ω. Therefore, the output power at output ports can be represented based on three currents I_1, I_2, and I_3 as follows:

$$I_1^2 = P_1/2/50 = P_1/100, \tag{4}$$

$$I_2^2 = P_2/2/50 = P_2/100, \tag{5}$$

$$I_3^2 = P_3/50 = P_3/50. \tag{6}$$

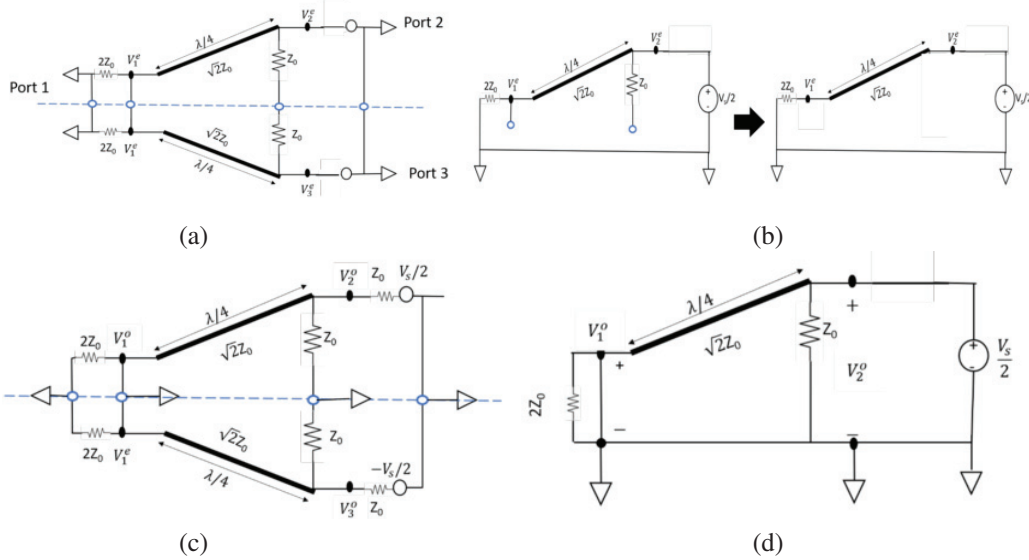Fig. 2. The structure of DoA sensor unit.

Fig. 3. The equivalent and upper half circuits of Wilkinson power divider in the even (a, b) and odd (c, d) modes.

Equation (2) becomes:

$$\frac{P_3}{50} = \frac{P_1}{100} + \frac{P_2}{100} + 2\sqrt{\frac{P_1}{100} \cdot \frac{P_2}{100}} \cos \Delta\phi. \qquad (7)$$

Replacing the equation (1) into equation (7), the angle α of the incident wave is calculated as follows:

$$\alpha = \arcsin\left(\arccos\left(\frac{\frac{P_3}{50} - \frac{P_1}{100} - \frac{P_2}{100}}{\sqrt{P_1 P_2}}\right)\frac{\lambda_0}{2\pi d}\right). \qquad (8)$$

B. Data processing and measuring unit

According to the working principle of the proposed device, we chose two dipole Yagi Uda antennas that have directional radiation patterns and compact size working at 2.6 GHz. The antennas dimensions were calculated and simulated. The radiation pattern of the manufactured antennas is shown in Fig. 4. The measured data indicates that the antennas are directive with a maximum gain of 6.52 dBi and high efficiency of 98.38%.

To calculate the DoA α, the values of power at three output ports of the DoA sensor have to be measured. The data processing and measuring unit measure all the mentioned signals and use an algorithm to calculate DoA α. In general, this unit contains four main parts: LNA, RF rectifiers, DC amplifiers, microcontroller, and MATLAB processing.

For LNA, we use the SBB5089 RF Power amplifier module which is designed for high linearity and minimal external components. By performing the measurement, all three LNA are shown to have a gain of 14 to 15 dB at 2.6 GHz with input power from -10 to 0 dBm.

Rectifier is one major part in the data processing block. Its main function is to convert AC voltages, which
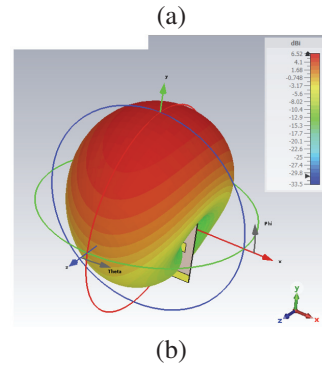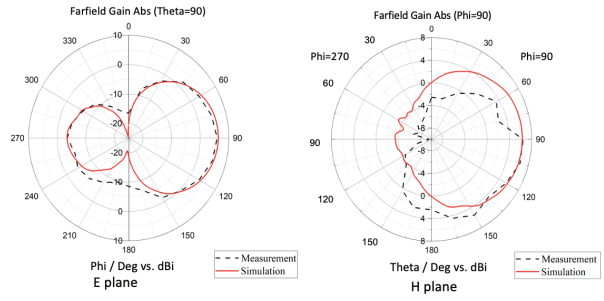

Fig. 4. The simulated and measured radiation pattern of Yagi Uda antenna (a) and 3D radiation pattern and (b) at 2.6 GHz.

are amplified by the LNA, into DC voltages, which will be the inputs of the DC power amplifier before going to the microcontroller. Therefore, the rectifier effectively determines the efficiency and accuracy of the received signals.

The rectifiers consists of multiple parallel connected half-wave voltage doublers. The SMS7630 Schottky
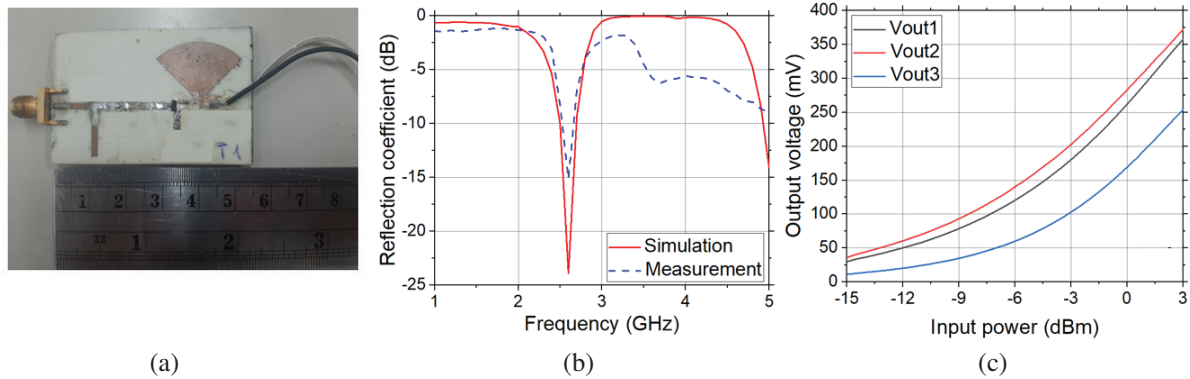
Fig. 5. (a) Manufactured rectifier, (b) Reflection coefficient, and (c) open-load output voltage of RF rectifier.

diode is chosen due to its high efficiency performance at low input power [11] with a 39 pF capacitor. Since the application of this work is for far-field SWIPT, the incident power is usually small. Therefore, in the DC filter part of the rectifier we use a radial stub instead of a lumped capacitor to minimize power loss due to welding. The commonly seen impedance matching stub is also employed to match the input impedance of the rectifier with output impedance of the LNA which is 50 Ω, as shown in Fig. 5 (a). The dimensions of microstrip lines are carefully calculated to tune the input impedance of the circuits to 50 Ω at 2.6 GHz. The design and simulation processes are conducted in ADS software in which the feed line is modeled as an AC source with 50 Ω impedance and the diode is modeled using the SPICE model. The parasitic inductance and capacitance of the diode is also considered. The requirement for the rectifiers is to create an output DC voltage as large as possible so they are designed with open ends. The simulation and measurement results are shown in Fig. 5. It is evident that the circuit resonates at 2.6 GHz. Output voltages of the three manufactured rectifiers range from 150 mV to 300 mV at 0 dBm input and go up as the input power increases. The plot of Fig. 5 (c) is stored as the data set of MATLAB program in 0.5 dBm resolution.

The output voltage of the RF rectifier is still low, and with a small input (below -10 dB) the output signal is noisy and brings errors. To solve this problem, a DC power amplifier is employed to amplify the output DC signal from the rectifiers and as well as to flatten this signal.

The measured DC voltages are processed in the following procedure: First, the STM32 microcontroller measures all three voltages. Then the processor uses the power voltage relation provided in Fig. 5 (c) to estimate the amount of power received by each antenna as well as the interference sum on Port 3. The Interpolation Technique is applied to calculate missing data in the input

data set of Fig. 5 (c). Subsequently, using equation (8) which is a simple trigonometric equation, the DoA α can be achieved and is printed on the screen.

III. EXPERIMENTAL VERIFICATION

The measurement system was put under-examinaion. The experiment configuration in real-life is displayed and all components are connected as described in Fig. 6. The incident wave, 0 dBm in strength, was generated by a Keysight E5080B ENA Vector Network Analyzer (VNA) and transmitted via a 6 dBi-gain reference Yagi antenna, placed 50 centimeters away from the system-under-test, comfortably inside the far-field of all antennas. All obstacles within a 50 centimeters radius were removed while all wireless sources in the proximity were turned off. In addition, we attached a needle indicator that is parallel to the reference line on the plinth of the rotating pillar. Hence, when we rotate the pillar with the attached DoA sensor, the needle indicator will clarify the true value of DoA. The processor and PC measured, calculated, and estimated the DoA every time the reset button of the processor was pressed. The DoA value was automatically calculated and displayed on the PC screen. In the experiment setup, the excited wave traveled to the receiving antennas at 0° elevation angle. Since the designed distance between two receiving antennas is 70 mm, the measurable DoA range should be from -60° to 60°. In the experiment, the azimuth angle was varied in this range with a 10° step. The measured DoA result as displayed in Fig. 7 yields high accuracy, and only differs as much as 7.5^o from the ground truth. The major reason for the error is that when we rotate the receiving antennas in the experiment, which will create a larger DoA value, the energy density around the two antennas will not be the same. The main idea of this paper is to determine DoA based on power received by each antenna, so the balance of energy density of both antennas is really important. Therefore, the difference in this value as mentioned will
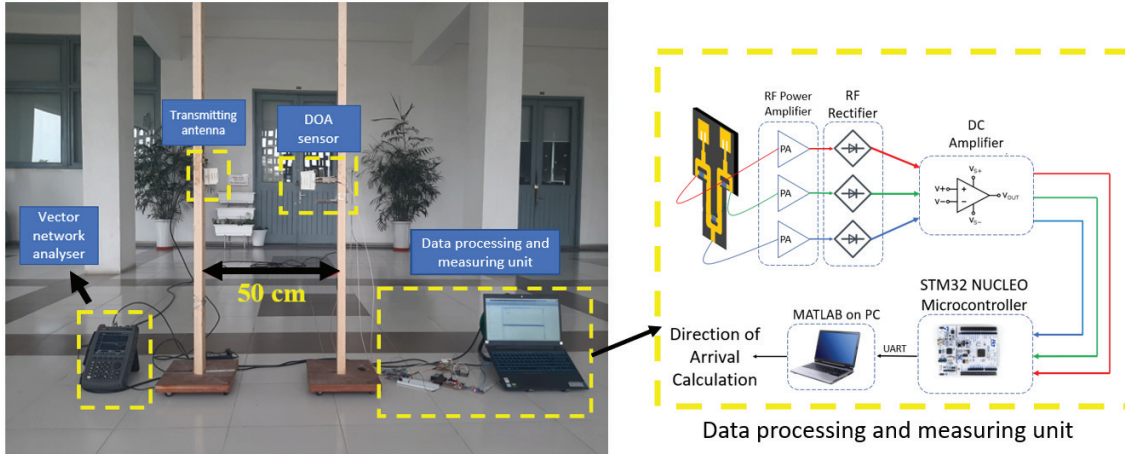
Fig. 6. Experiment configuration to examine the accuracy of the proposed DoA system.

Table 1: Comparison DoA measuring performance between the proposed and other systems

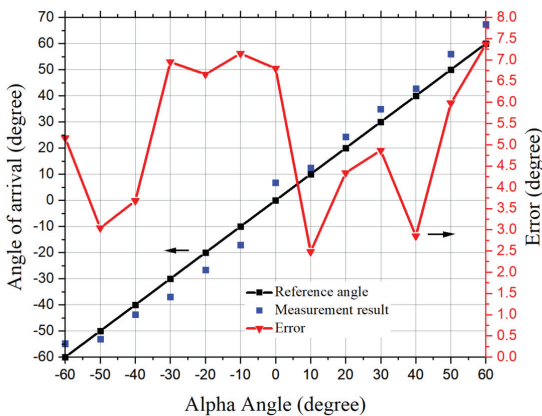| References	Working Frequency	Measuring Range	Error	Method
[7]	2.65 GHz	12.6^o to 90°	Less than 2°	Photonic-based
[12]	2.45 GHz	-30° to 30°	-2.1^o to 3.5^o	Based on harmonic reradiation
[13]	10 GHz	1.82^o to 90°	Less than 1°	Photonic-based
This work	2.6 GHz	-60° to 60°	Less than 7.5^o	Power-based

Fig. 7. The measurement result.

affect the measured result. The other reason would be due to the mismatch between each device in the data processing and measuring unit. To have the best output result, the devices in each output power port need to be identical. However, due to the lack of accuracy in the manufacturing process, there were some mismatch happened. These imprecisions, overall, have contributed to the error in the final result.

Table 1 shows the comparison of this work and several previous works. It can be seen that the proposed DoA system possesses a simpler structure as it is only compose of two receiving antennas and simple passive circuits that are the WPDs, while the system in [7] and [13] consists of Mach Zehnder modulation utilizing the laser source. The DoA estimation system in [12] is just two receiving microstrip antennas, which is too simple, leading to a narrow measuring angle compared to other works. The power-based DoA also was proposed in some previous works such as [14] and [15]. However, they mainly focused on a part of the DoA system which is antenna configuration. The simple, complete DoA system like this work, to the best of our knowledge, has not yet been studied. With a wide measuring angle range and highly simple structure, the proposed DoA system has big potential to be widely applied in practical structures such as WIPT.

IV. CONCLUSION

In conclusion, we have proposed and empirically investigated an alternative approach to measure the DoA of microwave signals based on interference. The proposed system consists of a DoA sensor and a data processing unit and yields less than a 7.5^o error in the tested range of -60° to 60°. The advantages of this method are its simple structure, compactness, low cost, and ease of manufacture as well as being a potential candidate for the DoA finding devices integrated in the gateway system using SWIPT technology.

REFERENCES

[1] S. Zouaoui, M. Souilem, W. Dghais, A. Radwan, S. Barmada, and M. Tucci, "Wireless power transfer and data communication cognitive radio through two-coil inductive channel," *IEEE Global Communications Conference (GLOBECOM)*, Waikoloa, HI, USA, Feb. 2019.

[2] B. Clerckx, R. Zhang, R. Schober, D. Ng, D. Kim, and H. Poor, "Fundamentals of wireless information and power transfer: From RF energy harvester models to signal and system designs," *IEEE Journal on Selected Areas in Communications*, vol. 37, pp. 4-33, Jan. 2019.

[3] B. Clerckx, K. Huang, L. Varshney, S. Ulukus, and M.-S. Alouini, "Wireless power transfer for future networks: Signal processing, machine learning, computing, and sensing," *IEEE Journal of Selected Topics in Signal Processing*, Aug. 2021.

[4] T. D. P. Perera, D. N. K. Jayakody, S. Chatzinotas, and V. Sharma, "Wireless information and power transfer: Issues, advances, and challenges," *IEEE 86th Vehicular Technology Conference (VTC-Fall)*, pp. 1-7, 2017.

[5] D. W. K. Ng, T. Q. Duong, C. Zhong, and R. Schober, *The Era of Wireless Information and Power Transfer*, Wiley Telecom, 2019.

[6] D. Peavey and T. Ogumfunmi, "The single channel interferometer using a pseudo-Doppler direction finding system," *IEEE International Conference on Acoustics, Speech, and Signal Processing*, Apr. 1997.

[7] H. Chen and E. H. W. Chan, "Simple approach to measure angle of arrival of a microwave signal," *IEEE Photonics Technology Letters*, vol. 31, pp. 1795-1798, Oct. 2019.

[8] O. A. Oumar, M. F. Siyau, and T. P. Sattar, "Comparison between MUSIC and ESPRIT direction of arrival estimation algorithms for wireless communication systems," *International Conference on Future Generation Communication Technology*, pp. 99-103, 2012.

[9] Y. Tian, Y. Huang, X. Zhang, M. Lin, and X. Qiao, "A robust algorithm for DOA estimation of coherent sources with UCA," *Applied Computational Electromagnetics Society (ACES) Journal*, vol. 37, no. 6, pp. 692-701, 2022.

[10] A. Azarbar, G. R. Dadashzadeh, and H. R. Bakhshi, "2-D DOA estimation with matrix pencil method in the presence of mutual coupling," *Applied Computational Electromagnetics Society (ACES) Journal*, vol. 27, no. 9, pp. 742-748, 2012.

[11] S. Hemour, Y. Zhao, C. H. P. Lorenz, D. Houssameddine, Y. Gui, C.-M. Hu, and K. Wu, "Towards low-power high-efficiency RF and microwave energy harvesting," *IEEE Transactions on Microwave Theory and Techniques*, vol. 62, no. 4, pp. 965-976, 2014.

[12] S. K. Tomohiko Mitani and N. Shinohara, "Direction-of-Arrival estimation by utilizing harmonic reradiation from rectenna," *IEEE Wireless Power Transfer Conference (WPTC)*, Feb. 2018.

[13] L. Peng, Y. Lianshan, Y. Jia, F. Xia, P. Wei, L. Bin, Z. Xihua, Z. Tao, and C. Zhiyu, "Photonic approach for simultaneous measurements of Doppler-frequency-shift and angle-of-arrival of microwave signals," *Optics Express*, vol. 27, pp. 8709-8716, Feb. 2019.

[14] Y. Han, Q. Fang, L. Song, F. Yan, X. Qiao, and S. Zhuang, "DOA estimation for unequal power sources using extremely low profile aperture coupled microstrip antenna," *Applied Computational Electromagnetics Society (ACES) Journal*, vol. 31, no. 9, pp. 1100-1109, 2016.

[15] R. Pohlmann, S. Zhang, T. Jost, and A. Dammann, "Power-based direction-of-arrival estimation using a single multi-mode antenna," *14th Workshop on Positioning, Navigation and Communications (WPNC)*, Jan. 2018.

Nga Vu received her B.Sc. degree in Control and Automation Engineering from the School of Electrical and Electronic Engineering of Hanoi University of Science and Technology in 2021. She is currently doing a Master's at École normale supérieure Paris-Saclay - Université Paris-Saclay, France. Her research interest is applied electromagnetics.

Thinh Le received his B.Sc. degree in Control and Automation Engineering from the School of Electrical and Electronics Engineering of Hanoi University of Science and Technology in 2022. He is currently doing a Master's at University of North Texas, USA. His research interests is applied electromagnetics.

Minh Dinh received his B.Sc. degree from Hanoi University of Science and Technology in 2021. He is currently pursuing his doctorate in Electrical Engineering at the University of Southern California, USA. His research interest is photonics.

Minh Thuy Le received her B.Sc. and M.S. degrees in Electrical Engineering from Hanoi University of Science and Technology in 2006 and 2008, respectively, and Ph.D.degree in Optics and Radio Frequency from Grenoble Institute of Technology, France in 2013. She is currently an Assoc. Prof. and a group leader of the Radio Frequency group at the Smart Sensor Laboratory, School of Electrical and Electronic Engineering (SEEE), Hanoi University of Science and Technology (HUST). Her research interests include build-in antenna, antenna array, beamforming, metamaterials, energy harvesting and wireless power transfer.

A Wideband, High Gain and Low Sidelobe Array Antenna for Modern ETC Systems

Lan T. Tran, Chinh D. Khuat, and Lam V. Phi

Department of Electrical and Electronic Engineering
University of Transport and Communications, Hanoi, 100000, Vietnam
ttlan@utc.edu.vn, linhchinh07@gmail.com, pvlam@utc.edu.vn

Abstract – Modern electronic toll collection (ETC) systems are currently moving towards a system design that is capable of fast and optimal payment handling for a single lane. Thus, the antenna of a roadside reader unit (RSU) needs to provide sufficient coverage over the vehicle lane during a payment cycle. In this paper, a left-hand circularly polarized (LHCP) 2×4 array antenna is proposed for European standard RSU readers at 5.8 GHz. The proposed array antenna consists of patch element antennas with parasitic elements to enhance gain and bandwidth. Sequential phase rotation feeding networks are applied to make the antenna low-profile. By using the optimized nut-shaped metasurface, the antenna can achieve higher gain due to concentrated radiation power in the boresight direction. The antenna has a wide impedance bandwidth of 2.34 GHz (37.73%), axis ratio bandwidth of 2.07 GHz (32.9%), high gain of 17 dBi, and sidelobe level (SLL) lower than -15 dB at 5.8 GHz. Especially, half-power beamwidths are $34°$ and $17°$ in horizontal and vertical planes, respectively, which covers sufficient space for a single lane while avoiding interference with other lanes. The performance of the proposed antenna is verified by measured results. It showed that the proposed antenna is a promising candidate for ETC applications.

Index Terms – circularly polarized antenna, FFETC, high gain, metasurface, RSU antenna, wideband antenna.

I. INTRODUCTION

The free-flow electronic toll collection (FFETC) is an important part of the intelligent transportation system (ITS), which allows vehicles on the highway to not to have to stop when passing through a toll station. This helps to improve traffic efficiency and reduce congestion, accidents, and environmental pollution. The structure of the FFETC system consists of a roadside unit reader (RSU) at the gate and an onboard unit (OBU) on the vehicle's window. They communicate with each other through the dedicated short-range communication (DSRC) standard. DSRC is a new technology that allows high-speed data transmission, while the accuracy and security are also superior to previous technologies like RFID [1]. Therefore, this technology has been deployed in many major countries around the world such as the United States, Japan, and European countries.

In Europe, two DSRC standards, EN12253 and EN302571, were established for CEN DSRC and ITS DSRC by the European Committee for Standardization (CEN) and the European Telecommunications Standards Institute (ETSI) [2, 3]. In particular, CEN DSRC is used for transportation applications with high reliability and performance in high-speed non-stop single-flow or multi-flow environments. For an RSU, EN12253 specifies the antenna operating at 5.8 GHz with a minimum bandwidth of 20 MHz. The beamwidth is limited to a vertical angle of $70°$, and a power of 33 dBm. Outside this coverage, the radiated power must be less than 18 dBm. In other words, the sidelobe level (SLL) of the antenna should be less than -15 dB. The polarization of the antenna is left-hand circularly polarized (LHCP) with a high polarization isolation of 15 dB in the main direction and 10 dB within the half-power beamwidth.

Studies have shown that an antenna with a main beam in H plane θ_h that is too wide should not be used because it can cause interference with neighboring lanes. The recommended half-power beamwidth is about $20°$ and the SLL is less than -15 dB [4]. On the other hand, for the payment to be guaranteed on the condition that the vehicle does not need to decelerate, the payment cycle between OBU and RSU must be very short, no more than 200 ms [5]. One solution is to reduce the central processing unit (CPU) cycles in the RSU (i.e. increase clock frequency). However, this solution is not feasible because the highest clock frequency currently does not exceed 100 MHz, and increases the cost of the RSU. Another possible solution is to design an antenna for the RSU with a transmission range to cover the vehicle's mileage in a billing cycle. Through this solution, RSU costs can be significantly reduced.

An FFETC system is set up as shown in Fig. 1. The RSU is mounted on the gate at the height of h_{RSU}, and made with the vertical axis at an angle β, θ_v is the half-power beamwidth (HPBW) of the antenna in the vertical plane. An OBU is installed on a vehicle whose distance to the road surface is h_{OBU}. To ensure a payment cycle takes place, the distance MN must be long enough (or θ_v must be wide enough) when the vehicle is traveling in one payment cycle at the allowed speed of v. There are two main loss factors influencing communication between RSU and OBU: the first one is free space loss L_{space} and the second is loss from car windows L_{win}. L_{space} depends on the instantaneous distance between OBU and RSU r, while L_{win} depends on the material of car windows. For accurate communications, the received OBU power P_r must be greater than -43 dBm [5]. Based on the Friis transmission equation, P_r is represented by equation (1). Parameters P_t, L_{space}, L_{win} and G_r are factors outside RSU. So the only solution to make sure the received signal is large enough is to increase G_t. Thus, our design criteria that need to be achieved for the RSU antenna are high gain, vertical HPBW θ_v wide enough, horizontal HPBW $\theta_h \leq 20°$ and SLL $\leq$ -15 dB. According to European standards, $h_{RSU} \leq 5.5$ m [5] and assuming h_{OBU} = 1.5 m. Therefore, the relationship between vehicle speed v and θ_v is given in Table 1.

$$P_r(t) = P_t + G_t(\theta) - L_{space}(r) - L_{win} + G_r. \quad (1)$$

The paper [5] also proposed an antenna with a radiation pattern with a vertical beam of 30° and a horizontal beam of 15°. However, the antenna SLL is high, about -12.5 dB. Recently, there has been some research on antenna design for RSU. In [6], a 10×10 antenna array is proposed with a high gain of up to 14.3 dBi. The antenna used a Woodward and Lawson feeding structure to achieve a low SLL of -28.2 dB. But, it has a symmetrical radiation pattern of about 37° in both vertical and horizontal planes, a fairly wide beam, and can cause interference to adjacent lanes. In addition, in the operating frequency range, the axis ratio value of 2.7 dB represents a low circular polarization purity. The 12-element antenna array in [4] is more optimally designed for the EN12253 standard. It has a wide bandwidth of 1.13 GHz with 15 dB high polarization isolation, HPBW of 23°, gain of 14.7 dBi at 5.8 GHz, and peak gain of 17 dBi at 5.9 GHz. In particular, its SLL is low, about -17 dB, thanks to the use of a Chebyshev feeding network. But, its beamwidths have not been optimized based on the vehicle's speed to cover a distance for a payment circle. Similarly, this is a weak point of the antennas in [7–11].

In [12], a 2×4 antenna array was introduced with high gain, vertical (V), and horizontal (H) beamwidths of 33.2° and 17.1°, respectively. However, the SLL is quite high, around -13 dB, and its performance has not
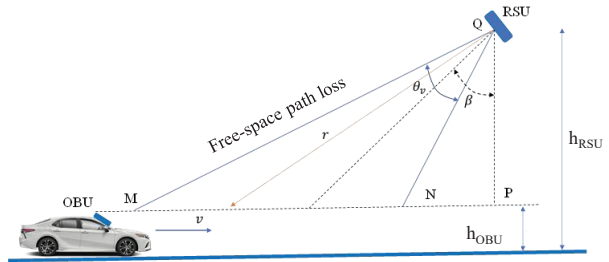

Fig. 1. The communication between OBU and RSU.

Table 1: The relationship between the beamwidth θ_v and the velocity of vehicle v

v (km/h)	60	100	130
θ_v (degree)	22	34.6	39

been verified by measurement. Therefore, this study will continue to improve it to meet the requirements for an RSU antenna as mentioned above. The double circle unit cell is analyzed and optimized to get characteristics of the metasurface with both negative permittivity (ε<0) and negative permeability (μ<0) to enhance the performance of the proposed antenna by reducing SLL and improving AR bandwidth. Compact size is another advantage of the proposed antenna by utilizing a sequential phase rotation feeding network. FR-4 is used for fabrication to obtain a low-cost antenna. Finally, the performance of the proposed antenna is verified by measured results.

The paper is organized into three parts. Part II presents the antenna design process, which will analyze the antenna components including the unit cell, element antenna, 2×2 array antenna, and 2×4 array antenna with the reflector. Some conclusions and discussions are given in Part III.

II. ANTENNA DESIGN

A. Unit cell

LHCP patch antennas are widely used for ETC applications. However, they are generally low gain, so improving gains for these antennas is a challenge for researchers. Several solutions have been proposed, for example, using parasitic sheets [13, 14], deploying stacked patches [15, 16] and implementing metamaterials [17, 18, 27–31]. The use of the parasitic patch in [13] can improve gain very well, and it can also extend the circular polarization bandwidth for antennas deployed on the same plane. However, the disadvantage of this structure is that the antenna size may be larger. In [15], deploying two patch layers was proposed. Simulation and measured results show that the gain of the antenna is significantly improved from 5

dBi to 10.5 dBi. This method does not increase the size of the antenna, but it does make the antenna thicker and more difficult to fabricate due to misalignment between layers. The gain of the antenna in [17] was enhanced by 2 dBi thanks to applying a metasurface placed on the main radiation patch. The antennas in [17–22] also implemented a metasurface, but the special feature of these designs is that the metasurface is capable of re-polarization from LP (linear polarization) to CP. Thereby, we can see that using a metasurface is not only to reconfigure the polarization but also to increase gain.

In this study a new unit cell and a metasurface are proposed to improve gain, and AR bandwidth, and to create a low-profile antenna. The structure of the proposed unit cell is shown in Fig. 2 (a). It is nut-shaped, made up of two circles of radius $r = 2.1$ mm with a total length of $k = 6$ mm. Each unit cell is printed on an FR-4 substrate with the permittivity $\varepsilon = 4.3$ and thickness of 1.6 mm. Compared to the unit cell in [12, 25], four corners of the unit cell are cut apart as shown in dashed boxes. The unit cell is rotated 45° compared with the Y-axis direction. The proposed unit cell is simulated by CST Studio Software [26] with the boundary condition as shown in Fig. 2 (b), where Port 1 is located 4 mm far from the surface of the unit cell, and Port 2 is located at a long distance away because this side of the metasurface is open so it is chosen as one wavelength.

The proposed unit cell is truncated and has a smaller size compared to the non-truncated unit cell (N-T unit cell) in [25], as a result, the mutual coupling between element antennas in the proposed array is reduced. Then, the SLL of the proposed array antenna is enhanced. The performance of the proposed unit cell and metasurface

when they are integrated into the element antenna will be presented in the next subsections.

B. Element antenna

The element antenna is designed with the metasurface structure proposed in subsection A. The structure of the element antenna is shown in Fig. 3. It has two layers: the lower layer is a reference antenna that was introduced in [12, 25], and the upper layer is the proposed metasurface, which is a 4×4 unit cell array. The distance between unit cells is d. The distance between the two layers is h. The size of the ground plane is $W\times W$.
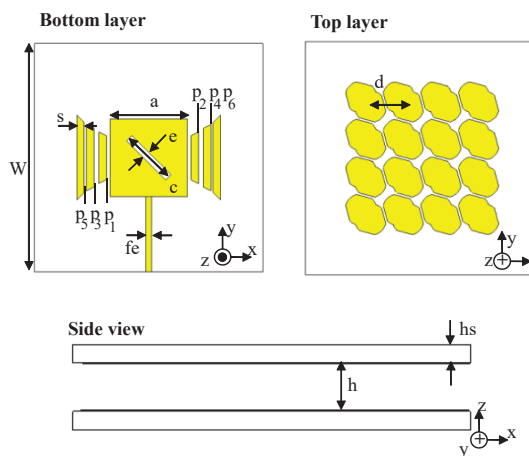

Fig. 3. Structure of element antenna using the proposed metasurface ($a = 10.5$, $c = 7.5$, $d = 5$, $e = 1$, $fe = 0.7$, $g_1 = 0.5$, $g_2 = 0.7$, $g_3 = 0.3$, $h = 4$, $hs = 1.6$, $p_1 = 5$, $p_2 = 7$, $p_3 = 8$, $p_4 = 9$, $p_5 = 9.5$, $p_6 = 11.5$, $s = 1$, $W = 33$) Unit: mm.

To analyze the role of antenna components, three antenna versions (AN1, AN2, and PROP) in Fig. 4 are simulated and compared with each other. AN1 is a square patch antenna with a diagonal slot in the middle. AN2 consists of AN1 and six parasitic patches, and the final model PROP contains AN2 and the proposed metasurface. PROP is the proposed element antenna. The simulation results of these three antennas are shown in Fig. 5.

Figure 5 reveals that AN1 resonates at 5.7 GHz and 6.2 GHz with S_{11} values of -7 dB and -8 dB. The lowest axis ratio value is 15 dB at 5.8 GHz while the peak gain is 5.7 dBi at 6.2 GHz. After adding the six isosceles trapezoidal parasitic patches, the AN2 resonates better at 6.2 GHz, while an additional resonance appears at the higher frequency of 7.25 GHz. The AR curve appears with three sharp peaks where there are small AR values of 12 dB, 16.5 dB, and 10.5 dB at 5.8 GHz, 7.2 GHz, and 7.4 GHz. The gain value at the low-frequency band seems to be constant, however, due to

Fig. 2. (a) Geometry of unit cell and (b) numerical unit cell model for simulation.
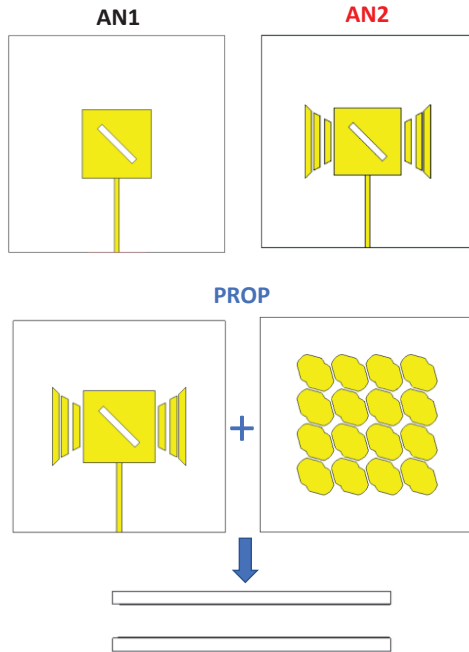
AN1   **AN2**

PROP

+

Fig. 4. Three different versions of the element antenna.

the resonance at 7.2 GHz, the gain at this frequency reaches 6 dBi. It can be seen that AN1 and AN2 have weak resonance, low gain, and no circularly polarized radiation. After adding the proposed metasurface, the impedance matching is greatly improved, and PROP achieves an impedance bandwidth (Imp. BW) of 1.2 GHz (20.34%). At the same time, the elliptical polarization of AN2 is also converted to circular polarization when using the proposed metasurface with an axial ratio bandwidth (AR BW) of 1 GHz (16.39%). In particular, the gain of PROP is significantly improved in the entire working frequency range with a very stable high value in the range of 7÷8 dBi (the gain curve is flat as shown in Fig. 5 (c)). Thus, using the proposed metasurface significantly improves the performance of circularly polarized antennas.

As mentioned in subsection A, the T unit cell reduces mutual coupling between element antennas. This is proved in Fig. 6, which shows the electric field (E-field) of the element antenna in two cases with the T unit cell and the N-T unit cell. It can be seen that the E-field in the case of the T unit cell is more concentrated in the boresight direction than that in the case of the N-T unit cell. Similarly, S_{21} of two-element antennas is also simulated in these two cases as shown in Fig. 7. At 5.8 GHz, S_{21} is reduced to 3.6 dB. Thus, the SLL of the proposed array is improved by using this T unit cell.

(a)

(b)

(c)
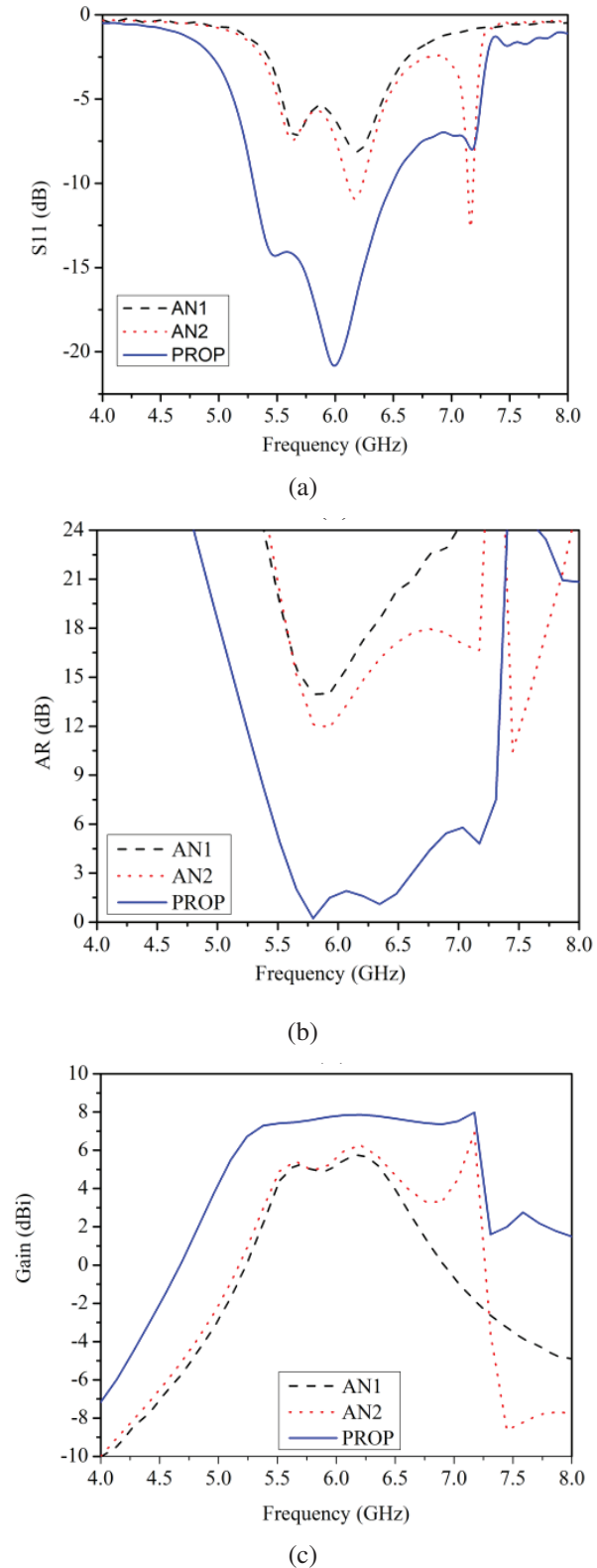
Fig. 5. Simulated results of three antenna versions in (a) S_{11}, (b) AR, and (c) gain.
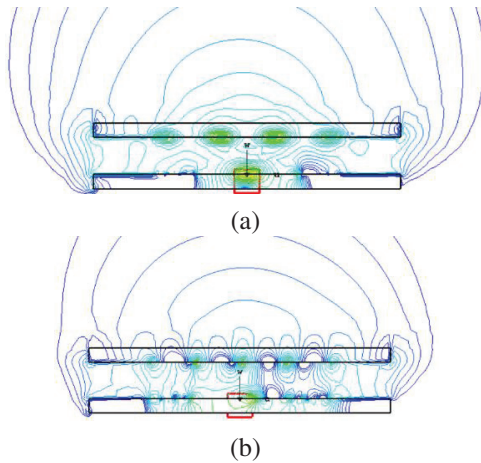
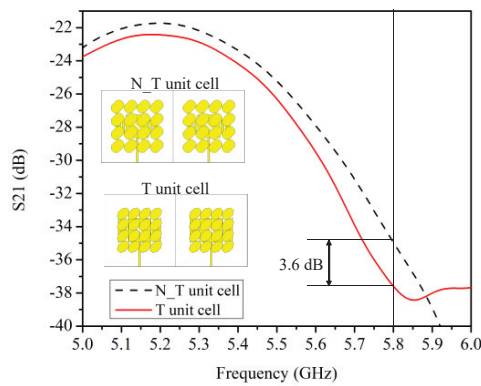Fig. 6. E-field of the element antenna (a) with the N-T unit cell and (b) with the T unit cell.

Fig. 7. Simulated S_{21} between two element antennas with the N-T unit cell and the T unit cell.

C. The proposed 2×2 array antenna

The 2×2 antenna array is designed as shown in Fig. 8. The four-element antennas are fed by the sequential phase rotation feeding network which was introduced in [25]. This feeding network contributes to
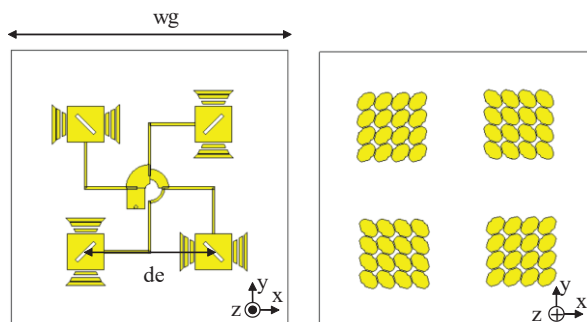

Fig. 8. The proposed 2×2 antenna array.

enhancing the AR bandwidth and making the proposed antenna compact. The distance between the element antennas is de = 37 mm and the total length is wg = 80 mm. Some fabrication photos of this antenna are shown in Fig. 9. Simulation and measured results in S_{11}, gain, and AR are given in Fig. 10. The measured result in S_{11} has a good agreement with the simulation ones. Figure 10 (b) provides information about the gain, where the maximum gain is 14.3 dBi at 5.8 GHz. The simulated AR bandwidth is 2 GHz (32.5%). The SLL of the 2×2 array antenna in the case of the T unit cell is lower than that in the case of the N-T unit cell as shown in Fig. 11. The measured radiation patterns agree well with the simulation ones. The HPBW are approximately 34° and the maximum SLL is -15.3 dB. Thus, the performance of the 2×2 array antenna is verified by the measured results with a high gain and wide bandwidth. But, its HPBWs are symmetrical, which has not satisfied for requirements of ETC antennas in terms of beamwidths as mentioned above. As a result, the 2×2 array antenna continues to be developed into a 2×4 array antenna presented in subsection D.
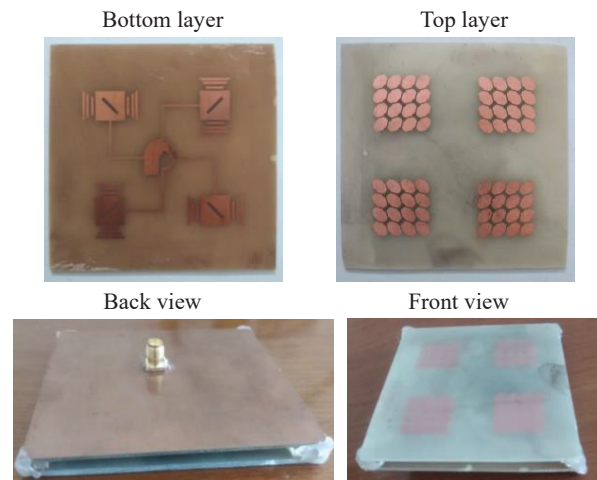

Fig. 9. Photos of the fabricated 2×2 antenna arrays.

D. The proposed 2×4 array antenna

The 2×4 antenna array is proposed in Fig. 12. It consists of three layers: the top layer is metasurface, the middle layer is the 2×4 patch antenna array, and the bottom layer is a T-shaped feeding network. The overall size of the proposed antenna is $W_t \times L_t$. The distance between two 2×2 arrays is d_f and the distance between the bottom layer and the middle layer is ha. The T-shaped feeding network has an input of the 50 Ω line. A $\lambda/4$ segment with a characteristic impedance of 35 Ω is used to match impedances for two 50 Ω outputs, which are
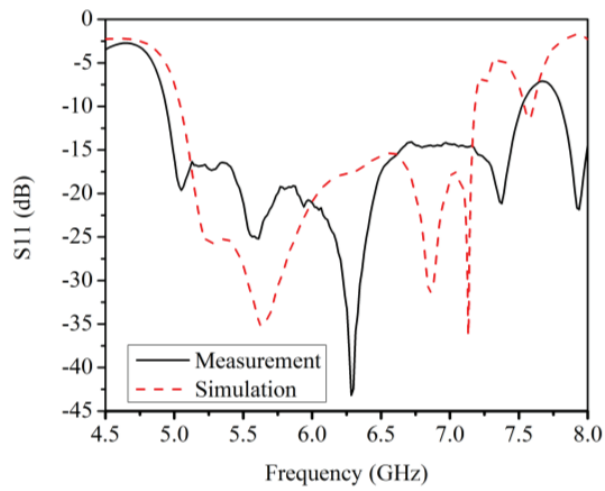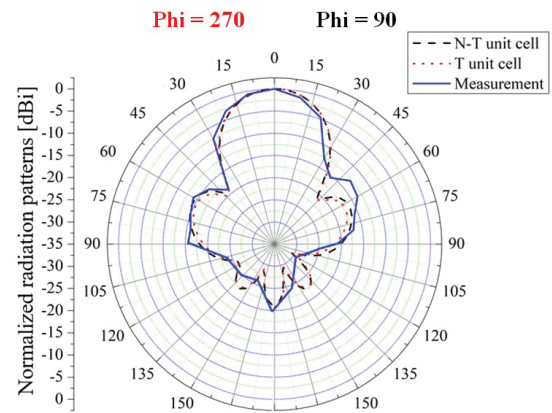
(a)
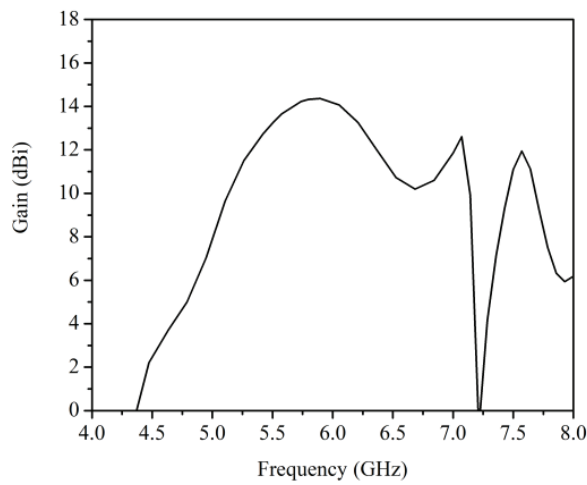
(b)
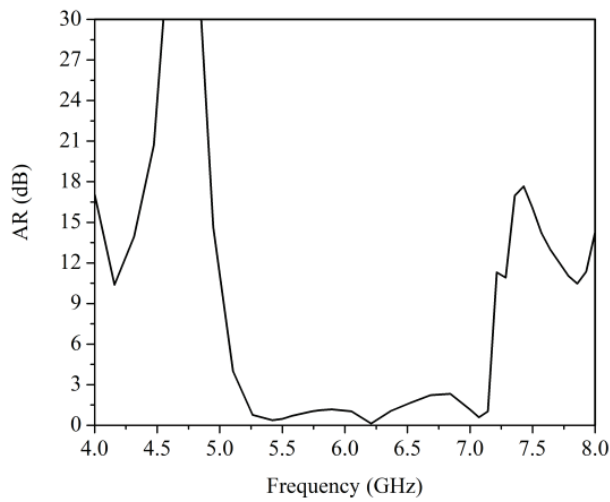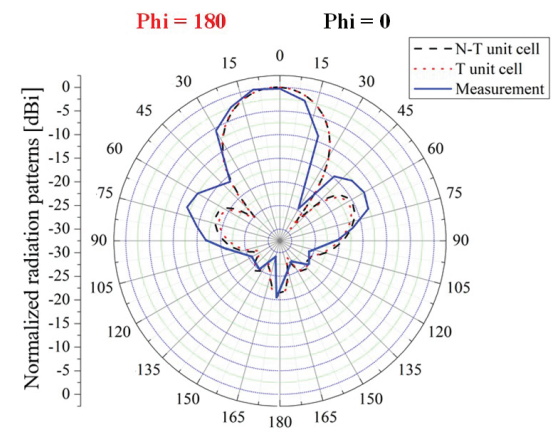

(c)

Fig. 10. Simulation and measured results of the 2×2 antenna arrays: (a) S_{11}, (b) gain, and (c) AR.

(a) YOZ plane

(b) XOZ plane

Fig. 11. Simulation and measured radiation patterns of the 2×2 array antenna in two cases: N-T unit cell and T unit cell in two planes (a) YOZ plane, (b) XOZ plane.
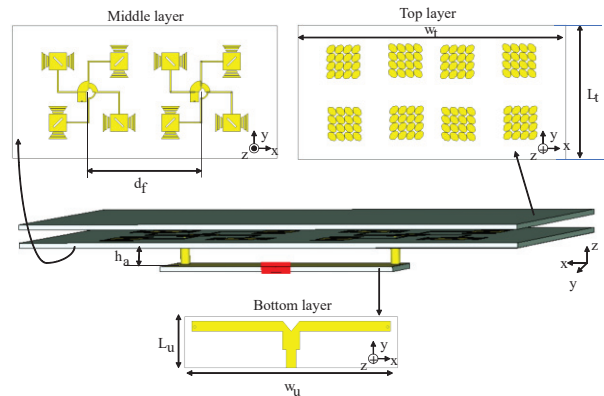

Fig. 12. The proposed 2×4 antenna array ($W_t = 160$, $L_t = 80$, $h_a = 7$, $L_u = 17.5$, $W_u = 75$, $d_f = 53$. Unit: mm).

connected to two 2×2 array antennas by coaxial cables. The size of the feeding network is $W_u×L_u$. Fabrication photos of the 2×4 array antenna are shown in Fig. 13.

The simulation and measured results of the 2×4 array are shown in Figs. 14 and 15, which show the impedance bandwidth of 2.34 GHz (37.56%), and the 3-dB AR bandwidth of 1.865 GHz. (30.6%), and the peak gain of 16.6 dBi at 5.8 GHz. The vertical beamwidth ($φ = 0°$) and the horizontal beamwidth ($φ = 90°$) are 35° and 18.6°, respectively. The proposed 2×4 array antenna meets almost all requirements for an ETC antenna, but the SLL of this antenna is -13.3 dB, so is quite high. Therefore, a reflector is added to compress the SLL.
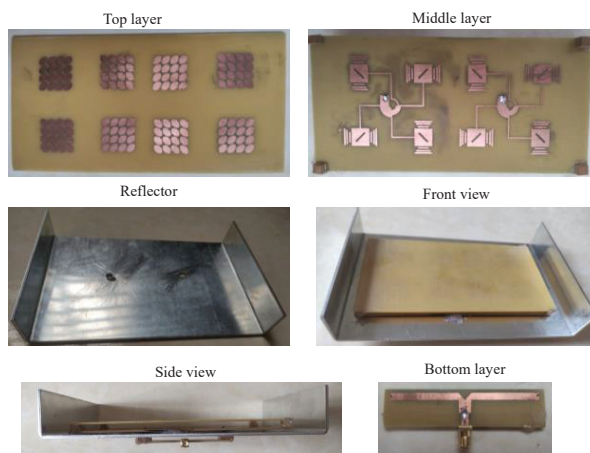

Fig. 13. Fabrication photos of the proposed 2×4 array antenna.

Figure 16 shows the 2×4 array antenna with the reflector. The size of the reflector is $w_r×L_r×h_r$. Two metal plates are placed on either side of the antenna, where the SLLs need to be reduced. The height of these two plates h_r is the main parameter affecting the SLL reduction. The larger h_r is, the smaller the sidelobe is. In addition, the wider reflector also helps to reduce the sidelobe.

In the plane $φ = 0°$, the SLL is significantly reduced from -13.3 dB to -15.7 dB while the SLL is -17.2 dB in the plane $φ = 90°$ as given in Fig. 15. The vertical beamwidth ($φ = 0°$) and the horizontal beamwidth ($φ = 90°$) are 34° and 17°, respectively. The measured radiation patterns are also shown in Fig. 15. There is little difference between the simulation and measured results, which is caused by measurement and fabrication errors.
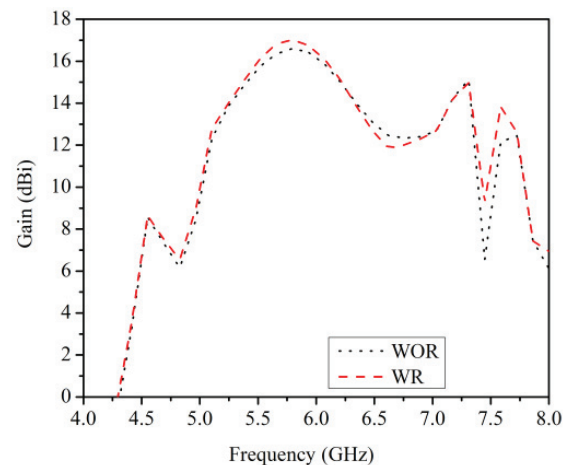
The effect of this reflector is more clearly shown by simulation results in Fig. 14. Figure 14 (a) shows that the impedance bandwidth is almost unchanged while 3-dB AR bandwidth is extended to 2 GHz (32.9%) in Fig. 14 (b), and the gain is improved to 17 dBi at 5.8 GHz. In
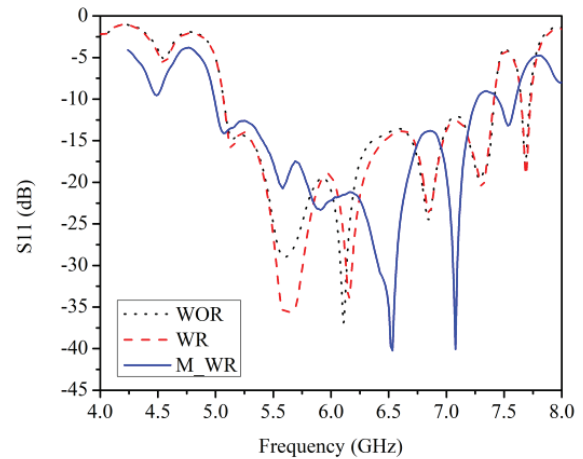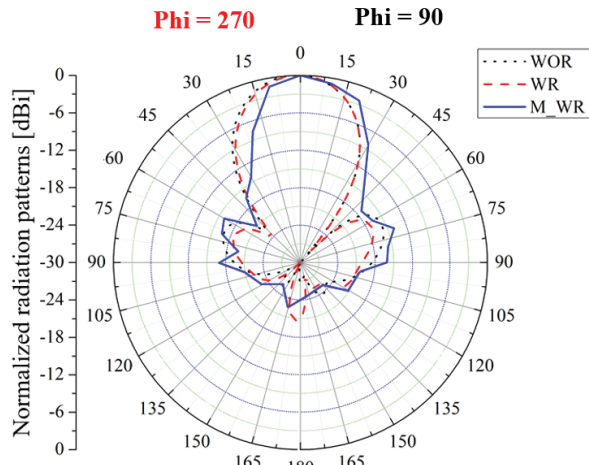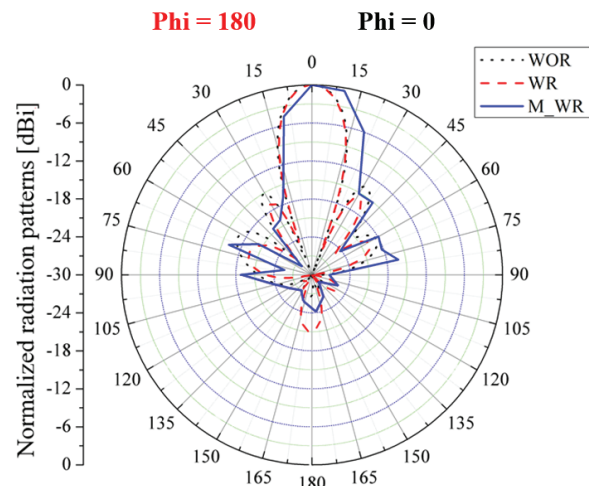

(a)
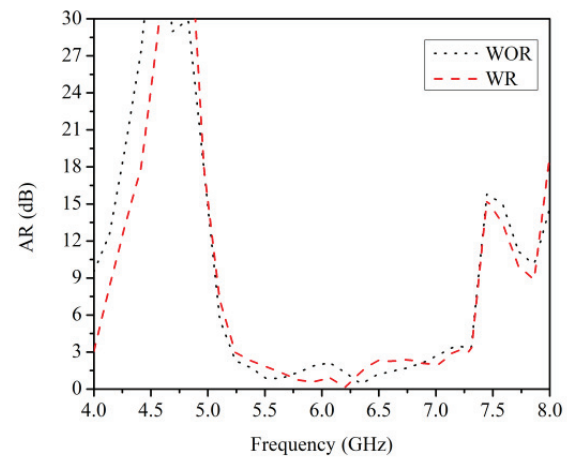
(b)

(c)

Fig. 14. Simulation and measured results of three cases without reflector (WOR), with reflector (WR), and measurement with reflector (M_WR) in (a) S11, (b) AR, and (c) gain.

(a) YOZ plane

(b) XOZ plane

Fig. 15. Simulation and measured radiation patterns of the 4 × 4 array antenna in three cases: without reflector (WOR), with reflector (WR), and measurement with reflector (M_WR), in two planes (a) YOZ plane, (b) XOZ plane.
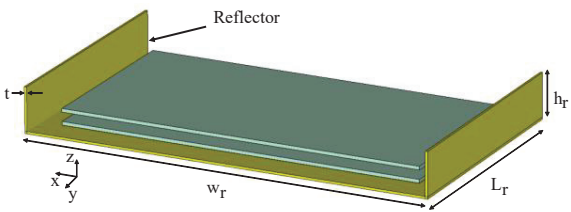

Fig. 16. The 2×4 array antenna with the reflector.

summary, the additional reflector can reduce the SLL, and increase both the AR bandwidth and the gain of the proposed 2×4 array antenna.

III. DISCUSSION AND CONCLUSION

Table 2 provides a comparison of the proposed 2×4 array antenna with some recently reported ETC antennas. It can be seen that the proposed antenna has wider impedance bandwidth and AR bandwidth than almost all the other antennas 4–10], except for the antenna [25]. The high gain of 17 dBi is another merit of the proposed antenna compared to the other antennas. Also, unlike the proposed antenna, most of the other antennas do not have optimized beamwidths in order to cover the vehicle's mileage in a payment cycle. Moreover, the size of the proposed antenna is more compact than the antennas in [5, 6]. In summary, a novel nut-shaped unit cell was proposed to improve the proposed array antenna in terms of impedance and AR bandwidths, SLL, and gain in this study. The problem of interference and vehicle speed was considered in designing the proposed array antennas. The vehicle can pass the ETC with a speed of more than 100 Km/h. The SLL of the proposed antenna was optimized to be smaller than -15 dB by adding a reflector. By applying the sequential phase rotation feeding network, the proposed array antenna is low-profile with enhanced AR bandwidth. Moreover, the proposed array antenna was verified by measured results. It is found that the proposed 2×4 array antenna has met most of the requirements for ETC antennas, and therefore, it is a suitable candidate for RSUs in modern ETC systems.

Table 2: A performance comparison between the proposed 2×4 antenna with other studies

Ref.	Imp. BW (%)	AR BW (%)	Gain (dBi)	V-H HPBW (degree)	SLL (dB)	Size (mm^3)
[4]	34.48	19.4	14.7	23-23	−17	172×172×0.8
[5]	7.86	Nm	16.6	35.4-15.7	−12.5	200×180×0.8
[6]	1	Nm	14.9	33-33	−26	390×340×0.8
[7]	2.58	Not CP	12	40-40	−10	103×103×13
[8]	Nm	19.4	18	20-20	−16	Nm
[9]	3.73	LP	9.9	Nm	Nm	55×30×1.6
[10]	1.37	Nm	13	Nm	−12	Nm
[12]	37.75	35.52	17	33-17	−13	152×76×6.4
This work	37.73	32.9	17	34-17	−15.7	180×106×30

Not mentioned: Nm.

REFERENCES

[1] J. Czako, *Where is Tolling Tech Taking Us*? ITS International, https://www.itsinternational.com/its1/feature/where-tolling-tech-taking-us, 2019.

[2] CEN (European Committee for Standardization), "Road transport and traffic telematics – dedicated short-range communication – physical layer using microwave at 5.8GHz," Oct. 2004.

[3] ESTI (European Telecommunications Standards Institute), "Intelligent Transport Systems (ITS); Radiocommunications equipment operating in the 5 855 MHz to 5 925 MHz frequency band; Harmonized EN covering the essential requirements of article 3.2 of the R&TTE Directive," May 2013.

[4] T. Varum, J. N. Matos, P. Pinho, and R. Abreu, "Non-uniform broadband circularly polarized antenna array for vehicular communications," *IEEE Transactions on Vehicular Technology*, vol. 65, no. 9, pp. 7219-7227, Sep. 2016.

[5] B. Franciscatto, "Design and implementation of a new low-power consumption DSRC transponder," *Department of Electronics, University of Grennoble*, Grenoble, France, July 2014.

[6] J. S. Jang, N. H. Kang, Y. W. Koo, and J. K. Ha, "Planar array antenna design with beam shaping for ETCS-RSE," *Asia-Pacific Microwave Conference Proceedings (APMC)*, Seoul, Korea, Nov. 2013.

[7] N. Rimbault, A. Sharaiha, and S. Collardey, "Very low profile helix antenna feeding resonant cavity for ETC system," *16th International Symposium on Antenna Technology and Applied Electromagnetics (ANTEM)*, Victoria, BC, Canada, July 2014.

[8] Y. Zhao and L. Li, "Circular polarized Fabry-Perot resonator antenna for dedicated short range communication," *2014 IEEE International Wireless Symposium (IWS 2014)*, Xi'an, China, Mar. 2014.

[9] R. M. Kingsta and K. Seyatha, "Design and performance comparison of metamaterial superstrate antenna for DSRC applications," *3rd International Conference on Trends in Electronics and Informatics (ICOEI)*, Tirunelveli, India, Apr. 2019.

[10] T. Varum, J. N. Matos, R. Abreu, and P. Pinho, "Non-uniform microstrip antenna array for Rx DSRC communications," *IEEE Antennas and Propagation Society International Symposium (APSURSI)*, Memphis, TN, USA, 2014.

[11] Y. Zhao, "Circular polarized Fabry-Perot resonator antenna for dedicated short range communication," *IEEE International Wireless Symposium*, Xi'an, China, Dec. 2014.

[12] D. C. Khuat and T. L. Tran, "A high gain wideband array antenna based on metasurface for ETC application," *Transport and Communications Science Journal*, vol. 73, no. 7, pp. 723-733, Sep. 2022.

[13] N. Hussain, H. H. Tran, and T. T. Le, "Single-layer wideband high-gain circularly polarized patch antenna with parasitic elements," *AEU - International Journal of Electronics and Communications*, vol. 113, no. 1, Jan. 2020.

[14] M. S. Ibrahim, "Design of low-cost, circularly polarized, and wideband U-slot microstrip patch antenna with parasitic elements for WiGig and WPAN applications," *Applied Computational Electromagnetics Society (ACES) Journal*, vol. 34, no. 9, pp. 1453-1456, Sep. 2019.

[15] V. S. Kraanthi, R. B. Sandhya, P. V. Sitaraman, S. Aora, C. Sriharsha, K. V. Senthil, and D. Venkataramana, "High gain circularly polarized stacked patch antenna at C-band for GEO satellite telemetry application," *IEEE Indian Conference on Antennas and Propagation (InCAP)*, Ahmedabad, India, Dec. 2019.

[16] A. Michel, P. Nepa, and J. Qiu, "Compact dual-band circularly polarized stacked patch antenna for microwave-radio-frequency identification multiple-input-multiple-output application," *International Journal of Antennas and Propagation*, vol. 2021, pp. 1-13, May 2021.

[17] S. X. Ta and I. Park, "Low-profile broadband circularly polarized patch antenna using metasurface," *IEEE Transactions on Antennas And Propagation*, vol. 63, no. 12, pp. 5929-5934, Dec. 2015.

[18] J. Dong, C. Ding, and J. Mo, "A low-profile wideband linear-to-circular polarization conversion slot antenna using metasurface," *Materials Journal*, vol. 13, no. 5, pp. 1-13, Mar. 2020.

[19] L. Yuan, H. Y. Xuan, L. Z. Wei, C. S. Ting, X. X. Ming, and G. Jing, "Design of a compact wideband CP metasurface antenna," *International Journal of RF and Microwave Computer-Aided Engineering*, vol. 30, no. 10, pp. 1-8, Oct. 2020.

[20] Z. Tao, H. Zhang, H. Xu, and Q. Chen, "Novel polarization conversion metasurface based circular polarized slot antenna with low profile," *2019 Cross-Strait Quad-Regional Radio Science and Wireless Technology Conference*, Taiyuan, China, Aug. 2019.

[21] Q. Zheng, C. Guo, and J. Ding, "Wideband and low RCS circularly polarized slot antenna based on polarization conversion of metasurface for satellite communication application," *Microwave and Optical Technology Letters*, vol. 60, no. 3, pp. 679-685, Feb. 2018.

[22] C. Qiang and Z. Hou, "Dual-patch polarization conversion metasurface-based wideband circular polarization slot antenna," *IEEE Access*, vol. 29, no 5, pp. 74772-74777, Nov. 2018.

[23] M. T. Le, Q. C. Nguyen, and T. P. Vuong, "Design of high-gain and beam steering antennas using a new planar folded-line metamaterial structure," *International Journal of Antennas and Propagation*, vol. 2014, pp. 1-16, Sep. 2014.

[24] N. H. Nguyen, T. D. Bui, A. D. Le, A. D. Pham, T. T. Nguyen, Q. C. Nguyen, and M. T. Le, "A novel wideband circularly polarized antenna for RF energy harvesting in wireless sensor nodes," *International Journal of Antennas and Propagation*, vol. 2018, pp. 1-9, Mar. 2018.

[25] D. C. Khuat, V. L. Phi, and T. L. Tran, "A wideband high gain circularly polarized antenna based on nut-shape metasurface," *International Conference on Advanced Technologies for Communications (ATC)*, Hanoi, Vietnam, Oct. 2022.

[26] CST Microwave Studio, ver. 2018, Computer Simulation Technology, Framingham, MA, 2008.

[27] A. A. Abbas, B. S. Samet, and H. A. Abbas, "A compact high gain wideband metamaterial, antenna for sub-6 GHz applications," *Applied Computational Electromagnetics Society (ACES) Journal*, vol. 37, no. 8, pp. 886-892, Aug. 2022.

[28] B. Qiu1, Y. Xia, and Y. Li, "Gain-enhanced wideband circularly polarized antenna with a non-uniformmetamaterial reflector," *Applied Computational Electromagnetics Society (ACES) Journal*, vol. 37, no. 3, pp. 281-286, Mar. 2022.

[29] H. Q. Tian, J. L. Wang, D. Han, and X. Wang, "A gain-enhanced dual-band microstrip antenna using metasurface as superstrate configuration," *Applied Computational Electromagnetics Society (ACES) Journal*, vol. 36, no. 12, pp. 1586-1593, Dec. 2021.

[30] L. N. Nguyen, "A MIMO antenna with enhanced gain using metasurface," *Applied Computational Electromagnetics Society (ACES) Journal*, vol. 36, no. 4, pp. 458-464, Apr. 2021.

[31] A. Sethi and R. Rajni, "Determination of electromagnetic parameters of a new metasurface comprising of square loop," *Journal of Engineering Science and Technology*, vol. 13, no. 1, pp. 48-57, Jan. 2018.

Lan T. Tran was born in Haiphong, Vietnam, in 1988. She received her B.S. and M.S. degrees in telecommunication engineering from the University of Transport and Communications, Hanoi, Vietnam, in 2011 and 2013, respectively. She received her Ph.D. degree in computer, physics, and electrical engineering from Yokohama National University, Yokohama, Japan. She is now a lecturer at the University of Transport and Communications. Her current research interest is the design of antennas for wireless communication systems.

Chinh D. Khuat was born in Hanoi, Vietnam, in 2000. He is studying Electronic and Telecommunication Engineering at the University of Transport and Communications, Hanoi, Vietnam. His current research interest is the design of antennas for ETC systems and rectennas for RF energy harvesting.

Lam V. Phi received his B.E. and M.E. degrees in electrical and electronic engineering from the University of Transport and Communications, Hanoi, Vietnam, in 2011 and 2014, respectively. He received his Ph.D. degree in physics, electrical, and computer engineering from Yokohama National University, Yokohama, Japan, in 2019. His current research interests include robotics, AI, control theory, motion control, internet of thing (IoT) and intelligent transport system (ITS).

High-isolation Wi-Fi Antenna System based on Metamaterial

Zhihao Chen[1], Ziqin Wang[1], Fangyuan Chen[2], Xi Hou[1], Yonghong Zhou[3], and Lam Phav[4]

[1]School of Electronic Information Engineering
Xihua Normal University, Nanchong, Sichuan Province, 637000, China

[2]Jinyichang Science and Technology Co., Ltd.
Jiaxing, Zhejiang Province, 314000, China
fangyuanscu@gmail.com

[3]School of Higher Vocational & Technical Teachers
China West Normal University, Nanchong, Sichuan Province, 637000, China

[4]Ministry of Post and Telecommunications of Cambodia
Khan Daun Penh, Phnom Penh, 120210, Cambodia

Abstract – In this research, an inverted L shaped Wi-Fi antenna with a metamaterial (MTM) decoupling unit is proposed. This swirly-shaped antenna has a compact geometry size of 0.1 wavelength. The metamaterial decoupling unit is placed between the antenna elements to improve the isolation to reduce the mutual coupling. The antenna's isolation reached 20.7 dB from 2.4 GHz to 2.48 GHz, and 23.5 dB from 5.15 GHz to 5.85 GHz, after the metamaterial unit was introduced. This designed methodology reinforced the anti-interference capability. This compact and low-cost antenna is especially suitable for application in high-density Wi-Fi 6 systems.

Index Terms – decoupling, miniaturization, metamaterial, Wi-Fi.

I. INTRODUCTION

Wi-Fi technology is extensively employed in wireless communication, especially in the IoT (Internet of Things) system. MIMO (multiple-input multiple-output) technology is widely used in Wi-Fi systems, it enables the communication between the multiple access point and routers. The increasing antenna elements and miniaturization requirement is a contradiction of the antenna's high isolation requirement.

The common-mode theory and differential-mode theory are a widely used method to solve the antenna coupling problem. The isolation problem can be reduced by introducing two filters. While this method works on the circuit, it does not eliminate the coupling problem fundamentally [1]. The neutral line method is also widely employed in reducing the coupling effect, by introducing the cancellation effect within antenna elements [2–4]. Also, in Luo's study, the metamaterial unit is applied to alleviate the electromagnetic wave leak between the transmitting antenna and receiving antenna. The isolation improved by approximately 30 dB in this study. At present, there are many research papers on decoupling of Wi-Fi frequency bands [5–7]. However metamaterial is rarely employed in Wi-Fi systems.

In Ramya's study, a triple-band metamaterial absorber is introduced to reduce the radar cross-section problem [8]. In Almirall's study, a novel wearable metal material with high isolation ability is studied [9]. In Vosoughitabar's study, a novel two-dimensional time-modulated metamaterial transmitter is proposed, this design guaranteed a low bit error rate in an orthogonal frequency division multiplexing system [10].

Metamaterial is widely used in antenna design as well. Due to the negative refractive index properties of metamaterial, it is frequently employed in the improvement of the antenna's gain [11–13]. In Jha's paper [14], metamaterial is used to increase the operating bandwidth and reduce antenna sizes, and the electrical length is only $0.14\lambda*0.21\lambda$. In Singh's paper, a transmissive metamaterial is proposed as a planar lens, allowing microstrip antennas working on the metamaterial to improve gain by 8.55 dB in the H-plane and 6.20 dB in the E-plane at 10 GHz, respectively [15]. Zhang proposed a metamaterial array loaded with C-type on a dipole antenna to enable the gain improvement in the demanded frequency band. Metamaterial is also employed in microwave devices and transmission line design to reduce return loss [16].

In this research, a novel compact Wi-Fi antenna with an inverted L shape is proposed. The following contributions and novel areas are analyzed:

1. A smaller metamaterial structure is used to improve the isolation of the MIMO antenna.

2. The use of a CPW (coplanar waveguide) feed, which is easier to integrate into the equipment, and can reduce the dispersion effect.

3. The proposed antenna with a compact geometry size, with a mere $0.2\lambda*0.2\lambda$ size.

4. The FR4 dielectric substrate is used, which is low cost and is suitable for mass production.

5. The proposed antenna is suitable for Wi-Fi communication systems.

II. GEOMETRY AND CHARACTERIZATION OF ANTENNA

Figure 1 shows the antenna structure. The symmetric Wi-Fi radiation unit is located on the margin of the ground, the metamaterial unit is located between the radiation unit. The radiation unit and the metamaterial unit are parallel and vertical to the ground, which facilitates the soldering. The coupling waveguide is applied as the exciting port.
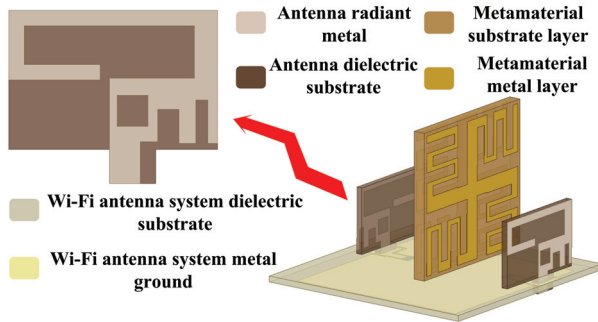

Fig. 1. Geometry structure of the antenna.

The Wi-Fi antenna is $9.5\times13.5\times0.8$ mm in size. FR4 (with a dielectric 4.4 and loss tangent 0.019) is employed for the antenna, MTM, and GND (ground). As shown in Fig. 2 (a), parasitic branches are placed on the Wi-Fi antenna to achieve dual-band communication, based on two different lengths of radiation branches to achieve resonance at 2.4 GHz and 5 GHz. Considering that the resonant cavity size of the planar antenna is large, the process of adjusting the resonance point and impedance matching is difficult, thus the inverted L antenna (ILA) is introduced in mobile devices due to its low cost and low profile. This design was inspired by the methodology from Tae [17].

As shown in Fig. 2 (b), the slot and bent structure are difficult to process due to the flexibility of the iron sheet. Meanwhile, the intrinsic impedance characteristic of iron has an apparent influence on electromagnetic radiation. Thus, the microstrip structure is employed, as
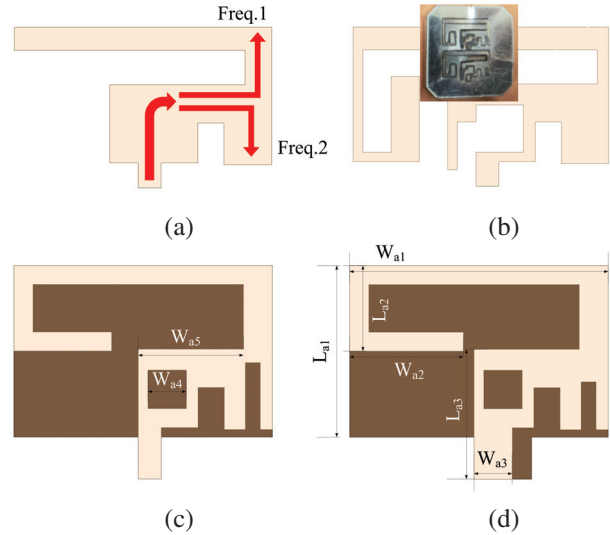

Fig. 2. Antenna evolution and the Wi-Fi antenna structure size: (a) Step 1, (b) Step 2, (c) Step 3, and (d) Step 4.

shown in Fig. 2 (c). The structure is elaborately designed to achieve the required communication band. For the convenience of mass production and installation, Parameter W_{a3} and antenna dielectric substrate geometry size are optimized, as shown in Fig. 2 (d). The E-shape metal patch lies on the right corner of the ground to expand the working frequency [18]. To achieve 2.4 GHz resonance in a compact size, the microstrip line is bent at the top left of the dielectric substrate to increase the electrical current length. The width of the coplanar waveguide and its gap distance is optimized based on the 2.4 GHz band to achieve the impedance match. The optimized parameters of the Wi-Fi antennas are $W_{a1} = 13.5$ mm, $W_{a2} = 5.9$ mm, $W_{a3} = 2$ mm, $W_{a4} = 2$ mm, $W_{a5} = 5.5$ mm, $L_{a1} = 9$ mm, $L_{a2} = 4.5$ mm, $L_{a3} = 6.8$ mm.

III. METAMATERIAL STRUCTURE AND THEORETICAL ANALYSIS

A. Theoretical analysis

Metamaterial is a kind of special artificial material, with equivalent negative permeability or dielectric constant. The performance of metamaterials mainly depends on the overall structure, size, dielectric thickness, incidence angle of excitation, electromagnetic wave, etc. This character empowers its geometry size which can be much more compact than the working frequency band [19]. Electromagnetic propagation in metamaterial is different from conventional material. Based on equation (1), the dot product of space electromagnetic wave propagation direction $\overrightarrow{S}$ and wave vector direction $\overrightarrow{k}$ gives a negative number when the permittivity ε and permeability μ are less than zero. Thus the electromagnetic wave propagation direction and energy flow are in opposite di-

rections in a specific frequency band under a specific metamaterial structure, from the time-harmonic electromagnetic wave theory.

$$\vec{k} \cdot \vec{S} = \frac{1}{2}\omega\varepsilon \left|\vec{E_0}\right|^2 = \frac{1}{2}\omega\mu \left|\vec{H_0}\right|^2. \quad (1)$$

Figure 3 displays the interference of the metamaterial to the electromagnetic wave propagation. The metamaterial can absorb and reflect wave energy in a certain condition. This character can be employed to improve antenna isolation. Based on the microwave theory [20], the refractive index n and impedance Z can be expressed with the S-parameters:

$$n = \frac{1}{kd}\cos^{-1}\left[\frac{1}{2S_{21}}(1 - S_{11}^2 + S_{21}^2) + 2\pi m\right], \quad (2)$$

$$Z = \sqrt{\frac{(1 + S_{11})^2 - S_{21}^2}{(1 - S_{11})^2 - S_{21}^2}}. \quad (3)$$

The refractive index and impedance can be obtained from the S parameters in a tow-port network, from equations (4) and (5), permittivity ε, permeability μ, and impedance Z with the following relationship:

$$\varepsilon = n/Z, \quad (4)$$
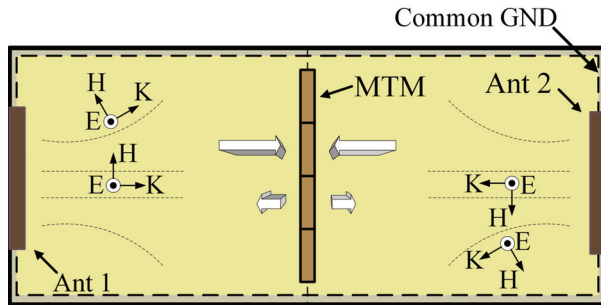
$$\mu = n \cdot Z. \quad (5)$$

Fig. 3. Wi-Fi antenna system electromagnetic wave coupling schematic.

When the propagation medium is a single negative material, as shown in equation (6), the refractive index is equivalent to a pure imaginary number, which proves that electromagnetic waves cannot propagate in this medium material.

$$n = i\sqrt{\varepsilon\mu}. \quad (6)$$

B. Metamaterial structure

Figure 4 shows the metamaterial unit. The metal patch on the material unit is in a finger cross shape, and in a central symmetric shape. In order to reduce the overall size of the metamaterial as much as possible, this design prints the same metamaterial metal layer on both sides of the metamaterial dielectric substrate to increase the gap and branch loading. The metal layer is on both sides
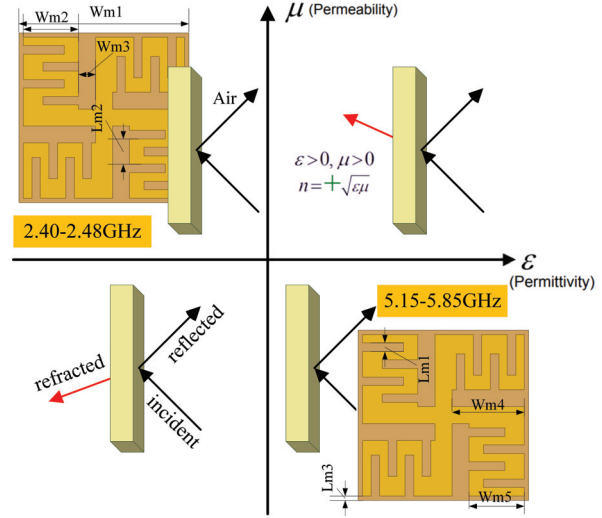

Fig. 4. Structure and properties of metamaterials.

of the 0.8 mm FR4 substrate. When the permittivity or permeability's value is smaller than zero, that is in the second coordinate or in the fourth coordinate, the metamaterial can absorb energy, as shown in Fig. 4.

As shown in Fig. 5, the metamaterial unit needs to be placed in a waveguide environment simulated by ANSYS Electronics. The boundary conditions of the waveguide model require that the upper and lower surfaces along the electric field direction are set as perfect electric wall (PEC), the front and rear surfaces along the magnetic field direction are set as perfect magnetic wall (PMC), and the left and right surfaces along the wave propagation direction are set as wave port excitation. It can be found that the obtained S21 is lower than -10 dB in the operating frequency band (2.4-2.48/5.15-5.85 GHz), and has obvious stop band characteristics.
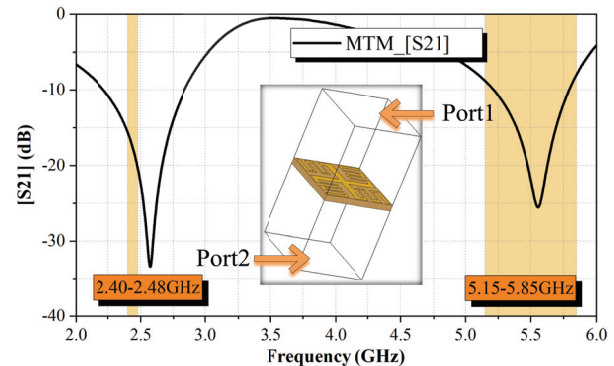

Fig. 5. MTM stop band characteristics.

As shown in Fig. 6, after obtaining the S-parameters of the two-port metamaterial cell based on the Finite In-
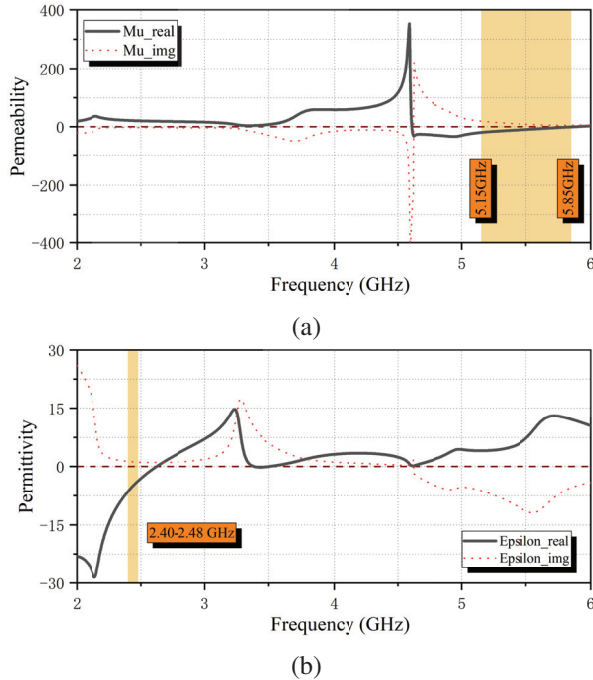
(a)

(b)

Fig. 6. (a) Metamaterial equivalent permeability (real part and imaginary part) and (b) Metamaterial equivalent dielectric constants (real part and imaginary part).

tegration Technique, the transformation matrix method is then used to derive the permeability and permittivity. In this design, the permittivity is smaller than zero from 2.4 GHz to 2.48 GHz, and the permeability is smaller than zero from 5.15 GHz to 5.85 GHz. In these two frequency bands, the metamaterial belongs separately to ENG (Epsilon Negative) and MNG (Mue-Negative) media, respectively. It can be proved, based on equation (6), that a specific frequencies wave cannot propagate in the media. So, in theory the material can absorb the electromagnetic wave in the corresponding frequency band and improve the antenna isolation level. The optimized parameters of the metamaterial are W_{m1} = 20 mm, W_{m2} = 5.8 mm, W_{m3} = 2 mm, W_{m4} = 8.5 mm, W_{m5} = 6.5 mm, L_{m1} = 1.4 mm, L_{m2} = 2.6 mm, L_{m3} = 0.5 mm.

IV. PARAMETERS ANALYSIS

In this study, the inverted L-bent branches are considered as a basic design structure. The equivalent capacity between the antenna branch and the ground needs to be reduced to ensure good radiation performance at low-frequency band. As shown in Fig. 7, the S_{11} is reduced when L_{a2} gets smaller. The return loss performance at 2.44 GHz reached the requirement when L_{a2} is 4.5 mm.

The isolation performance in the condition of the metamaterial unit and metal layer are compared. As shown in Fig. 8, the S_{21} is -11.6 dB at 2.4 GHz in the absence of metamaterial, and S_{21} is larger than -20 dB.
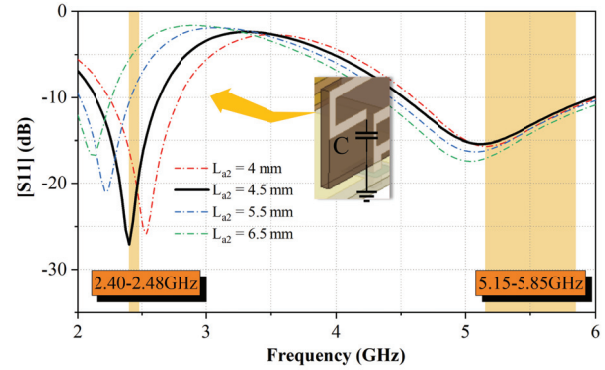

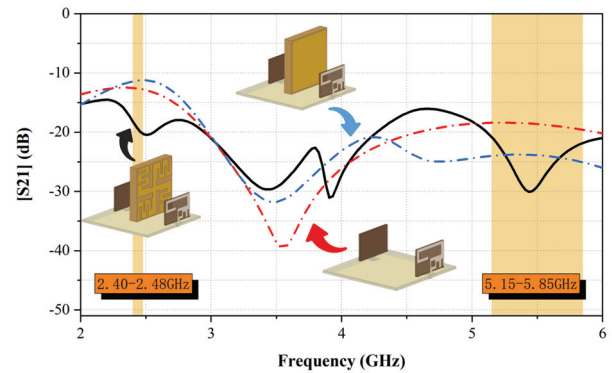Fig. 7. Simulated S_{11} from different geometry size L-bent branches.

Fig. 8. Simulated S_{21} about comparing metamaterial unit and metal baffle.

Between 5.15 GHz and 5.85 GHz, the isolation improves after the metal layer is introduced in the middle of the antenna while the isolation at the lower frequency band gets larger. The isolation is smaller than -20 dB both in the lower frequency and higher frequency after the metal material unit is introduced. So this designed metamaterial unit has a positive effect in reducing the electromagnetic wave coupling effect.

The antenna can be regarded as a combination of a curve-type capacitance and inductance [21]. The metamaterial structure is optimized to ensure the best performance in the improvement of antenna isolation. As shown in Fig. 9, the center working frequency is left-shifted with the increase of W_{m2}. S_{21} has the best performance when W_{m2} is 4.8 mm. As shown in Fig. 4, the overall inductance increases when W_{m2} gets larger, thus the resonance frequency band is left-shifted. In this study, a metal layer is optimized to improve the metamaterial performance, this methodology improves the isolation at low frequencies in a limited space with great value to the MIMO antenna design.
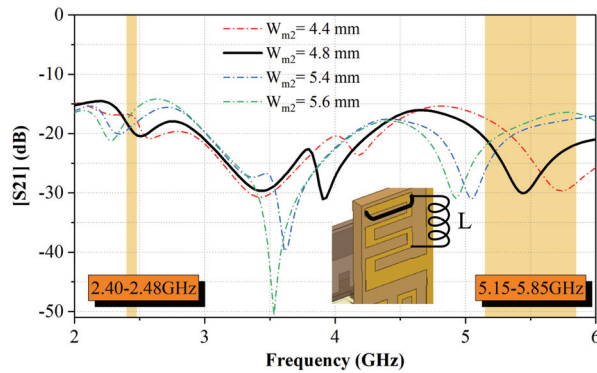
Fig. 9. Simulated S_{21} from different geometry size W-bent branches.

V. RESULTS AND ANALYSIS

The simulated and measured VSWR(voltage standing wave ratio)of these two Wi-Fi antennas are shown in Fig. 10. These two curves with a great agreement with each other, but with a small discrepancy. This discrepancy is from the testing error and manufacturing. The frequency band in the condition of VSWR<3 covers the entire Wi-Fi bands for the measured results. As shown in Fig. 11, the isolation drops from -8 dB to -19.3 dB at 2.4 GHz when the metamaterial is introduced and placed at the adjusted position. The isolation at higher Wi-Fi frequency drops from -16.6 dB to -18.2 dB, this value satisfies the requirement of -15 dB in engineering applications.
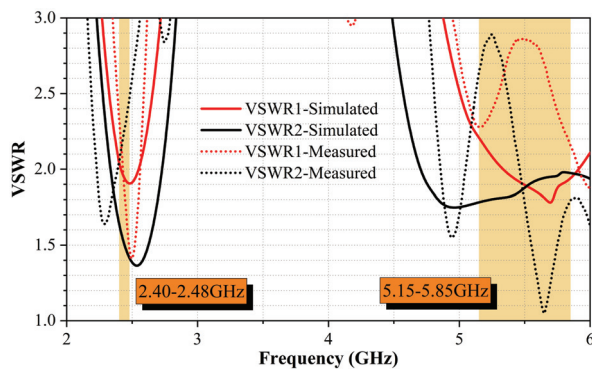

Fig. 10. Simulated and measured VSWR.

As shown in Fig. 12, the simulated and measured antenna working efficiency is higher than 79%. The maximum antenna gain is 6 dBi at 2.4 GHz, and 8 dBi at 5 GHz. This is an excellent performance for an electric small antenna. We used a SATIMO multi-probe near-field antenna measurement system as shown in Fig. 13, which is different from traditional far-field measurement systems. It provides faster and more accurate test results. The radiation pattern is measured in a 5m×5m×5m
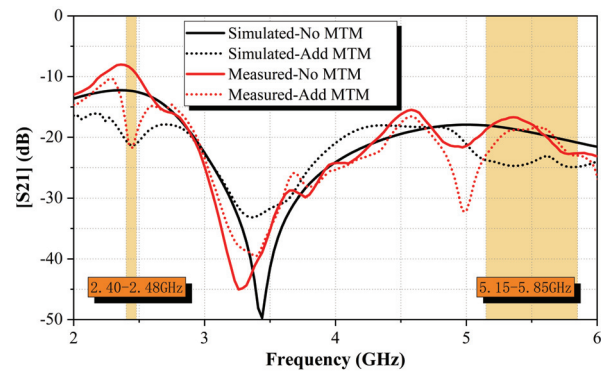

Fig. 11. Simulated and measured antenna isolation.

specially designed near-field anechoic chamber with 24 near-field EM probes for antenna device testing.
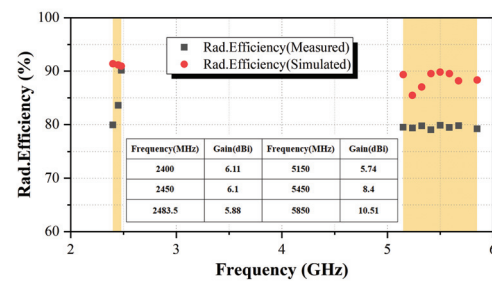

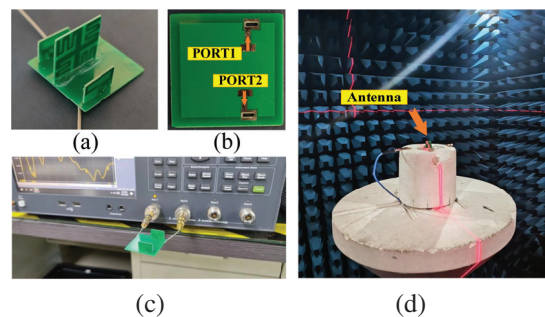Fig. 12. Measured and simulated antenna efficiencies and gain.

Fig. 13. Antenna and the testing environment (a) antenna, (b) antenna feed position, (c) reflection coefficient test with vector network analyser, and (d) antenna measurement in the microwave anechoic chamber.

Figure 14 shows the antenna radiation performance of the E plane and H plane, both at 2.45 GHz and 5.4 GHz. This antenna is tested in a near-field microwave anechoic chamber, with 32 microwave probes. It can be seen this antenna system is omnidirectional and has a good radiation characteristic.
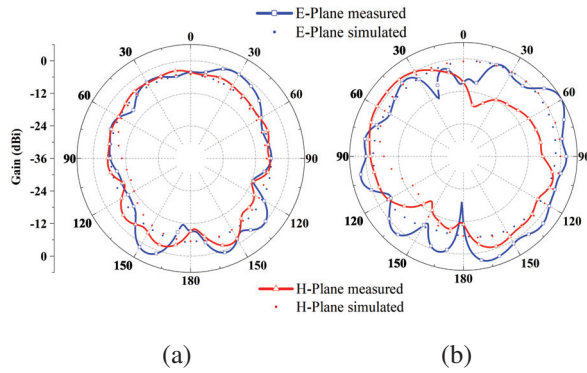
Fig. 14. Measured and simulated radiation patterns: (a) 2450 MHz and (b) 5400 MHz.

The corresponding relation between ECC(Envelop Correlation Coefficien) and frequency of the two-port MIMO antenna system proposed in this paper is shown in Fig. 15. It can be seen that at the operating frequency, the ECC parameter is lower than 0.2, which is considered as the optimal performance of the MIMO antenna in engineering.
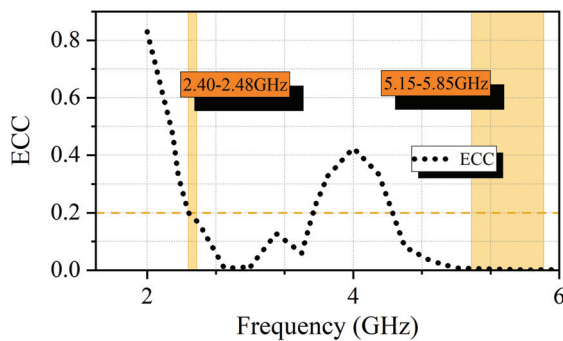

Fig. 15. The tested ECC at work frequency band.

As shown in Table 1, the proposed Wi-Fi antenna in this research has better isolation compared with previous studies. This MIMO antenna's frequency covers the entire Wi-Fi band, and with vertical placement. This design elaborately utilizes a small space and has guaranteed vertical polarization performance.

Figure 16 compares the influence of metamaterial structure on the radiation pattern of Wi-Fi antenna. It can be seen that the radiation intensity in direction A at 2.4 GHz is increased to a certain extent after the introduction of the metamaterial structure. The antenna radiation intensity is decreased in direction B at frequency 2450 MHz and 5400 MHz, which conforms to the characteristics of the ENG (Epsilon Negative) dielectric and the MNG (Mue-Negative) dielectric. So it is derived that the electromagnetic wave cannot propagate in the two media.

Table 1: Performances comparison with relevant studies

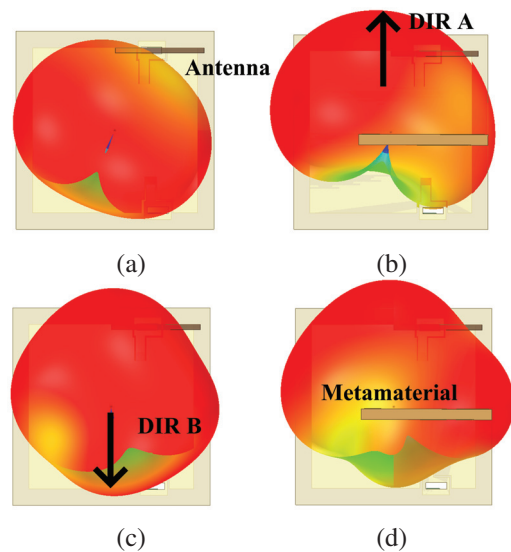| Ref	Distance (mm)	Number of Antennas	Working Frequency Band	Isolation (dB)
[22]	35 mm (0.28 λ)	2	2.40-2.48 GHz	<-17.9 dB
[23]	25 mm (0.08 λ)	2	1-25 GHz	<-10 dB
[24]	20 mm (0.16 λ)	4	2.40-2.69 GHz/3.4-3.69 GHz	<-10 dB
[25]	30 mm (0.34 λ)	4	3.4-3.7 GHz	<-10 dB
[26]	40 mm (0.43 λ)	2	3.2-3.8 GHz/5-6.8 GHz	<-18 dB
[27]	48 mm (0.44 λ)	8	3.3-6 GHz	<-11 dB
Prop.	25 mm (0.2 λ)	2 (without metamaterial)	2.40-2.48 GHz/5.15-5.85 GHz	<-8 dB
	25 mm (0.2 λ)	2 (with matematerial)		<-19.3 dB

Fig. 16. Measured 3D radiation patterns: (a) no MTM in 2450 MHz MTM, (b) with MTM in 2450 MHz, (c) no MTM in 5400 MHz, and (d) with MTM in 5400 MHz.

VI. CONCLUSION

In this work, a high isolation co-ground and dual band Wi-Fi antenna based on metamaterial is proposed.

The isolation in the Wi-Fi frequency band improved with the introduction of the proposed material and verified the effectiveness of the proposed metamaterial absorber. This design solved the microwave interference problem of the MIMO antenna. This design methodology also works on the antenna decoupling system. This antenna is compact, with a $30 \times 30 \times 20$ mm size, and with a simple feeding method. In addition, the antenna has high radiation efficiency ($\eta > 79\%$) and high isolation ($S_{21} > $ -16 dB) so is very suitable for application in Wi-Fi devices.

ACKNOWLEDGMENT

REFERENCES

[1] W. Zhang, Y. Li, K. Wei, and Z. Zhang, "A two-port microstrip antenna with high isolation for Wi-Fi 6 and Wi-Fi 6E applications," *IEEE Transactions on Antennas and Propagation*, vol. 70, no.7, pp. 5227-5234, Jan. 2022.

[2] R. Liu, X. An, H. Zhang, M. Wang, Z Gao, and E. Lei, "Neutralization line decoupling tri-band multiple-input multiple-output antenna design," *IEEE Access*, vol. 8, pp. 27018-27026, Feb. 2020.

[3] D. Saxena, A. Kumar, R. K. Verma, and P. Jha "Metamaterial inspired dual band MIMO antenna with open-ended slot and neutralized line for isolation enhancement," *IEEE 10th International Conference on Signal Processing and Integrated Networks (SPIN)*, Noida, India, pp. 727-732, May 2023.

[4] A. Kumar, C. Tyagi, D. Saxena, and P. Jha, "Miniaturized two-element MIMO antenna with neutralization line and an asymmetric open slot for WLAN and IOT applications," *IEEE International Conference on Artificial Intelligence and Smart Communication (AISC)*, Greater Noida, India, pp. 227-231, Apr. 2023.

[5] P. Jha, A. Kumar, A. De, and R. K. Jain, "Flexible and textile two-port compact antenna for WLAN and wearable applications," *IEEE 8th International Conference on Signal Processing and Integrated Networks (SPIN)*, Noida, India, pp. 308-311, Aug. 2021.

[6] P. Jha, A. Kumar, A. De, and R. Jain, "Two-port miniaturized textile antenna for 5G and WLAN applications," *International Journal of Microwave and Wireless Technologies*, pp. 1-10, Apr. 2023.

[7] A. Kumar, D. Saxena, P. Jha, and N. Sharma, "Parasitic and open slot-based circular polarized two-port antenna for ISM applications," *IEEE International Conference on Artificial Intelligence and Smart Communication (AISC)*, Greater Noida, India, pp. 332-337, Apr. 2023.

[8] S. Ramya and I. S. Rao, "Design of new metamaterial absorber with triple band for radar cross section reduction," *IEEE Fifth International Conference on Advances in Computing and Communications (ICACC)*, Kochi, India, pp. 303-306, Mar. 2015.

[9] O. Almirall, R. Fernández-García, and I. Gil, "Wearable metamaterial for electromagnetic radiation shielding," *The Journal of the Textile Institute*, vol. 113, no. 8, pp. 1586-1594, June 2021.

[10] S. Vosoughitabar, A. Nooraiepour, W. Bajwa, N Mandayam, and C. Wu, "Metamaterial-enabled 2D directional modulation array transmitter for physical layer security in wireless communication links," *IEEE/MTT-S International Microwave Symposium-IMS*, Denver, CO, USA, pp. 595-598, June 2022.

[11] I. U. Din, S. Ullah, S. I. Naqvi, R. Ullah, E. Ali, and M. Alibakhshikenari, "Improvement in the gain of UWB antenna for GPR applications by using frequency-selective surface," *International Journal of Antennas and Propagation*, Oct. 2022.

[12] S. Kundu, A. Chatterjee, and S. K. Jana, "Gain enhancement of a printed leaf shaped UWB antenna using dual FSS layers and experimental study for ground coupling GPR applications," *Microwave and Optical Technology Letters*, vol. 60, no. 6, pp. 1417-1423, Apr. 2018.

[13] B. Qiu, Y. Xia, and Y. Li, "Gain-enhanced wideband circularly polarized antenna with a non-uniform metamaterial reflector," *Applied Computational Electromagnetics Society (ACES) Journal*, vol. 37, no. 3, pp. 281-286, July 2022.

[14] P. Jha, A. Kumar, A. De, and R. K. Verma, "CPW-fed metamaterial inspired compact multiband antenna for LTE/5G/WLAN communication," *Frequenz*, vol. 76, no. 7, pp. 401-407, Mar. 2022.

[15] A. K. Singh, M. P. Abegaonkar, and S. K. Koul, "A negative index metamaterial lens for antenna gain enhancement," *2017 International Symposium on Antennas and Propagation (ISAP)*, Phuket, Thailand, pp. 1-2, Nov. 2017.

[16] F. Zhang, Q. Wu, and J. C. Lee, "Miniaturized microstrip-based metamaterials quasi-standard transmission lines unit," *IEEE Proceedings of 2012 5th Global Symposium on Millimeter-Waves*, Harbin, China, pp. 629-632, May 2012.

[17] H. Tae, K. Oh, W. Son, W. Lim, and J. Yu, "Design of compact dual-band quadruple inverted-F/L antenna for GPS L1/L2 band," *IEEE Transactions*

on Antennas and Propagation, vol. 61, no. 4, pp. 2276-2279, Apr. 2013.

[18] F. Yang, X. Zhang, X. Ye, and Y. Rahmatsamili, "Wide-band E-shaped patch antennas for wireless communications," *IEEE Transactions on Antennas and Propagation*, vol. 49, no. 7, pp. 1094-1100, July 2001.

[19] X. Zhu, X. Yang, Q. Song, and B. Liu, "Compact UWB-MIMO antenna with metamaterial FSS decoupling structure," *EURASIP Journal on Wireless Communications and Networking*, vol. 2017, no. 1, pp. 1-6, Dec. 2017.

[20] X. Chen, T. M. Grzegorczyk, B. I. Wu, J. Pacheco, and J. Kong, "Robust method to retrieve the constitutive effective parameters of metamaterials," *Physical Review E*, vol. 70, no. 1, July 2004.

[21] L. Kurra, M. P. Abegaonkar, A. Basu, and S. Koul, "FSS properties of a uniplanar EBG and its application in directivity enhancement of a microstrip antenna," *IEEE Antennas and Wireless Propagation Letters*, vol. 15, pp. 1606-1609, Jan. 2016.

[22] I. Gil and R. Fernández-García, "Study of metamaterial resonators for decoupling of a MIMO-PIFA system," *IEEE 2016 International Symposium on Electromagnetic Compatibility-EMC EUROPE*, pp. 552-556, Sep. 2016.

[23] A. Armghan, K. Aliqab, V. Sorathiya, F Alenezi, M. Alsharari, and F. Ali, "Design and fabrication of the split ring resonator shaped two-element MIMO antenna with multiple-band operation for WiMAX/5G/Zigbee/Wi-Fi applications," *Micromachines*, vol. 13, no. 12, pp. 2161-2170, Dec. 2022.

[24] R. Hussain, A. Raza, M. Khan, and M. Sharawi, "Miniaturized frequency reconfigurable pentagonal MIMO slot antenna for interweave CR applications," *International Journal of RF and Microwave Computer-Aided Engineering*, vol. 29, no. 9, pp. 11-21, Apr. 2019.

[25] A. Kholapure and R. Karandikar, "Printed MIMO antenna with reconfigurable single and dual band notched characteristics for cognitive radio," *IEEE International Conference on Antenna Innovations & Modern Technologies for Ground, Aircraft and Satellite Applications (iAIM)*, Bangalore, India, pp. 1-5, Nov. 2017.

[26] R. Verma and A. Kumar, "WI-FI reconfigurable dual band microstrip MIMO antenna for 5G and WI-FI WLAN applications," *Przeglad Elektrotechniczny*, July 2021.

[27] J. He, S. Zhu, J. Yu, H. Li, and G. Li, "Wideband decoupled 8-element MIMO mobile phone antenna for sub-6GHz 5G NR bands," *Applied Computational Electromagnetics Society (ACES) Journal*, vol. 37, no. 12, pp. 1208-1215, 2022.

Zhihao Chen received his B.E. degree in Communication Engineering from China Jiliang University, HangZhou, China, in 2021. Since 2021 he has been pursuing a master's degree in Electronic Information Engineering, at China West Normal University, Nanchong, China. He was a teaching assistant at the same university. His research interests include microwave theory and technology, and antenna design.

Ziqin Wang received his B.E. degree in Applied Electronic Engineering from China West Normal University, Nanchong, China, in 2020. Since 2021 he has been pursuing a master's degree in Electronic Information Engineering, at the same university. He was an intern at Jinyichang Science & Technology from 2022 to 2023. His research interests include microwave theory, numerical computation in electromagnetics, and antenna design.

Fangyuan Chen received his Ph.D degree in Radio Physics at Sichuan University, Chengdu, China, in 2016. From 2013 to 2015 he was a visiting doctoral student at Cornell University, New York, USA. Now he is the deputy chief engineer of Jinyichang Science & Technology Co., Ltd. Currently, he is responsible for strategic technology development in V2X network architecture design, multi-band frequency antenna design. His research interests are microwave theory and technology, and optimization algorithms.

Xi Hou is currently pursuing an M.D. degree at the School of Electronic Information Engineering, China West Normal University. She worked on CITIC's Engineer of Excellence program. Her current research interests include antenna and metasurfaces and their applications.

Yonghong Zhou received his M.S. degree in Computer Applications Technology and his Ph.D. degree in Radio Physics from Southwest Petroleum University and Sichuan University, Chengdu, China, in 2005 and 2017, respectively. He joined the teaching staff in 2005 and is currently a Professor with the School of Electronic Information Engineering, China West Normal University. His research area include microstrip antennas, electromagnetic metasurfaces and their applications, and numerical methods applied in electromagnetics.

Lam Phav received his B.E degree in Computer Science and Engineering, from the Royal University of Phnom Penh, Cambodia, in 2004. He received his M.Sc. degree in Communication Information Systems, from Sichuan University, Chengdu, Sichuan, China, in 2013. Currently he is working at the General Department of Information and Communication Technology, Ministry of Post and Telecommunications (MPTC), Phnom Penh, Cambodia. His research intetrests are antenna theory and design, and wireless communication technology.

Temperature Controlled Terahertz Absorbers based on Omega Resonators

Jia-Tong Jing[1], Wei Song[1], Ting-Ting Ge[1], Xin-Qing Sheng[1], Aliaksei Balmakou[2], and Sergei Khakhomov[2]

[1]Institute of Radio Frequency Technology and Software
Beijing Institute of Technology, Beijing, 100081, China
3120215362@bit.edu.cn, wsong@bit.edu.cn, 18810669611@163.com, xsheng@bit.edu.cn

[2]Departments of Optics
Francisk Skorina Gomel State University, Gomel, 246028, Belarus
balmakou@gmail.com, khakh@gsu.by

Abstract – In this article, the structural stability of a metasurface absorber that works at 2.8 THz is analyzed. Since the absorber is made of metallic titanium, its elemental inclusions will be heated up and expand when absorbing electromagnetic waves. To evaluate the accumulated heat, the structural thermal expansion and the stability of the wave-absorbing performance, electromagnetism-thermodynamics-structural mechanics multiphysics simulations are conducted. Based on the thermal stability study, thermistors are further introduced into the metasurface, leading to two thermal controlled terahertz absorbers. Numerical experiments show that the absorbers present a peak absorption coefficient of 92.7% at 2.79 THz up to the temperature of 1761.4 K. When the temperature rises, the absorption frequencies of the two absorbers shift to 3.51 THz and 3.94 THz, with the peak absorption coefficients of 92.8% and 93.8%, respectively.

Index Terms – multiphysics simulations, thermal controlled terahertz absorbers, thermal expansion.

I. INTRODUCTION

Electrically thin absorbing metasurfaces are of prime importance for many applications, for example, wave filtering [1, 2], radar cross-section reduction [3–6], energy harvesting [7–10], phase modulating [11, 12], and thermal emission control [13–15]. Total absorption of electromagnetic radiation requires elimination of all wave propagation channels: reflection and transmission. The electromagnetic behavior of any arbitrary scatterer may be described by its polarizability tensors [16]. Polarizability tensors determine the linear relation between induced dipole moments and exciting electromagnetic fields. There are various analytical and numerical approaches for calculation of polarizability tensors of scatterers [17–19]. Correspondingly, electrically thin

absorbers are proposed [20]. Among these structures, the Ω-shaped metallic resonator is interesting because it demonstrates nearly full absorption for EM waves [21]. Moreover, it can be fabricated by laser lithography methods with subsequent metallization or ion beam-selective etching. So it has potential applications in spatial light modulators, sensors, bolometers and so on [20, 22]. However, there remain two interesting problems.

First, the absorption of electromagnetic waves is based on metallic loss which converts electromagnetic energy into thermal energy. During the process of EM wave absorbing, the heated metal structure may expand. That will affect the polarizability of the metasurface. Especially when metallic contact between the inclusions occurs, the polarizability will be changed dramatically, which would lead to a significant change in the absorbing function of the metasurface absorber. However, to the best of our knowledge, there are few studies on the thermal stability of the absorption.

Second, known from the causality principle, the maximal bandwidth of absorption of a passive absorbing layer is proportional to the layer thickness [23, 24]. So the full absorption of the metasurface exists only in a narrow frequency band, and the band is fixed once the structure of the metasurface is determined. Therefore, dynamically controlling the absorption band remains an interesting topic.

In this paper, we first investigated the thermal stability of a terahertz absorber based on Ω-shaped titanium resonators. An electromagnetism-thermodynamics-structural mechanics multiphysics simulation is conducted. The simulation results show that up to the melting temperature of titanium, the absorber demonstrates stable absorption.

Second, based on the analysis of polarizability, we incorporated thermistors in the Ω resonators and obtained temperature-controlled EM absorbers. In this

way, the absorption frequency can be shifted by controlling the temperature. Absorption coefficients of over 90% for all the bands are demonstrated in the simulations.

II. METASURFACE ABSORBING THEORY

Consider a metasurface absorber operating at 2.8 THz as proposed in [21]. The metasurface is formed with unit cells in a square lattice, with lattice constants of 37 μm. Each unit cell consists of four pairs of orthogonally arranged Ω-shaped titanium wires as shown in Fig. 1. The diameter of each Ω is 1/7 wavelength.
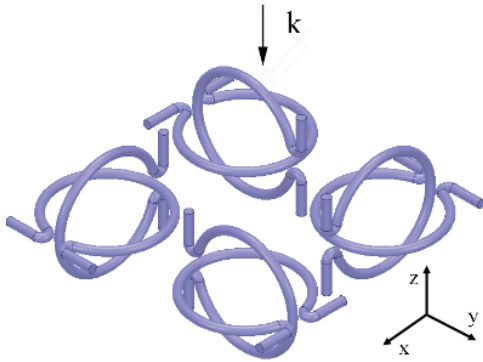

Fig. 1. Schematic of the array of pairs of Ω particles.

Illuminated normally by an incident plane wave, the induced electric and magnetic dipole moments p and m can be modelled with the help of polarizability [16]. Due to the subwavelength dimensions of the array elements, the dipole moments and polarizabilities can be described using the effective surface-averaged values:

$$\begin{bmatrix} p \\ m \end{bmatrix} = \begin{bmatrix} \hat{\alpha}_{ee} & \hat{\alpha}_{em} \\ \hat{\alpha}_{me} & \hat{\alpha}_{mm} \end{bmatrix} \begin{bmatrix} E_{inc} \\ E_{inc} \end{bmatrix}. \tag{1}$$

Here $\hat{\alpha}_{ee}$, $\hat{\alpha}_{em}$, $\hat{\alpha}_{me}$ and $\hat{\alpha}_{mm}$ are the effective electric, electromagnetic, magnetoelectric and magnetic polarizability tensors of the unit cells.

As shown in [20], the electric fields of the reflected and transmitted waves from this metasurface are given by:

$$E_r = \frac{i\omega}{2S}\left(\eta_0\hat{\alpha}_{ee} - \frac{1}{\eta_0}\hat{\alpha}_{mm}\right)E_{inc} \tag{2}$$

$$E_t = \left[1 + \frac{i\omega}{2S}\left(\eta_0\hat{\alpha}_{ee} + \frac{1}{\eta_0}\hat{\alpha}_{mm}\right)\right]E_{inc}, \tag{3}$$

where ω is the angular frequency, S is the area of the unit cell, and η_0 is the free-space wave impedance.

Requiring $E_r = 0$ and $E_t = 0$ in equations (2-3), one can find the conditions of symmetric total absorption in a metasurface:

$$\eta_0\hat{\alpha}_{ee} = \frac{1}{\eta_0}\hat{\alpha}_{mm} = i\frac{S}{\omega}. \tag{4}$$

By introducing the normalized polarizabilities,

$$\begin{bmatrix} \tilde{\alpha}_{ee} & \tilde{\alpha}_{em} \\ \tilde{\alpha}_{me} & \tilde{\alpha}_{mm} \end{bmatrix} = \begin{bmatrix} \eta_0\hat{\alpha}_{ee} & \hat{\alpha}_{em} \\ \hat{\alpha}_{me} & \frac{1}{\eta_0}\hat{\alpha}_{mm} \end{bmatrix}, \tag{5}$$

(4) can be transformed into a simpler form

$$\tilde{\alpha}_{ee} = \tilde{\alpha}_{mm} = i\frac{S}{\omega}. \tag{6}$$

This means the normalized electric polarizability should be equal to the normalized magnetic polarizability. Furthermore, the electric and magnetic resonance must coincide in frequency in order to demonstrate simultaneous purely imaginary electric and magnetic polarizabilities.

The thickness of the metasurface is 17 μm, which is negligible compared to structure dimensions in the xOy plane. Therefore, omitting the z-component, $\tilde{\alpha}_{ee}$ can be expressed as:

$$\tilde{\alpha}_{ee} = \begin{bmatrix} \tilde{\alpha}_{ee}^{xx} & \tilde{\alpha}_{ee}^{xy} \\ \tilde{\alpha}_{ee}^{yx} & \tilde{\alpha}_{ee}^{yy} \end{bmatrix}, \tag{7}$$

$\tilde{\alpha}_{em}$, $\tilde{\alpha}_{me}$ and $\tilde{\alpha}_{mm}$ can be expressed similarly.

III. STABILITY ANALYSIS OF THE METAMATERIAL ABSORBER

To study the thermal stability of the absorber, an electromagnetism-thermodynamics-structural mechanics multiphysics simulation was conducted by the COMSOL Multiphysics software. The radio frequency module, the heating module and the solid mechanics module were used in the simulation.

The material of the inclusions used in the unit cell (Fig. 1) is titanium, which has a conductivity of $\sigma = 7.407 \times 10^5$ S/m, a thermal expansion coefficient of 7.06×10^{-6} 1/K, and a melting temperature of 1941.15 K. The unit cell is surrounded by periodic boundary conditions in the x- and y-directions. In the z-direction, the PML (Perfectly Matched Layer) boundaries are applied. In the radio frequency module, a y-polarized plane wave incidence with frequency of 2.8 THz is set to impinge from the +z direction. In the heating module, the heat source is internal Joule heat. The convective heat flux is used with a heat transfer coefficient of 10 and an initial temperature of 293.15 K (room temperature). In the solid mechanics module, one end of the straight section in the Ω ring is fixed. To be specific, the bottom end for each vertical Ω ring is fixed. For each horizontal ring, the end close to the lattice boundary is fixed.

When the incident EM power is set to be $P_{inc} = 500$W/m^2 and $P_{inc} = 10000$W/m^2, the simulated steady-state temperature is plotted in Fig. 2.

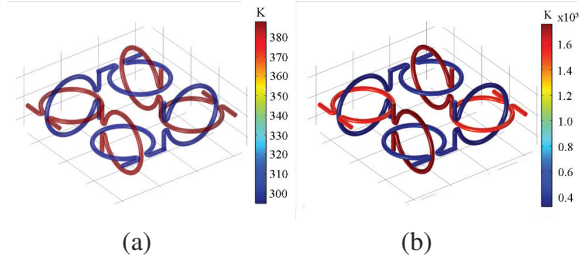For the y-polarized incidence, only one in each Ω pair gets heated. Further simulation shows that the other

Fig. 2. Corresponding temperature distribution, (a) in 500 W/m^2 and (b) in 10000 W/m^2.

half of the absorber gets heated with x-polarized incidence and is not plotted here. On each heated Ω-shaped inclusion, the heat distribution is uniform. For the $P_{inc} = 500$W/m^2 case, the steady temperature is 387.5 K. That temperature increases to 1761.4 K when the incident power density reaches 10000 W/m^2.

The corresponding expansion of the heated metamaterial absorber is plotted in Fig. 3. For each heated Ω ring, metallic expansion mainly occurs in the circular area.
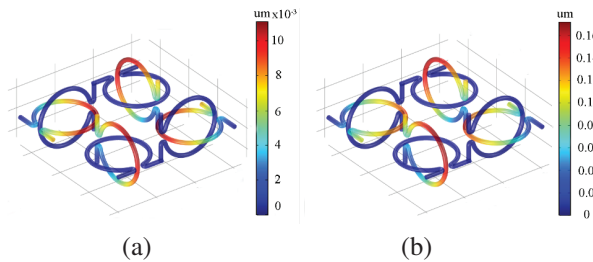

Fig. 3. Corresponding displacement in different powers, (a) in 500 W/m^2 and (b) in 10000 W/m^2.

The absorption coefficient A of the absorber can be obtained from the simulated reflection coefficient R and the transmission coefficient T [21], as presented in Fig. 3.

The maximum expansion in the diameter of the Ω ring D, and the expansion rate with respect to the radius of the Ω ring (D/R) with the corresponding steady-state temperature and absorption rate are summarized in Table 1.

We can see that with a steady-state temperature of 387.5 K, the maximum expansion on the Ω ring is in the order of nanometers. For the case with a steady-state temperature of 1761.4 K, the maximum expansion is in order of 0.1 micrometer. With such expansion on the circular section, the deformation is not so big as to cause physical connection among Ω wires which might lead to dramatic change in the polarizabilities. That is why the absorption coefficient remains almost unchanged in the simulation results.

We further studied the condition that the expansion of the metal does cause the contact between the inclu-
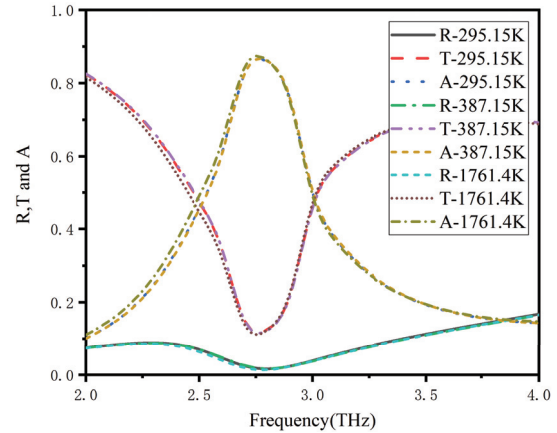

Fig. 4. Simulated reflection R, transmission T, and absorption A coefficients for the absorber, at temperature of 295.15 K, at temperature of 387.15 K and at temperature of 1761.4 K.

Table 1: Simulated peak expansion in structure and absorption at steady-state temperature

Temperature (K)	D (μm)	D/R (%)	Operating Frequency (THz)	A (%)
295.15	0	0	2.79	86.9
387.8	0.011	0.17	2.79	86.9
1761.4	0.17	2.58	2.79	86.9

sions. Simulations show that only when the temperature reaches 10000 K, will the Ω particles touch each other. Taking the melting temperature of titanium (1941.15 K) into account, we arrive at the conclusion that, up to the melting temperature of the material, the absorber is thermally stable.

IV. DESIGN AND SIMULATION RESULTS OF METASURFACE ABSORBERS

A. Design of metasurface absorbers

Based on the above thermal stability analysis, we present here the scheme to design temperature controlled metasurface absorbers by incorporating thermistors. In this scheme, the heat source may originate from the Joule heat transformed from the EM wave absorption by the Ω absorber itself, or it can be added manually through a heat conducting medium. Under this scheme, two examples are provided. As can be seen from Fig. 5, thermistors are introduced in the unit cells. In this way the functions of the metasurfaces may be dynamically controlled by temperature. Such thermistors can be realized by materials such as VO$_2$ [25, 26], which has an isolator phase and metallic phase with the transition temperature of around 320 K. As is shown in [25], the corresponding dynamic

range of the effective conductivity of VO$_2$ film is 10^1-10^5 S/m. So for the themistors, we used equivalent models of open circuits and short circuits at different temperatures.

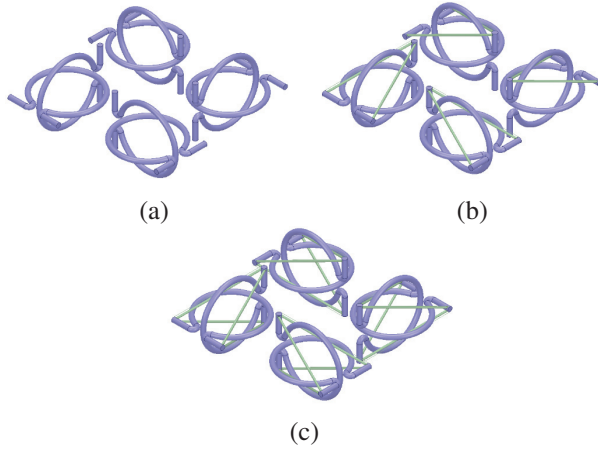(a)   (b)

(c)

Fig. 5. Schematic of the designed absorbers, (a) Model 1, (b) Model 2, and (c) Model 3.

In the first example, 8 thermistors are added to each unit cell on one side of the Ω absorber. In the second example, 16 thermistors are added to both sides of the Ω absorber, leading to a bi-directional symmetric structure. When the temperature is 295.15 K, the resistance of thermistors is much larger compared with the resistance of titanium. So in this case, the thermistors are modelled by an open circuit. Under such a temperature, the two examples have the same equivalent models (referred to as Model 1 below) as shown in Fig. 5 (a). As the temperature rises, the resistance of the thermistors decrease and hence can be modelled by a section of aluminum as plotted in green in Figs. 5 (b) (Model 2) and (c) (Model 3), respectively.

B. Design of metasurface absorbers

From equation (6) in section II, we know that to obtain total absorption, two conditions should be satisfied. First, the normalized electric and the normalized magnetic polarizabilities of the metasurface must be equal. Second, they should be purely imaginary.

In order to validate the proposed temperature-controlled absorber designs, full-wave simulations were conducted by ANSYS High Frequency Structure Simulator (HFSS) software to evaluate the normalized polarizabilities of the proposed absorbers.

The unit cell is surrounded by periodic boundary conditions in the xOy plane, and two ports are defined in the z-direction to calculate S parameters (Fig. 6). The Ω rings can be embedded in a plastic foam substrate such as polymethacrylimide (PMI) for mechanical support [27]. This PMI material is with $\varepsilon = 1.05 - 1.13$, loss tangent
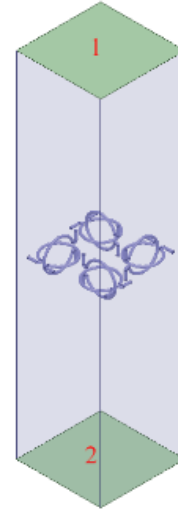

Fig. 6. Schematic of the simulation settings.

of $\delta = (1 - 18) \times 10^{-3}$, and thermal deformation temperature of 449-509 K.

Following the method in [18], the normalized polarizabilities $\widetilde{\alpha}_{ee}$, $\widetilde{\alpha}_{em}$, $\widetilde{\alpha}_{me}$ and $\widetilde{\alpha}_{mm}$ of Model 1 are obtained. Figure 7 shows that the entries on the diagonal of $\widetilde{\alpha}_{ee}$ are of the order of 10^{-22}. The remaining entries are of the order of 10^{-26}. Moreover, the curves of $\widetilde{\alpha}_{ee}^{xx}$ and $\widetilde{\alpha}_{ee}^{yy}$ coincide. Similar results for $\widetilde{\alpha}_{mm}$ can be obtained and are not plotted here. Considering the ω in equations (2) and (3) is in the order of 10^{12}, the cross-section S is in the order of 10^{-10}, the simulation results indicate that the reflected waves can be affected significantly by the diagonal elements of $\widetilde{\alpha}_{ee}$ and $\widetilde{\alpha}_{mm}$.

Figures 7 (c) and (d) show that all the entries of $\widetilde{\alpha}_{em}$ are of the order of 10^{-26}. Similar results for $\widetilde{\alpha}_{me}$ can be obtained in the same way and are not plotted here. Therefore, we can approximate the polarizability matrix as:

$$
\begin{bmatrix} \widetilde{\alpha}_{ee} & \widetilde{\alpha}_{em} \\ \widetilde{\alpha}_{me} & \widetilde{\alpha}_{mm} \end{bmatrix} \simeq \begin{bmatrix} \widetilde{\alpha}_{ee} & 0 \\ 0 & \widetilde{\alpha}_{mm} \end{bmatrix}
$$

$$
= \begin{bmatrix} \begin{bmatrix} \widetilde{\alpha}_{ee}^{xx} & 0 \\ 0 & \widetilde{\alpha}_{ee}^{yy} \end{bmatrix} & 0 \\ 0 & \begin{bmatrix} \widetilde{\alpha}_{ee}^{xx} & 0 \\ 0 & \widetilde{\alpha}_{ee}^{yy} \end{bmatrix} \end{bmatrix}, \quad (8)
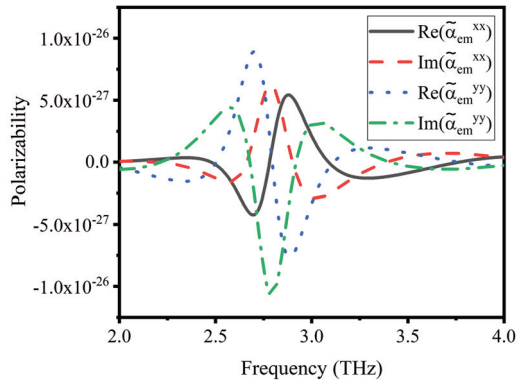$$

$\widetilde{\alpha}_{ee}^{xx}$ and $\widetilde{\alpha}_{mm}^{xx}$ are compared in Fig. 8 (a). It can be seen that $\widetilde{\alpha}_{ee}^{xx}$ and $\widetilde{\alpha}_{mm}^{xx}$ is close around 2.8 THz, and are almost purely imaginary. The reflection, transmission, and absorption coefficients for the metasurface in
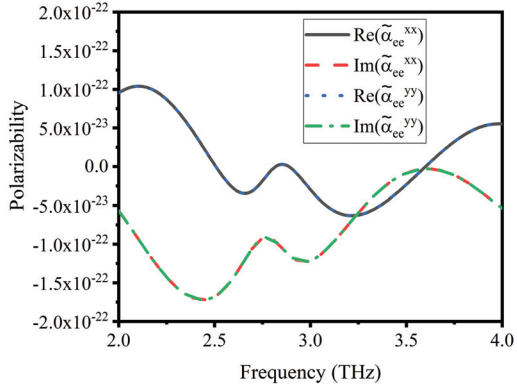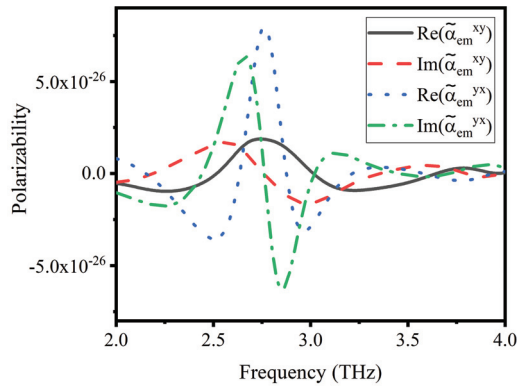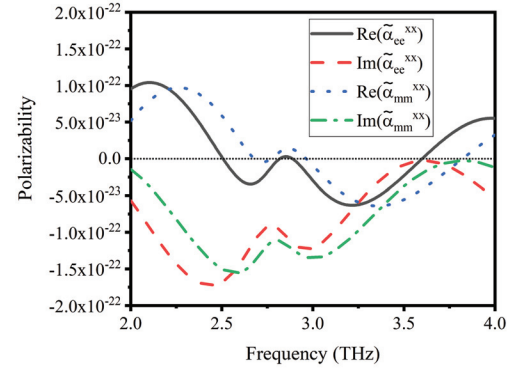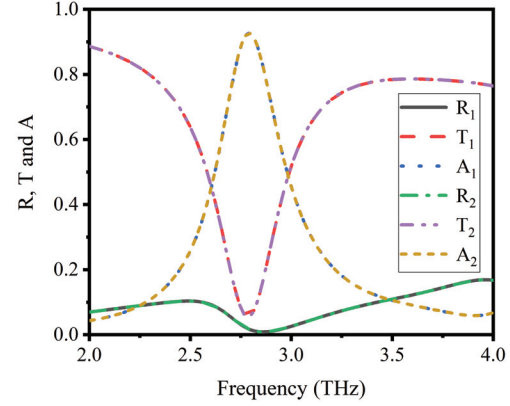
(a)
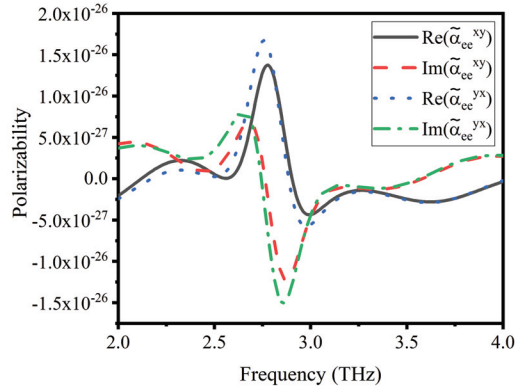
(b)

(c)

(d)

Fig. 7. The normalized polarizability results of Model 1.

(a)

(b)

Fig. 8. The normalized polarizabilities and absorption coefficients of Model 1.

Model 1 are plotted in Fig. 8 (b). The subscript 1 or 2 corresponds to the excitation port number as defined in Fig. 6, so it indicates the direction of the incident wave. Maximum absorption coefficient of 92.7% can be seen at 2.79 THz, which agrees with the polarizability results shown in Fig. 8 (a). Since the structure bears both mirror symmetry in the z-direction and rotational symmetry in the xOy plane, the absorber functions identically for incidences from +z and -z directions, and is polarization insensitive.

The normalized polarizabilities $\widetilde{\alpha}_{ee}$, $\widetilde{\alpha}_{em}$, $\widetilde{\alpha}_{me}$ and $\widetilde{\alpha}_{mm}$ of Model 2 can also be obtained. Similarly to Model 1, the normalized polarizabilities of Model 2 can also be approximated by equation (8).

Comparing $\widetilde{\alpha}_{ee}^{xx}$ and $\widetilde{\alpha}_{mm}^{xx}$ plotted in Fig. 9 (a), we can see around 3.5 THz $\widetilde{\alpha}_{ee}^{xx}$ and $\widetilde{\alpha}_{mm}^{xx}$ are close and are almost purely imaginary. Correspondingly, peak absorptions occur around this frequency (Fig. 9 (b)). This metasurface is still polarization insensitive. However, since the structure loses the mirror symmetry in the z-direction, a slight difference in A_1 and A_2 can be observed, indicating the metasurface functions differently for the upward and the downward incidences.
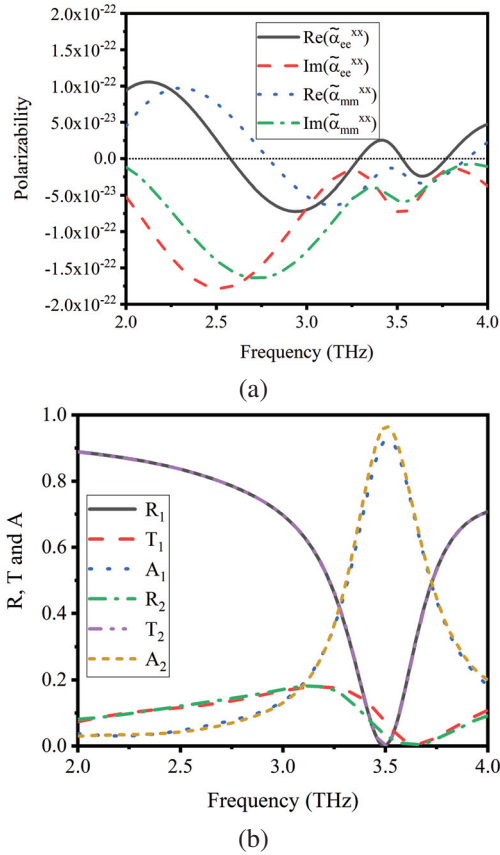
(a)

(b)

Fig. 9. The normalized polarizabilities and absorption coefficients of Model 2.

(a)

(b)

Fig. 10. The normalized polarizabilities and absorption coefficients of Model 3.

Specifically, the absorption coefficient changes from 92.5% (at 3.52 THz) to 96.7% (at 3.51 THz) when the incident direction changes from -z to +z.

Similar conclusions can be drawn with Model 3. The normalized polarizabilities $\widetilde{\alpha}_{ee}$, $\widetilde{\alpha}_{em}$, $\widetilde{\alpha}_{me}$ and $\widetilde{\alpha}_{mm}$ of Model 3 are similar with Model 1, in which polarizabilities can be approximated by equation (8).

$\widetilde{\alpha}_{ee}^{xx}$ and $\widetilde{\alpha}_{mm}^{xx}$ is close around 4.0 THz, and are almost purely imaginary (Fig. 10 (a)). Accordingly, peak absorption of 93.8% can be found at 3.94 THz (Fig. 10 (b)). Due to its structural symmetry, the absorber in this model is polarization insensitive and bi-directional.

To sum up, the above investigation validates the thermal controlling of the absorbing frequencies, with the overall absorption coefficients of over 90%.

C. Effective circuit analysis

The operation of the proposed temperature controlled absorbers can be understood by equivalent circuit models. In this section, we used the commercial software of Advanced Design System (ADS) to perform the circuit analysis. Through the structure analysis, we can determine the equivalent circuit, as shown in Fig. 11,
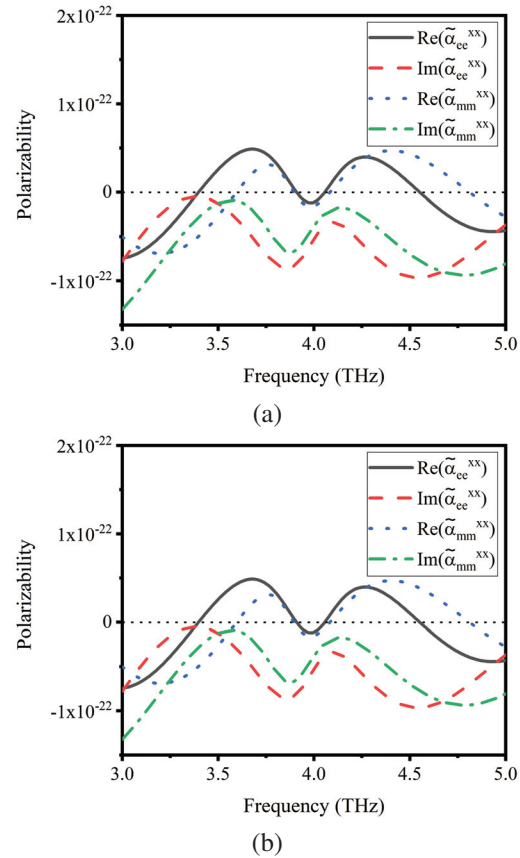

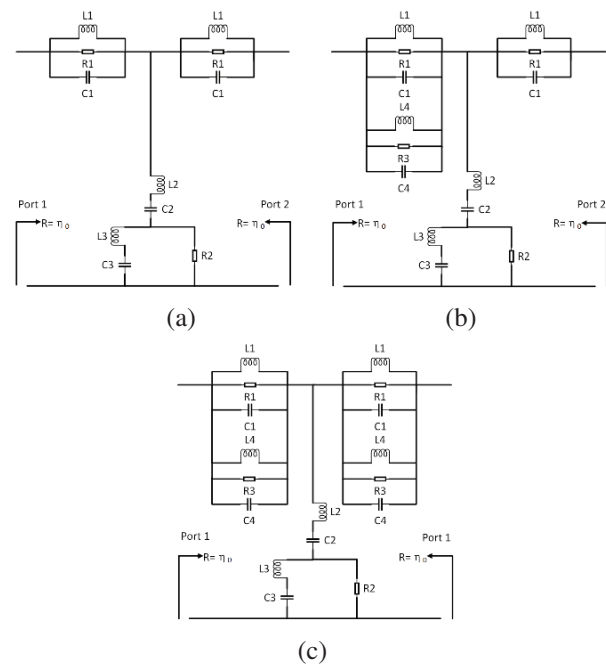(a)   (b)

(c)

Fig. 11. Schematic of effective circuits, (a) Model 1, (b) Model 2, and (c) Model 3.

whose parameters can be further approximated through optimization.

The equivalent circuit models for Models 1 to 3 are plotted in Fig. 11. Due to the z-directional symmetry in the physical structures, models in Figs. 11 (a) and (c) demonstrate corresponding port symmetry. η_0 stands for the wave impedance in free space. The parameters are summarized in Table 2.

Table 2: Parameters of the equivalent circuit models

Model	a	b	c
L1 (pH)	1.05	1.05	1.05
L2(pH)	0.002	0.002	0.002
L3(pH)	1.93	1.93	1.93
L4(pH)	-	0.42	0.42
C1 (pF)	0.003	0.003	0.003
C2 (pF)	0.0003	0.0003	0.0003
C3 (pF)	8.42	8.42	8.42
C4 (pF)	-	0.002	0.002
R1(Ω)	377	377	377
R2(Ω)	17	17	17
R3(Ω)	1288.7	1288.7	1288.7

The simulation results of HFSS and ADS for the three models are compared in Fig. 12. As in Figs. 8–10, the subscript indicates the port of excitation. It can be seen that the ADS and HFSS simulation results agree well at the absorption frequencies for all the models, which validates the effective circuit models. We can also see that the HFSS models have broader absorption frequency bands than the ADS models. The reason is that the circuit models have fewer degrees of freedom, leading to stronger sensitivity to frequency. If a more complex circuit model design could be adopted,
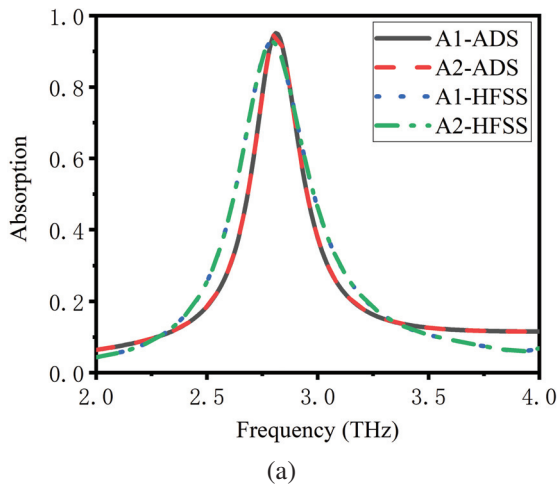
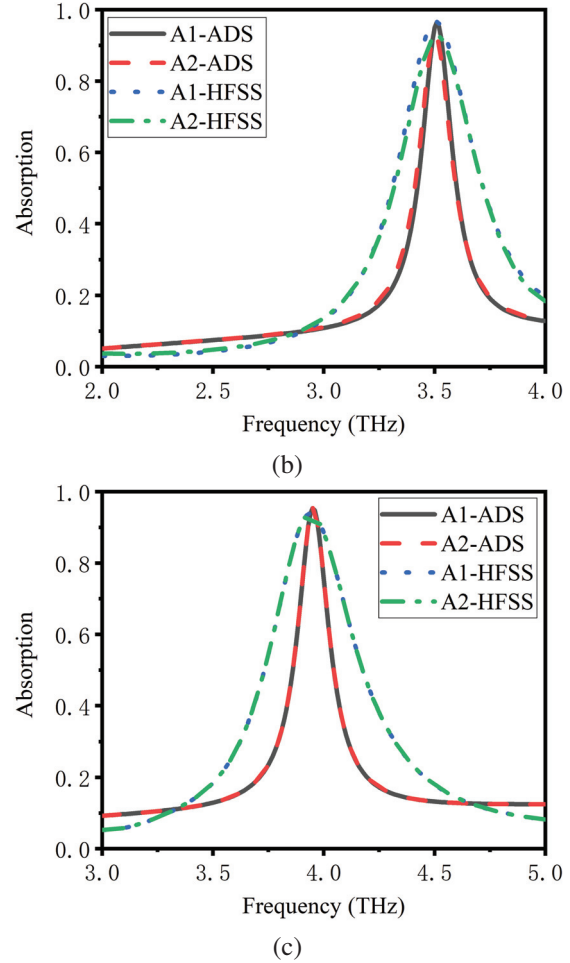

(a)

Fig. 12. *Continued*

(b)

(c)

Fig. 12. Simulated absorption coefficients, (a) Model 1, (b) Model 2, and (c) Model 3.

the results, it would be suggested, would be more consistent.

V. CONCLUSION

In this study, we analyzed the stability of an Ω-shaped absorber and designed two temperature-controlled EM absorbers based on electromagnetism-thermodynamics-structural mechanics multiphysics simulation. Up to the temperature of 1761.4 K, which is close to the melting temperature of the material, the expansion of the Ω-shaped inclusion is within the order of 0.1 μm with expansion rate of no greater than 2.58%. The absorption coefficient maintained at 92.7% at 2.79 THz. This demonstrated the thermal stability of the Ω absorber both in structure and in EM wave absorption function. By adding thermistors, two temperature-controlled absorbers were designed. When the temperature rises, the simulated absorption of the two proposed absorbers demonstrated a frequency shift from 2.79 THz to 3.51 (+0.01) THz and 3.94 THz, with corresponding absorption coefficients of 92.5 (+4.2)%

and 93.8%, respectively. At the end of the paper, the effective circuit model method is used to analyze the two metasurface absorbers. In the THz frequency regime, the proposed thermal-controlled absorbers have substantial potential for being used for spatial light modulators, sensors, and bolometers.

REFERENCES

[1] Y. P. Hong, I. J. Hwang, D. J. Yun, D. J. Lee, and I. H. Lee, "Design of single-layer metasurface filter by conformational space annealing algorithm for 5G mm-wave communications," *IEEE Access*, vol. 9, pp. 29764-29774, Feb. 2021.

[2] W. L. Guo, G. M. Wang, H. P. Li, K. Zhang, and T. Cai, "Ultra-thin two-dimensional transmissive anisotropic metasurfaces for polarization filter and beam steering application," *Chinese Physics B*, vol. 25, no. 10, pp. 104101-104107, Oct. 2016.

[3] Z. Zhang, Y. Zhang, T. Wu, S. Chen, W. Li, and J. Guan, "Broadband RCS reduction by a quaternionic metasurface," *Materials*, vol. 14, no. 11, pp. 2787-2797, May 2021.

[4] Y. Saifullah, F. Zhang, G. Yang, and F. Xu, "3-bit polarization insensitive reflective metasurface for RCS reduction," *The 12th International Symposium Antennas, Propagation, and EM Theory (ISAPE 2018),* Hang Zhou, China, pp. 1-3, Dec. 2018.

[5] C. Huang, W. Pan, X. Ma, and X. Luo, "Wideband radar cross-section reduction of a stacked patch array antenna using metasurface," *IEEE Antennas and Wireless Propagation Letters*, vol. 14, pp. 1369-1372, Dec. 2015.

[6] T. A. Khan, J. Li, U. Raza, J. Chen, and A. Zhang, "Design of a metasurface with wide RCS reduction bandwidth," *2019 Photonics & Electromagnetics Research Symposium - Fall (PIERS - Fall),* Xiamen, China, pp. 976-982, Dec. 2019.

[7] T. Almoneef and O. M. Ramahi, "Dual-polarized multi-band infrared energy harvesting using h-shaped metasurface absorber," *Progress in Electromagnetics Research C*, vol. 76, pp. 1-10, Jan. 2017.

[8] N. Muhammad, T. Fu, Q. Liu, X. Tang, Z. L. Deng, and Z. Ouyang, "Plasmonic metasurface absorber based on electro-optic substrate for energy harvesting," *Materials*, vol. 11, pp. 2315-2325, Nov. 2018.

[9] M. Bağmancı, M. Karaaslan, E. Ünal, O. Akgol, F. Karadağ, and C. Sabah, "Broad-band polarization-independent metamaterial absorber for solar energy harvesting applications," *Physica E: Low-dimensional Systems and Nanostructures,* pp. 1-6, June 2021.

[10] A. Kumar, C. Saha, and R. Sethunadh, "Dual band energy harvester based on metasurface absorber," *2020 URSI Regional Conference on Radio Science (URSI-RCRS),* Varanasi, India, pp. 1-4, Feb. 2020.

[11] K. Zhang, Y. Wang, S. N. Burokur, and Q. Wu, "Generating dual-polarized vortex beam by detour phase: From phase gradient metasurfaces to meta-gratings," *IEEE Transactions on Microwave Theory and Techniques*, vol. 70, no. 1, pp. 200-209, Jan. 2022.

[12] Y. Yuan, S. Sun, Y. Chen, K. Zhang, and C. Qiu, "A fully phase-modulated metasurface as an energy-controllable circular polarization router," *Advanced Science*, vol. 7, no. 18, pp. 2001437, July 2020.

[13] X. Zhang, H. Liu, Z. Zhang, Q. Wang, and S. Zhu, "Controlling thermal emission of phonon by magnetic metasurfaces," *Scientific Reports*, vol. 7, no. 1, pp. 1-8, Feb. 2017.

[14] J. Li, B. Yu, and S. Shen, "Scale law of far-field thermal radiation from plasmonic metasurfaces," *Physical Review Letters*, vol. 124, no. 13, pp. 137401, Mar. 2020.

[15] Y. Ueba and J. Takahara, "Spectral control of thermal radiation by metasurface with split-ring resonator," *Applied Physics Express*, vol. 5, no. 12, pp. 122001, Dec. 2012.

[16] T. Niemi, A. O. Karilainen, and S. A. Tretyakov, "Synthesis of polarization transformers," *IEEE Transactions on Antennas and Propagation*, vol. 61, no. 6, pp. 3102-3111, June 2013.

[17] X. X. Liu, Y. Zhao, and A. Alù, "Polarizability tensor retrieval for subwavelength particles of arbitrary shape," *IEEE Transactions on Antennas and Propagation*, vol. 64, no. 6, pp. 2301-2310, June 2016.

[18] M. Yazdi and N. Komjani, "Polarizability calculation of arbitrary individual scatterers, scatterers in arrays, and substrated scatterers," *JOSA B*, vol. 33, no. 3, pp. 491-500, 2016.

[19] L. Pulido-Mancera, P. T. Bowen, M. F. Imani, N. Kundtz, and D. Smith, "Polarizability extraction of complementary metamaterial elements in waveguides for aperture modeling," *Physical Review B*, vol. 96, no. 23, pp. 235402-235404, Mar. 2017.

[20] V. S. Asadchy, I. A. Faniayeu, Y. Ra'Di, S. Khakhomov, I. Semchenko, and S. Tretyakov, "Broadband reflectionless metasheets: frequency-selective transmission and perfect absorption," *Physical Review X*, vol. 5, no. 3, pp. 031005-031007, July 2015.

[21] A. Balmakou, M. Podalov, S. Khakhomov, D. Stavenga, and I. Semchenko, "Ground-plane-less bidirectional terahertz absorber based on omega resonators," *Optics Letters*, vol. 40, no. 9, pp. 2084-2087, Sep. 2015.

[22] C. M. Watts, D. Shrekenhamer, J. Montoya, G. Lipworth, J. Hunt, and T. Sleasman, "Terahertz compressive imaging with metamaterial spatial light modulators," *Nature Photonics*, vol. 8, no. 8, pp. 605-609, Aug. 2014.

[23] M. Gustafsson, I. Vakili, S. E. B. Keskin, D. Sjoberg, and C. Larsson, "Optical theorem and forward scattering sum rule for periodic structures," *IEEE Transactions on Antennas and Propagation*, vol. 60, no. 8, pp. 3818-3826, Aug. 2012.

[24] K. N. Rozanov, "Ultimate thickness to bandwidth ratio of radar absorbers," *IEEE Transactions on Antennas and Propagation*, vol. 48, no. 8, pp. 1230-1234, Aug. 2000.

[25] H. Liu, J. Lu, and X. R. Wang, "Metamaterials based on the phase transition of VO2," *Nanotechnology*, vol. 29, no. 2, pp. 024002-024003, Jan. 2017.

[26] A. M. Shaltout, V. M. Shalaev, and M. L. Brongersma, "Spatiotemporal light control with active metasurfaces," *Science*, vol. 364, pp. 648-657, May 2019.

[27] F. Zhao, "Present state of art of polymethacrylimide (PMI) foam research," *Aerospace Materials and Technology*, pp. 1-6, Jan. 2008.

[28] J. Li and J. Dho, "Characteristics of phase transition of VO2 films grown on TiO2 substrates with different crystal orientations," *Journal of Crystal Growth*, vol. 404, pp. 84-88, July 2014.

Jia-Tong Jing received his B.E. and M.S. degrees from the Beijing Institute of Technology, Beijing, China, in 2018 and 2021 respectively. He is currently pursuing a Ph.D. degree at the Institute of Radio Frequency Technology and Software from Beijing Institute of Technology. His current research interests include metamaterial and computational electromagnetics.

Wei Song received her B.S. degree from North Eastern University, Shen-yang, China, in 2002, and her M.S. and Ph.D. degrees from Queen Mary University of London, London, UK, in 2003 and 2008, respectively. She is currently an Associate Professor with the School of Information and Electronics, Beijing Institute of Technology, Beijing, China. She has authored or co-authored over 20 papers in refereed journals and international conferences, and has co-authored a monograph in computational electromagnetics. Her current research interests include high-performance methods in computational electromagnetics, EM property analysis, and metamaterial-based antenna design.

Ting-Ting Ge received her B.E. degree from North China University of Technology, Beijing, China, in 2019, and her M.S. degree from the Beijing Institute of Technology, Beijing, China, in 2022. Her current research interests include EM property analysis, and metamaterial-based antenna design.

Xin-Qing Sheng received his B.S., M.S. and Ph.D. degrees from the University of Science and Technology of China (USTC), Hefei, China, in 1991, 1994, and 1996, respectively. Sheng is a Chang-Jiang Professor of the School of Information and Electronics at the Beijing Institute of Technology. Sheng has authored and co-authored over 150 papers in refereed journals, and three books: *Essentials of Computational Electromagnetics* (Singapore: IEEE Press-Wiley, 2012), *A Brief Treatise on Computational Electromagnetics* (Beijing: Science Press, 2004), and *A Treatise on Electromagnetic Waves* (Beijing: Science Press, 2007). Sheng authored SINOCOM, a simulation software for scattering by complex targets. His research interests include computational electromagnetics, scattering and antenna analysis, electromagnetic compatibility, and microwave imaging.

Electromagnetic and Thermal Analysis of a 6/4 Induction Switched Reluctance Machine for Electric Vehicle Application

Ali Madanimohammadi, Mohammadali Abbasian, Majid Delshad, and Hadi Saghafi

Department of Engineering
Islamic Azad University, Isfahan (Khorasgan) Branch, Isfahan 39998-81551, Iran
a.madani.m@khuisf.ac.ir, m.abbasian@khuisf.ac.ir, delshad@khuisf.ac.ir, h.saghafi@khuisf.ac.ir

Abstract – In this paper, an oil-cooling induction switched reluctance machine (ISRM) is offered. The stator and rotor of the electric machine are non-segmental. However, by placing coils on the rotor, a short magnetic flux path is achieved in the rotor and stator cores. As a result, a higher torque with lower losses is generated. This configuration can be used in high-power electric motors for electric and hybrid vehicles. ISRM is a novel machine and there is a lack of access to its operation and data characteristics. ISRM can be designed in different configurations with various stator and rotor pole numbers and winding strategies. In this study, an oil-cooling three-phase ISRM with 6 stator poles and 4 rotor poles was considered. Firstly, a 2D finite element model of it is created, and its magnetic properties extracted, the flux path, torque and efficiency of the ISRM are calculated, and the results are presented. Secondly, the thermal performance of the motor is analyzed using ANSYS Motor-Cad software. Finally, a prototype of the ISRM and its appropriate drive with the oil cooling system is built and tested. The experimental results and conclusions which prove the ability of the presented machine are presented in the last parts of the paper.

Index Terms – analysis, electric vehicle, finite element, induction motor, oil spray cooling, short flux path, switched reluctance motor.

I. INTRODUCTION

In recent decades, the number of vehicles that consume fossil fuels has been increasing all over the world. This leads to the generation of toxic gases and materials, which is a serious threat to human health and the environment. Replacing internal combustion engines with electric powertrains is an appropriate solution to reduce the dangerous pollutants produced by traditional vehicles. Electric machines are the most essential part of electric powertrains. For electric vehicle applications, high-performance electric machines are required. They should be lightweight, compact, low-cost, efficient, easily to manufacture, and above all, reliable [1].

Permanent magnet machines, such as Permanent Magnet Synchronous Machines (PMSM) are implemented in hybrid and electric vehicles due to their high torque and efficiency [2]. These machines use permanent magnets that contain rare earth materials such as Neodymium and Samarium. On the other hand, the high cost of permanent magnet materials and their limited supply have been identified as significant challenges for the electric vehicle industry in the future [3].

There are other electric motors that could be considered to be used as a propulsion system for electric vehicles. The most famous one is the induction machine, which has been implemented in the powertrain of Tesla cars' previous models. Induction machines do not contain permanent magnets but still have an acceptable power density and efficiency. However, they don't have the efficiency and power density as high as the permanent magnet motors [4]. As a result, the new models of Tesla cars replaced PMSM with an induction motor as a traction motor.

Some researchers have been working on switched reluctance machines (SRMs) instead of induction machines or permanent magnet machines in the powertrain of electric vehicles. SRMs consist of a straightforward structure and have fault-resistant performance under difficult operational circumstances [5]. The simplicity of an SRM is due to its rotor configuration, which does not contain either permanent magnets or conductors. In SRMs, only reluctance torque is the cause of torque generation. Simple structure, low cost, high-temperature resistant rotor, and high speed are the most essential advantages of the switched reluctance motors. Compared to a permanent magnet motor, switched reluctance motors contain some disadvantages, such as a lower level of torque density, a high level of torque ripple, noise, and vibration [6].

In recent years, many investigations have been done to improve the switched reluctance motor capabilities and advantages. The research shows this critical fact

that only a small percentage of the electromechanical forces generated inside the SRMs are used to produce motion and produce torque. In fact, not only a large part of the force produced is a non-motional force, but it is also caused by motor noise and vibration. This is one of the primary defects of the SRMs that needs to be addressed. Many efforts have been made to design SRMs with a higher percentage of a motional force to achieve high torque motors with lower noise and vibration. For example, the double stator switched reluctance machine (DSSRM) was designed in 2010 with high torque density and low vibration [7]. DSSRM consists of a cylindrical hollow rotor and two stators. In this structure, short flux paths are created in the machine cores. It has been demonstrated that the implementation of this structure, can create more motional force, the torque density of a DSSRM is twice that when compared with the conventional SRM. In DSSRM topology, the non-motional force is declined, so the machine experiences lower noise and vibration. On the other hand, DSSRM has some drawbacks, and researchers are working to address them. For example, in electric vehicle applications, the inner stator, which contains high-current windings, is surrounded by the rotor. As a result, it isn't easy to design a cooling system for the inner stator. Moreover, the rotor is composed of several ferromagnetic segments which are embedded in a non-ferromagnetic cylinder. This may hinder a straightforward realization of the rotor and other parts of the motor and urges us to design electric motors with a non-segmental rotor and stator.

There are other high torque and short flux path SRMs that have a segmental rotor or stator [8-10]. For instance, a segmented switched reluctance motor was introduced by Mecrow, with a segmental rotor and non-segmental stator [8]. In this electric machine, the rotor consists of ferromagnetic segments, which are fixed together by a non-ferromagnetic cage. This configuration is such that it prevents the flux from circuiting through all the stator yoke. This electric motor can produce 40% more torque than conventional SRMs of the same size. Another configuration of segmental switched reluctance motor has been proposed in [9]. In this structure, the rotor is segmental, and the stator is non-segmental. Like other segmental SRMs, this motor can produce higher torque compared to the conventional SRMs while generating a lower core loss. It should be mentioned that in segmental SRMs a minor deviation in the manufacturing and assembly process of segmented parts, can result in a non-uniform airgap between the rotor and stator. This can lead to mechanical problems during motor operation, such as a vibration increase in the motor [7].

If a switched reluctance machine can be designed with a non-segmental rotor and stator, and at the same time a short flux path is maintained in the motor core,

appropriate results can be obtained. To this end, [11] has proposed a novel structure of an electric machine called ISRM. This machine can use the impact of magnetic induction and a short flux path to enhance the energy conversion efficiency of the generated force into motion and torque. This structure leads to a fundamental change in the design of electric motors and their optimization. In this motor, the integrated structure and the rotor conductors lead to a very short flux path. In the next section, more details about the operation principles of ISRM will be presented and a comprehensive analysis will be performed, using the finite element method.

ISRM can be designed with multiple poles and different coils. To investigate this novel structure, this paper examines a 6kw ISRM with 6 stator poles and 4 rotor poles. It is designed and analyzed using ANSYS Maxwell software. The results of the magnetic analysis are presented along with calculations of flux, torque, and efficiency. Also, the thermal performance of this motor, which uses an oil cooling system, is done using ANSYS Motor-Cad software. The 6kw ISRM is built and tested, and in the end the experimental results are presented.

II. ISRM
A. Machine topology

ISRM is a novel electrical machine but it has a conventional structure. It includes one inner rotor and one outer stator [11]. This is an advantage for this machine, because some of the novel electric machines which are presented for electric vehicle propulsion systems have an unconventional structure that makes the machine manufacturing process more difficult. The rotor of ISRM contains short-circuited coils. The rotor coils are not powered by an external source, but the current is induced while the rotor moves. During the rotor rotation, the magneto motive force (MMF) generated by the rotor coils prevents the flux from passing through the rotor yoke, leading to the creation of a short flux path.

ISRM can be designed in different types of poles and various winding strategies. Depending on the number of stator and rotor poles, the winding pitches can differ. In some configurations, the stator and rotor coils are full pitch, while in some other topologies, the stator and or rotor coils are short pitch. For instance, a 12/8 ISRM with short-pitch rotor coils and full-pitch stator coils are presented in [11].

The number of ISRM stator and rotor poles is selected as conventional SRMs. In this paper, ISRM with 6 stator poles and 4 rotor poles is investigated. Figure 1 shows a schematic of this three-phase ISRM. As illustrated in the figure, the stator and rotor coils are full pitch. Figure 2 shows the connection of windings. In ISRM, the rotor coils are not connected, contrary to the induction machine. Like conventional SRMs, the DC pulse is
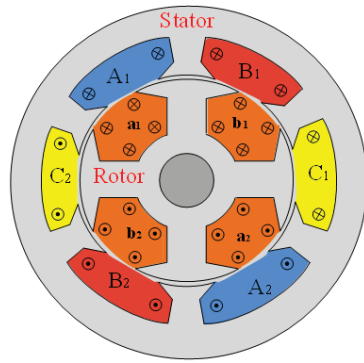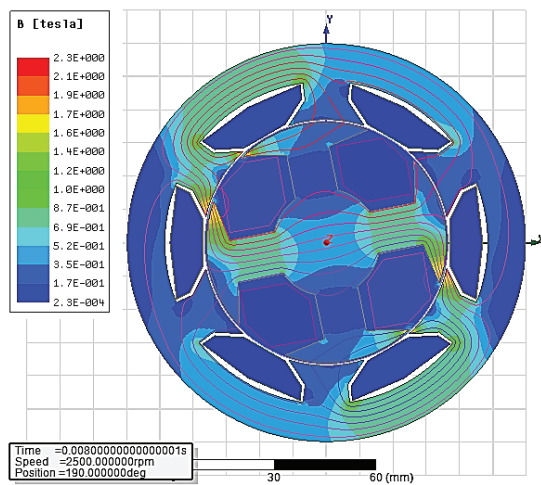
Fig. 1. A 3-phase 6/4 ISRM.

Fig. 2. Flux path in ISRM without rotor winding.

required to excite each phase of ISRM. These pulses are generated by the electric drive, respecting the rotor position. Conventional SRM drives can be implemented into ISRM without any modifications.

If a phase of the ISRM is excited while the rotor is rotating, the magnetic field inside the rotor coils will change. This results in voltage induction in the short-circuited coils of the rotor, according to Faraday induction law. Based on Lenz's law, the direction of the inductive electromotive forces in the rotor coils is opposed to the flux changes. Hence, the flux does not pass through the rotor core, which leads to a short flux path around the excited stator coil. The results of the finite element analysis to determine the flux path of ISRM will be presented in this paper.

B. Simulation of ISRM (6/4)

The two-dimensional model of a 6/4 ISRM with the characteristics shown in Table 1 is simulated using ANSYS Maxwell software.

This configuration has some advantages, such as high-speed capability and low switching loss, compared

Table 1: Specifications of the ISRM and SRM

Parameter	Value
Housing diameter	120 mm
Stator outer diameter	100 mm
Motor length	115 mm
Stack length	50 mm
Air gap	0.5 mm
Number of stator poles	6
Number of rotor poles	4
Turn number of stator coils	100
Turn number of rotor coils (ISRM)	100
Rated current	80 A
Maximum current density	20 A/mm^2
Rotor and stator material	M19
Rated power (ISRM)	6 kW
Rated power (SRM)	3 kW
Cooling method	Direct oil cooling

to the ISRMs with a high number of rotor and stator poles. The purpose of this simulation is to investigate the rotor short-circuit coil's effect on the motor magnetic flux distribution. In the first step, phase A is powered, assuming that no coils are placed on the rotor. After simulating the motor in transient mode with the speed of 2500 rpm, the magnetic flux is calculated, and the results are presented. Figure 2 clearly shows that the magnetic flux paths are distributed in all poles of the rotor and stator. In the second step, the copper coils act as a short circuit on the rotor, and the same simulation is repeated again under the same conditions. The results of the new simulation can be seen in Figs. 3 and 4. As shown in the figures, the flux path is shortened, and the flux does
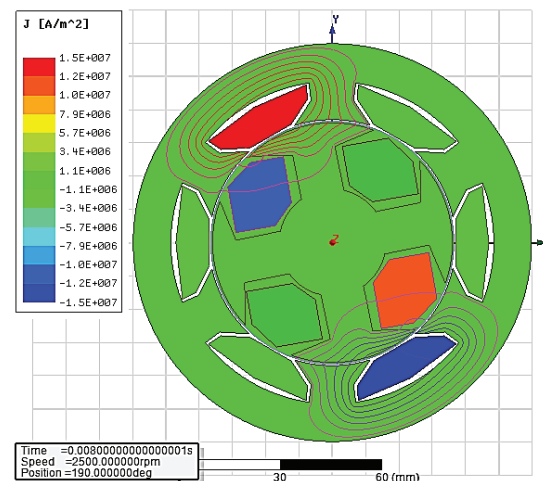

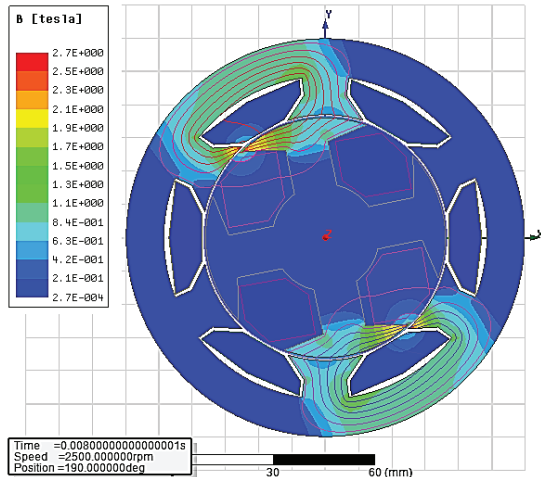Fig. 3. ISRM current distribution while phase A is excited.

Fig. 4. Flux distribution in the ISRM while phase A is excited.

not enter the rotor yoke due to the current induced in the rotor coils.

C. Torque characteristics of ISRM (6/4)

In this section, a conventional SRM and an ISRM are considered and the torques are calculated. Table 1 presents the related characteristics.

According to the transient finite element analysis of ISRM, phase A is excited with a constant current, while the rotor speed is constant. It should be noted that if the direct oil cooling method is applied to the rotor and stator windings, the current density of the conductors can increase up to 20 A/mm^2. In this case, the maximum phase current of the ISRM and the SRM will be 80 A. Considering this maximum current, the finite element method (FEM) analysis is performed in this study.

The reposition of the rotor is 45 degrees from unalignment to alignment. It should be noted that only two thirds of the considered torque range is used in the continuous operation mode (30 degrees). The FEM calculated results of the generated torque and the average torque of the ISRM (while the phase current is 80 A and the rotor speed is 2500 rpm) are presented in Figs. 5 and 6, respectively.

The same simulation (while the phase current is 80 A and the rotor speed is 2500 rpm) is performed for a conventional SRM, with the specifications presented in Table 1, and the simulation results are extracted. Figure 7 shows the flux distribution for the conventional SRM. The generated torque and the output torque of the SRM is calculated and presented in Fig. 5. The results demonstrate that ISRM can produce torque 85% higher than the equal-sized SRM. It should be mentioned that the ISRM torque has a high torque ripple. This is also the case for the conventional SRM. The torque ripple of ISRMs can
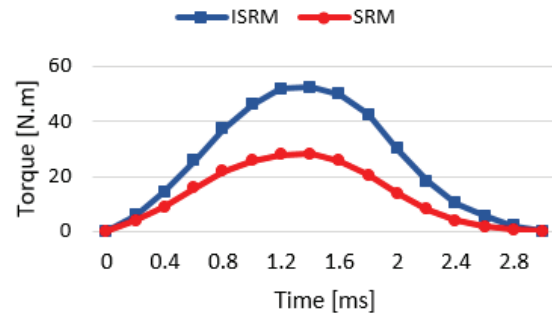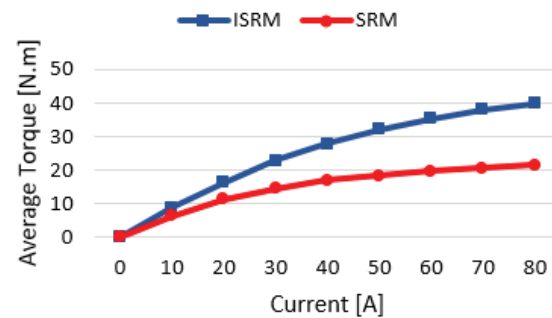

Fig. 5. Total torque of ISRM and SRM.

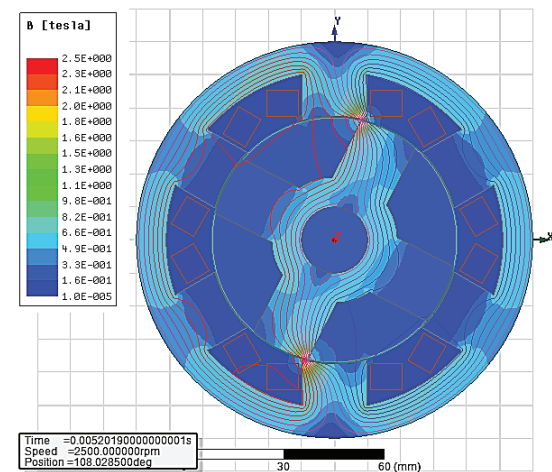Fig. 6. Average torque of the ISRM and the SRM in different currents.

Fig. 7. Flux distribution of the SRM while phase A is excited.

be mitigated by the same techniques that are applied to conventional SRMs [12].

D. Evaluation of ISRM copper loss

While the rotor moves, the current is induced in the rotor coils. In this section, the induced current analysis

in rotor coils is performed using the FEM. The current of the excited stator phase is assumed 80 A, and the rotor speed is 2500 rpm. The induced current of one of the rotor coils is shown in Fig. 8. Actually, current is induced in the rotor coil, which is under the excited stator phase. Firstly, when the rotor is in an unaligned position, the induced current in the rotor coil is equal to the stator phase current. The induced current in the rotor coils is variable, and it vanishes when the rotor is moving from the unaligned position toward the aligned position.
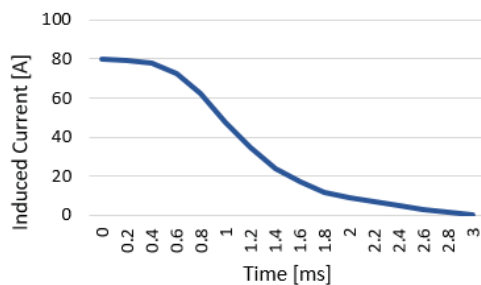
Fig. 8. Induced current in a rotor winding.

It may be assumed that implementing coils on the rotor of ISRM may enhance the overall copper loss of the machine. Actually, the rotor of ISRM generates copper loss due to the windings of the rotor, and this is a drawback compared to conventional SRMs which don't have conductors on the rotor. But if the output torque compared to the overall copper loss of ISRM is high enough, it can be concluded that the efficiency of ISRM is high. In other words, a desired torque of ISRM is created with a lower stator current compared to SRM. This issue can be analyzed using the FEM method.

By FEM analysis and simulation of the ISRM and the SRM (see Table 1) in different currents, the copper loss in different output powers is calculated and presented for each motor in Fig. 9.
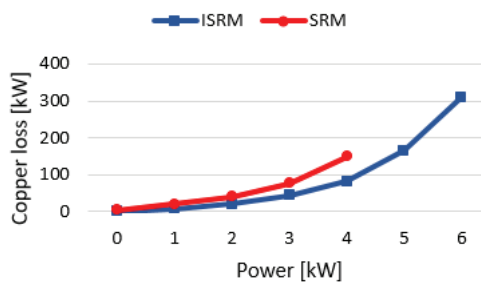

Fig. 9. The copper loss of the ISRM compared to the copper loss of the conventional SRM at various output powers.

The analysis is considered with an oil cooling system, and the winding temperature is 100°C. The motor speed is constant in these simulations (2500 rpm). It can be concluded that the ISRM copper loss is lower than the copper loss of the SRM in each output power. It can be found that the presence of the rotor coil does not increase the total copper loss of the ISRM at a specific output power compared to the SRM.

E. The ISRM cooling system

Thermal stress causes damage to various components of electric machines, such as coils, insulations, bearings, and magnets. The cooling system can be selected depending on the application of the electric machine. To increase the output torque of the machine, the current density of stator conductors has to be increased as much as possible. To this end, the heat generated due to the ohmic loss of high currents should be removed from the machine. High torque density electric machines which are implemented in electric vehicle propulsion systems require modern cooling techniques. Actually, in the conductors of these machines, the current density can reach up to 20 A/mm^2, which urges us to employ direct liquid cooling systems. Direct liquid cooling is accomplished using different techniques such as spray methods.

Oil spray cooling is an effective method that can remove high levels of heat from the inner parts of the motor. This method is implemented in recent models of Tesla and Toyota Prius. The coolant that is employed in oil spray cooling systems of electric machines must have specific properties. They need to be non-flammable, non-toxic, chemically stable, and inert. Moreover, they must have a low dielectric constant, high dielectric strength, and low density. For example, Florien liquids have these criteria and are richly used for direct liquid cooling systems [13].

To analyze the thermal behavior of the electric machine, two numerical methods can be employed. The most accurate method is the finite element method, but it takes time to solve a problem using this technique. Another method is based on the lumped parameter thermal network, which can provide acceptable results quickly. Ansys Motor-CAD is a powerful tool that yields admissible analysis using the lumped parameter thermal network technique.

In this paper, Ansys Motor-Cad is used to predict the thermal behavior of the 6/4 ISRM. Firstly, the ISRM model is built into the software, and the losses of all parts of the machine which are calculated in Ansys Maxwell are imported. Then, oil-spray cooling is chosen as the cooling method of the electric machine. Automatic transmission fluid, ATF134 with a density of 812.5kg/m3, and specific heat of 2.030J/kg· K was chosen as the

coolant. Conditions applied to the thermal network are according to [13]. The rotational speed is 2000 rpm, and the ambient temperature is set at 40°C. Moreover, the coolant inlet temperature is 40°C and the minimum rate of published coolant flow is 1 L/min. In this cooling system, six nozzles with a diameter of 6.35mm are implemented around the motor.

Figure 10 shows the three-hour temperature-increase curve of the ISRM non-cooled motor. The final temperature of the stator winding is 168°C, the rotor winding temperature is about 270°C, and the stator pole temperature is about 164°C. Furthermore, the rotor pole temperature is about 153°C.
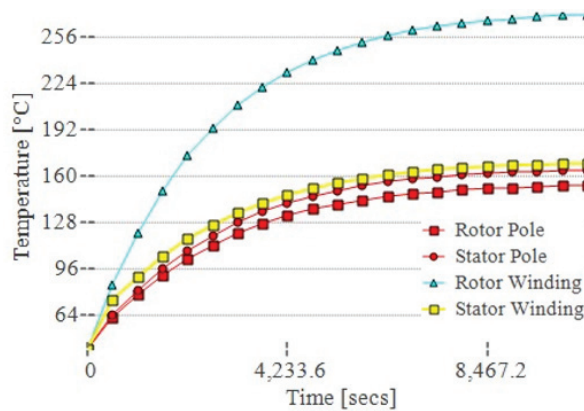
Fig. 10. The three-hour temperature-increasing curve of the non-cooled motor.

Figure 11 shows the three-hour temperature-increase curve of the oil-cooled motor. The initial temperature of the motor winding is 40°C. After one hour, the temperature of the motor parts is stable. The rotor winding temperature is about 130°C and
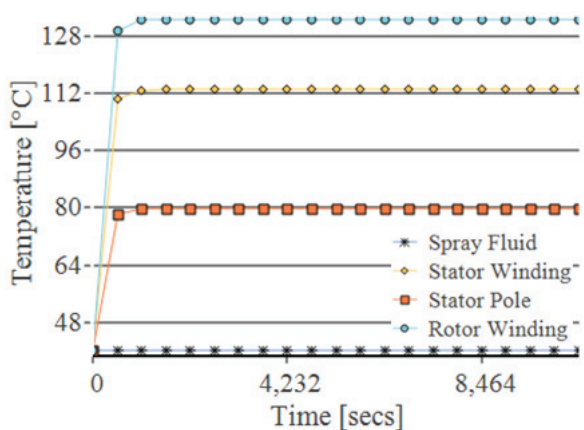

Fig. 11. Comparison of the temperature curve of the ISRM with oil cooling.

the stator winding temperature is about 100°C. Furthermore, the stator pole temperature is about 80°C. Figure 12 shows the thermal stress in different parts of the ISRM.
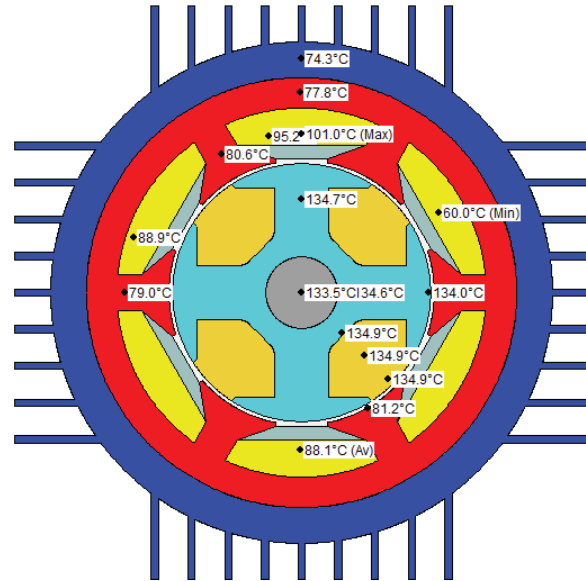

Fig. 12. Thermal stress of the ISRM with oil cooling system.

III. EXPERIMENTAL RESULTS

For the real traction application of electric vehicles, at least a 50kW ISRM should have been designed and developed, but because of fund shortages, we were just able to construct a 6kW ISRM. This oil spray cooling ISRM, with the characteristics presented in Table 1, was built and tested. Figure 13 shows a block diagram of the experimental test setup of the ISRM. Figure 14 illustrates the ISRM experimental setup of the ISRM. The ISRM prototype can be seen in Fig. 15.

The ISRM drive is precisely the same as conventional SRM drives. Firstly, the instantaneous position of the rotor must be determined at each step to turn the appropriate switches on and off. For this purpose, a shaft encoder (E50S) is mounted on the rotor shaft to determine the rotor position with an accuracy of one degree. Due to the utilization of a relative position sensor, a light sensor is installed on the motor shaft that detects the zero-degree position in each cycle. The advantage of this sensor is that the position error in each revolution is zero and provides enough accuracy to start and control the motor speed.

The ISRM drive includes several electronic boards. The LAUNCHXL-F28069M, C2000 Piccolo,
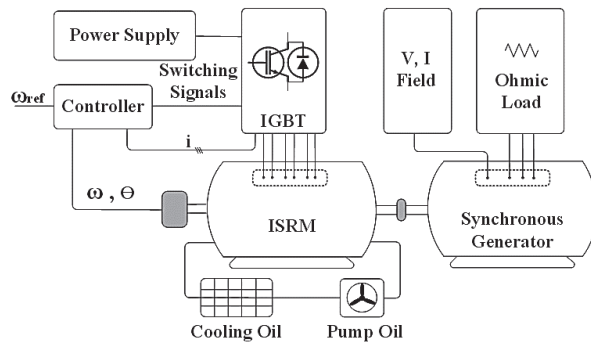
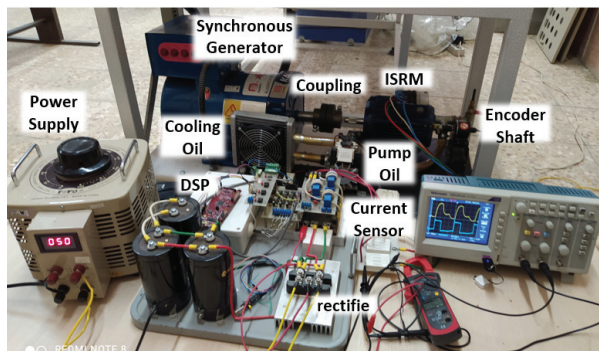Fig. 13. Block diagram of the experimental test setup of the ISRM.

Fig. 14. The experimental setup of the ISRM.

Fig. 15. ISRM prototype.

is employed as a controller to generate sufficient gate pulses to turn IGBTs on and off at the appropriate time. A half-bridge converter using IGBT-IPM was considered as the switching circuit (7MBP75RA120). A snubber circuit is used to limit the voltage overshoots and protect the IGBTs.

In general, experimental measurements can be classified into direct and indirect methods. Direct methods use magnetic sensors to directly measure flux. To measure flux directly, methods are rarely used because the leakage flux affects accuracy. Indirect methods use phase voltage and current to estimate the flux. They can provide a simple structure, a low cost, and better accuracy.

The control of the ISRM is similar to the conventional SRM. The control is based on the changes to the inductance diagram in terms of time. In fact, in motor mode, it should be done only during the time with a positive inductance slope and in generator mode only during the time with a negative inductance slope.

The ISRM control algorithm is shown in Fig. 16. It can be seen that in the figure, five boxes are specified, which respectively represent: encoder, current sensor, rotor position, hysteresis band and switches.

The ISRM prototype was tested for different currents and speeds to evaluate its operation. When the appropriate power switches are turned on, the corresponding stator phase is excited. When a phase is excited, the rotor rotates for 30°C, from the unaligned position toward the aligned position. The switches will be turned off when the rotor is close to aligned position. The energy stored in the excited coils keeps the current in the same direction until this energy has completely vanished. As shown in Fig. 17, following continued excitation, a counterclockwise excitation pattern results in a clockwise rotation of the rotor and vice versa. Figure 17 includes two waveforms. The first figure illustrates the current of one phase of the stator winding and the second figure shows the voltage of the switch at the speed of 700 rpm.

By measuring different voltages and currents, the torque and efficiency of the ISRM can be calculated. The efficiency of the ISRM was calculated at different speeds, and the results are presented in Fig. 18.

The rotor of an ISRM has copper losses due to the rotor windings, and this is a drawback compared to a conventional SRM with no conductors on the rotor. But if the output torque is high enough compared to the total copper losses of the ISRM, it can be concluded that the efficiency of the induction reluctance switch motor is increased. In other words, the desired torque is created in the ISRM motor with less stator current compared to the SRM. The torque is measured for different speeds and can be shown in Fig. 19.
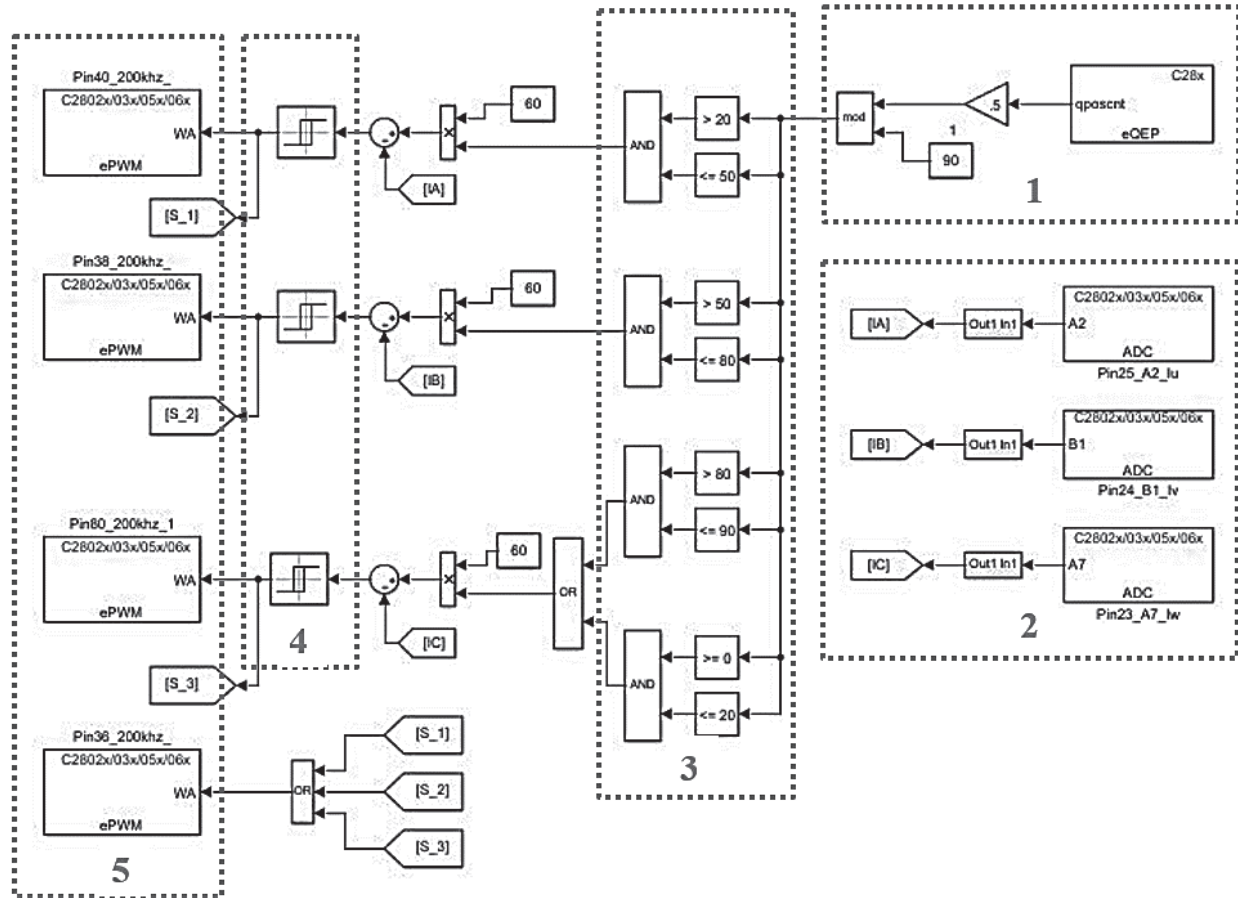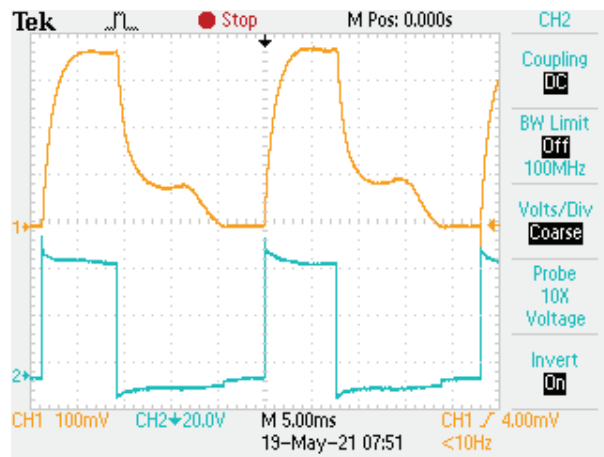
Fig. 16. ISRM 6/4 control algorithm.

Fig. 17. The phase current and voltage of the ISRM.

Fig. 18. The efficiency of the ISRM at various output powers.

The cooling oil is stored in an oil tank with a capacity of approximately 0.4 L/min, is delivered by an oil pump (maximum flow rate: 2 L/min) to the flow path, whi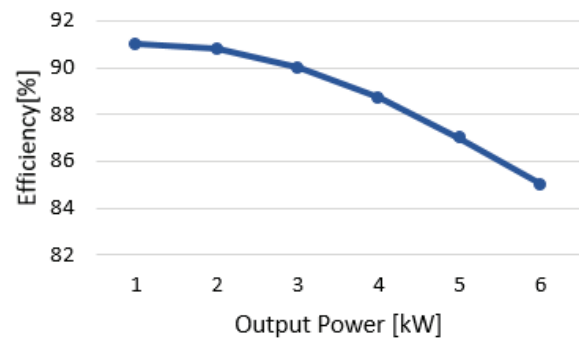ch is located in a hollow area of the shaft. The hollow flow path of the shaft has 6 nozzles to spray the cooling oil over the end windings. The oil absorbs the internal heat of the motor and then flows to the oil tank via a hole under the motor housing. The torque calculated from the FEM analysis and the experimental results are compared in Fig. 20.
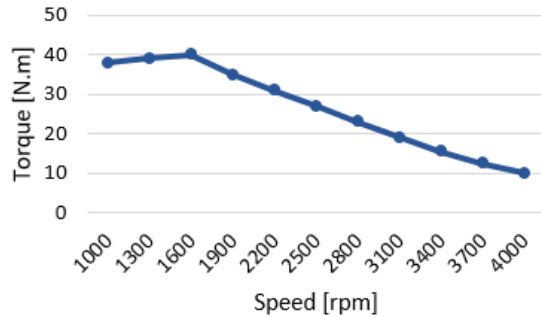
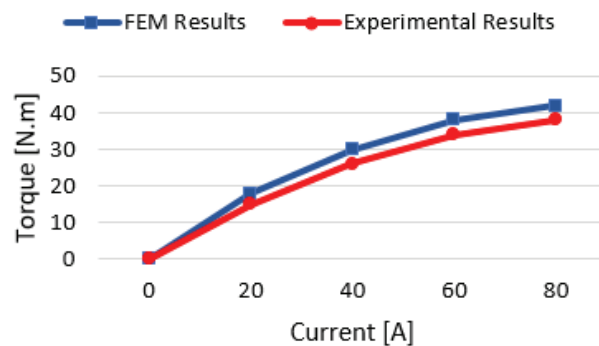Fig. 19. Torque versus speed of the ISRM.

Fig. 20. The FEM and experimental results of the ISRM.

Motor-CAD thermal analysis and the experimental results are compared in Fig. 21. A graph of steady-state temperatures shows the various parts the engine has reached. It can be observed that there is a desired accordance between simulation and experimental results.
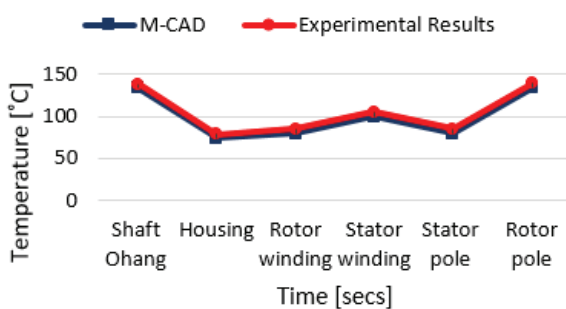

Fig. 21. The M-CAD and experimental results of the ISRM.

IV. CONCLUSIONS

In this paper, a 6/4 ISRM with an oil cooling system for electric vehicle application was proposed. The 6 kW machine was built, and transient electromagnetic analysis was performed in ANSYS-Maxwell. The torque capability of the ISRM was examined and compared with a conventional SRM. The result confirms that the ISRM has 85% more torque density, compared to the conventional SRM. The simulation results showed that the ISRM has a short flux path, which leads to a higher level of energy conversion efficiency. To predict the thermal behavior of the machine, an oil spray cooling system was applied to the ISRM model in ANSYS-Motor-Cad. The appropriate design was accomplished, and the hotspots of the machine were determined. For an actual traction application, at least a 50 kW ISRM should have been designed and tested, but it was only possible to construct a 6 kW prototype. The 6 kW ISRM and the appropriate cooling system were built and tested, and the experimental results were presented.

REFERENCES

[1] B. Rezaeealam and F. Rezaee-Alam, "Optimization of permanent magnet synchronous motors using conformal mappings," *Applied Computational Electromagnetics Society (ACES) Journal*, vol. 32, no. 10, pp. 915-923, Oct. 2017.

[2] Y. Wang, H. Tan, Y. Wu, and J. Peng, "Hybrid electric vehicle energy management with computer vision and deep reinforcement learning," *IEEE Transactions on Industrial Informatics*, vol. 17, no. 6, pp. 3857-3868, June 2021.

[3] B. Poudel, E. Amiri, P. Rastgoufard, and B. Mirafzal, "Toward less rare-earth permanent magnet in electric machines: A review," *IEEE Transactions on Magnetics*, vol. 57, no. 9, Sep. 2021.

[4] G. Qu and Y. Fan, "Design of a new consequent-pole segmented dual-stator permanent magnet machine," *IEEE Transactions on Magnetics*, vol. 58, no. 2, Feb. 2022.

[5] S. Corovic and D. Miljavec, "Modal analysis of different stator configurations to mitigate electro-magnetically excited audible noise and vibrations of switched reluctance motors," *Applied Computational Electromagnetics Society (ACES) Journal*, vol. 32, no. 12, pp. 1089-1097, Dec. 2017.

[6] D. F. Valencia, R. Tarvirdilu-Asl, C. Garcia, J. Rodriguez, and A. Emadi, "Vision, challenges, and future trends of model predictive control in switched reluctance motor drives," *IEEE Access*, vol. 9, pp. 69926-69937, May 2021.

[7] M. Abbasian, M. Moallem, and B. Fahmi, "Double stator switched reluctance motors: Fundamentals and magnetic force analysis," *IEEE Trans. Energy Convers*, vol. 25, no. 3, pp. 589-597, Dec. 2010.

[8] B. C. Mecrow, E. A. El-Kharashi, J. W. Finch, and A. G. Jack, "Preliminary performance evaluation of switched reluctance motors with segmental rotors," *IEEE Trans. Energy Convers*, vol. 19, no. 4, pp. 679-686, Dec. 2004.

[9] S. Mehta, M. A. Kabir, P. Pramod, and I. Husain, "Segmented rotor mutually coupled switched reluctance machine for low torque ripple applications," *IEEE Transactions on Industry Applications*, vol. 57, no. 4, pp. 3582-3594, July-Aug. 2021.

[10] M. A. J. Kondelaji and M. Mirsalim, "Segmented-rotor modular switched reluctance motor with high torque and low torque ripple," *IEEE Transactions on Transportation Electrification*, vol. 6, no. 1, pp. 62-72, Mar. 2020.

[11] M. Abbasian, "Induction switched reluctance motor," U.S. Patent US20170370296A1, June 30 2020.

[12] A. K. Rana and A. V. Raviteja, "A mathematical torque ripple minimization technique based on nonlinear modulating factor for switched reluctance motor drives," *IEEE Transactions on Industrial Electronics*, vol. 69, no. 2, pp. 1356-1366, Feb. 2022.

[13] C. Liu, D. Gerada, Z. Xu, Y. C. Chong, M. Michon, J. Goss, and H. Zhang, "Estimation of oil spray cooling heat transfer coefficients on hairpin windings with reduced-parameter models," *IEEE Transactions on Transportation Electrification*, vol. 7, no. 2, pp. 793-803, June 2021.

Ali Madani Mohammadi was born in Isfahan, Iran, in 1985. He is a Ph.D. student in power engineering. Since 2015 he has been working as a visiting professor at the Technical Engineering Department of Islamic Azad University, Isfahan Branch (Khorasgan). His research interests include electric motors, drive and renewable energy.

Mohammadali Abbasian was born in Gaz, Isfahan, Iran. He received his bachelor's, M.Sc. and Ph.D. degrees in electrical engineering from the Isfahan University of Technology, in 2002, 2004 and 2011, respectively. From 2009 to 2010, he was a Ph.D. Exchange Student with Renewable Energies and Vehicular Technologies at the University of Texas at Arlington, Arlington, TX, USA. From 2017 to 2018, he was a Research Scientist with Bundeswehr University, Munich, Germany. He is currently an assistant professor with IAU University, Khorasgan, Isfahan.

Majid Delshad was born in Isfahan, Iran, in 1979. He received his B.S. and M.S. degrees in electrical engineering in 2001 and 2004 from Kashan University and Isfahan University of Technology, Iran, respectively. He received his Ph.D. degree also in electrical engineering from Isfahan University of Technology. He is an associate professor in Isfahan (Khorasgan) Branch, IAU. His research interests include soft switching techniques in DC-DC converters and current-fed converters.

Hadi Saghafi was born in Isfahan, Iran, in 1982. He studied at Isfahan University of Technology, receiving his B.Sc. in 2004, M.Sc. in 2007 and Ph.D. in 2014, all in power engineering. Since 2015, he has been with the Department of Technical Engineering, Isfahan (Khorasgan) Branch, Islamic Azad University, where he is an assistant professor. His research interests include microgrids, distributed generation, control in power electronics, application of power electronics in power systems and motor drives.

Sub-harmonic-based Cost-effective Brushless Wound Rotor Synchronous Machine Topology

Syed Sabir Hussain Bukhari[1] and Jong-Suk Ro[2]

[1]Department of Electrical Engineering
Sukkur IBA University, Sukkur 65200, Sindh, Pakistan

[2]School of Electrical and Electronics Engineering
hung-Ang University, Seoul 06974, South Korea
Corresponding author: Jong-Suk Ro
jongsukro@gmail.com

Abstract **–** This paper proposes a sub-harmonic-based brushless wound rotor synchronous machine (WRSM) topology. The proposed topology involves two three-phase stator windings with a different number of turns. Both windings are linked in parallel and are provided with current from a single inverter. One of these windings is a four-pole winding while the second winding is a two-pole winding. This arrangement generates a magneto-motive force (MMF) in the air-gap of the machine comprising of two components: a regular fundamental MMF and a sub-harmonic MMF. The fundamental component produces the main stator field whereas the sub-harmonic component generates a sub-harmonic field that is utilized to produce a harmonic current in a two-pole rotor harmonic winding. The induced harmonic current is rectified to inject direct current (DC) to the field winding and produce a four-pole rotor magnetic field. The four-pole rotor magnetic field when magnetically interacts with the same number of the main stator field poles producing torque. Finite element analysis (FEA) is carried out to confirm the operation and achieve the electromagnetic behavior of the proposed topology.

Index Terms **–** finite element analysis, sub-harmonic brushless operation, wound rotor synchronous machine.

I. INTRODUCTION

In recent years, several researchers have been exploring brushless topologies of wound rotor synchronous machines (WRSMs) in order to minimize the usage of permanent magnets (PMs) for the development of machine systems [1], [2]. The main reason behind this approach is the rising price of rare-earth metals used to develop high-performance-based PMs. In addition, PM machines require sophisticated flux-weakening strategies to achieve controllable speed and torque characteristics when they are used in electric vehicle (EV) and hybrid electric vehicle (HEV) applications [3], [4]. The classical brushless WRSM topologies involve additional exciters for the rotor field excitation, which make them expensive and bulky, and hence less practical to be adopted in several industrial applications. On the other hand, the rotor field excitation systems based on the harmonic field excitation technique offer several advantages over the classical WRSM topologies [5–7].

Earlier, a sub-harmonic-based brushless WRSM topology that required dual-inverter configuration was proposed in [8]. The stator winding of this topology was divided into two halves with a distinct star-connection. Each half of the armature winding was supplied with a different magnitude of current. This arrangement achieved the brushless operation for WRSMs; however, the rotor of the machine encountered the high magnitude of unbalanced radial forces which developed due to the different magnitude of currents in the two halves of the machine air-gap. In addition, the efficiency of the machine was also low. Later on, a high-efficient, sub-harmonic-based brushless WRSM topology was proposed in [9]. This topology involved a dual-inverter and circumferentially distributed dual-winding configurations as presented in Fig. 1. The windings of the machine were supplied with different magnitude of currents to develop sub-harmonic magneto-motive force (MMF) in the air-gap of the machine. Besides the brushless operation for WRSMs, this topology offers higher efficiency, higher average torque and lower torque ripple as compared to the sub-harmonic-based brushless WRSM topology proposed in [8]. In addition, the magnitude of the unbalanced radial force for the rotor of the machine was also found to be low.

In this paper, a sub-harmonic-based brushless WRSM topology that involves a single-inverter and
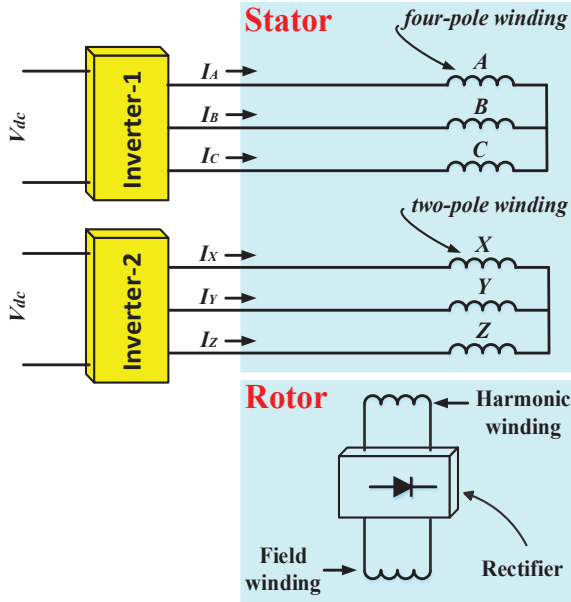
Fig. 1. Conventional dual-inverter, sub-harmonic-based BL-WRSM topology.

dual-winding configurations is proposed. Both stator windings have a different number of turns and are connected in parallel. One of these windings is a four-pole winding, whereas the second winding is a two-pole winding. Unlike the conventional sub-harmonic-based brushless WRSM topologies which require a dual-inverter configuration [8], [9], the proposed topology requires a single inverter which makes it cost-effective, when it is compared to the conventional sub-harmonic-based brushless WRSM topologies. In addition, the proposed topology provides control over the currents of the two-pole winding by employing a variable resistor. Once the inverter supplies the three-phase current to the stator windings, an MMF comprising of two components, a regular fundamental MMF and a sub-harmonic in the air-gap, is produced. The fundamental MMF generates the main stator field whereas the sub-harmonic MMF generates the sub-harmonic field that is used to induce a harmonic current in the two-pole rotor harmonic winding. The induced harmonic current is rectified to inject DC to the rotor field winding and produce a four-pole rotor magnetic field. The magnetic interaction of the four-pole rotor magnetic field with the same number of main stator field poles produces torque. The operation and electromagnetic performance of the proposed topology is discussed in the subsequent sections.

II. OPERATING PRINCIPLE

The simplified illustration of the proposed sub-harmonic-based brushless wound rotor synchronous

machine (WRSM) topology is presented in Fig. 2. As shown in the figure, this topology consists of two stator windings namely ABC and XYZ. Both windings are connected in parallel through a variable resistor (VR) and are powered from a single inverter. ABC winding is a four-pole winding whereas XYZ winding is a two-pole winding. The purpose of the VR is to control the current of the two-pole winding which eventually adjusts the sub-harmonic MMF component in the air-gap of the machine. This leads to control of the performance of the machine by tuning the resistance of the VR and controlling the sub-harmonic MMF of the machine. The rotor of the topology is equipped with a four-pole rotor field winding and a two-pole harmonic winding. These windings are connected in series through a rectifier. The machine structure which is based on a four-pole and twenty-four-slot configuration is presented in Fig. 3. As the machine is supplied with current (I_{abc}) from a single inverter, a different magnitude of current flows through ABC and XYZ windings due to their different number of turns. These currents are shown in equations (1) and (2):

$$\left. \begin{array}{l} I_A = I\cos\omega t \\ I_B = I\cos\left(\omega t - \frac{2\pi}{3}\right) \\ I_C = I\cos\left(\omega t + \frac{2\pi}{3}\right) \end{array} \right\}, \qquad (1)$$

$$\left. \begin{array}{l} I_X = I_a - I\cos\omega t \\ I_Y = I_b - I\cos\left(\omega t - \frac{2\pi}{3}\right) \\ I_Z = I_c - I\cos\left(\omega t + \frac{2\pi}{3}\right) \end{array} \right\}. \qquad (2)$$

The above currents result in an MMF as shown in Fig. 4 (a). The FFT analysis of the developed MMF results in dominating fundamental and sub-harmonic
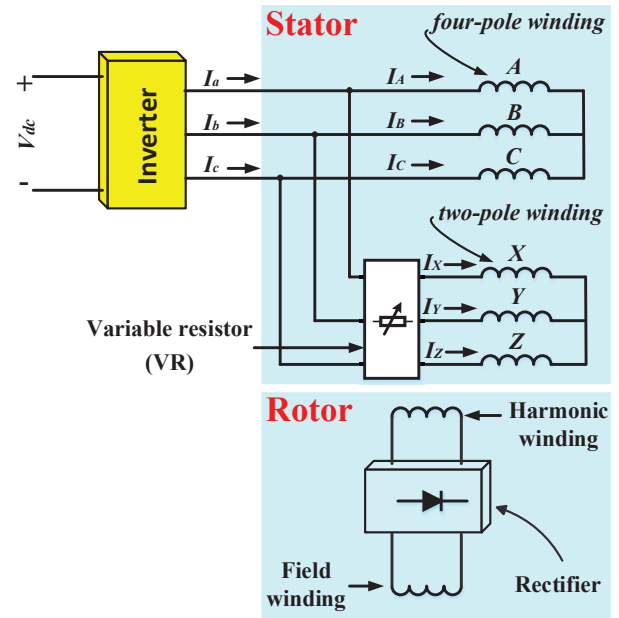

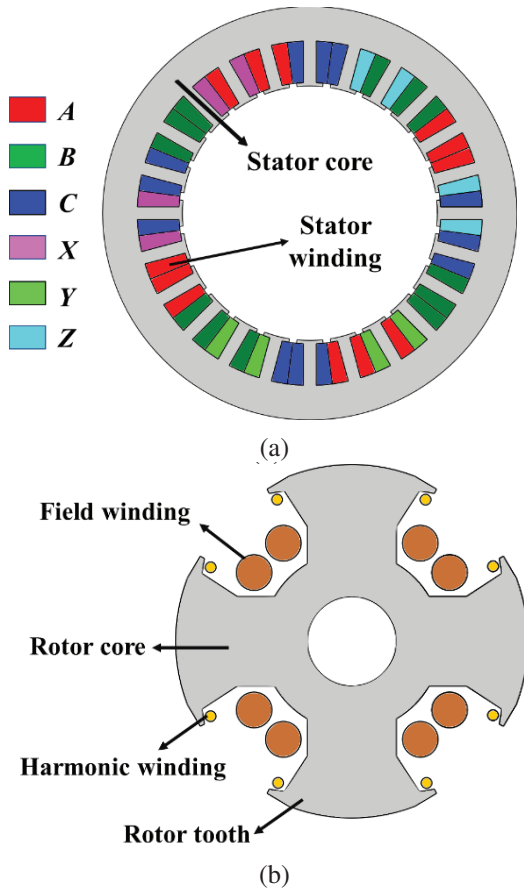Fig. 2. Proposed single-inverter, sub-harmonic-based BL-WRSM topology.

Fig. 3. (a) Stator and (b) rotor structures of the machine.

MMF components as shown in Fig. 4 (b). A simplified illustration of these dominating MMF components is presented in Fig. 4 (c). Mathematically, the MMF of the machine can be calculated using the following equation:

$$F = \frac{3 N_{ABC} I}{4\pi} \cos(\omega t - \theta) + \frac{3 N_{XYZ} I}{2\pi} \cos\left(\frac{\omega t - \theta}{2}\right), \quad (3)$$

where I is the maximum amplitude of the current, N_{ABC} is the number of ABC winding turns, N_{XYZ} is the number of XYZ winding turns, F is the total generated MMF and θ is the spatial angle.

The fundamental MMF component develops the main stator field whereas the sub-harmonic MMF produces the harmonic current in the harmonic winding of the rotor through the electromagnetic induction. This current is rectified and supplied to the rotor field current to develop the four-pole rotor field in order to achieve the brushless operation. The electromagnetic interaction of the four-pole stator and four-pole rotor fields produces torque. The simplified illustration of the operating principle of the proposed sub-harmonic-based brushless WRSM topology is presented in Fig. 5. This figure shows that there is an absence of electromagnetic connection
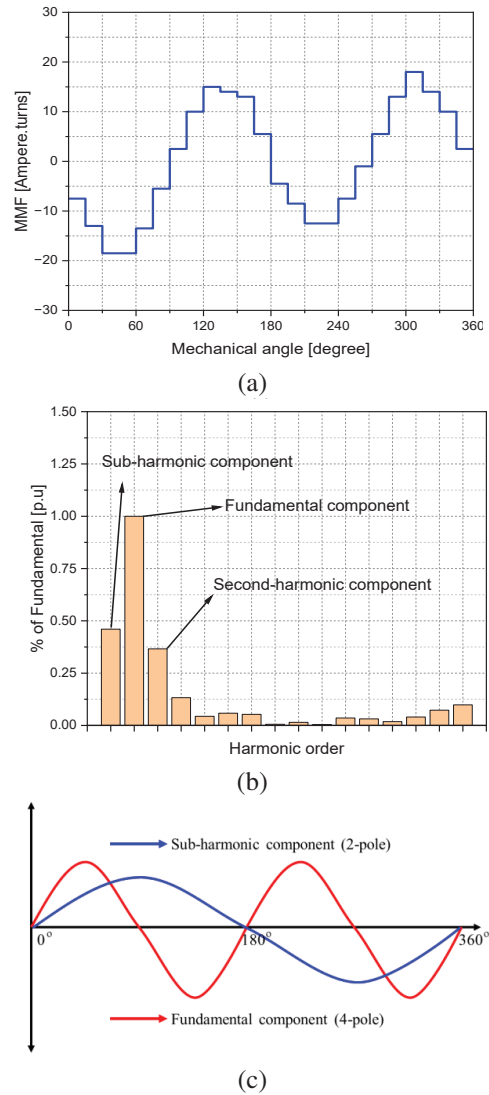

Fig. 4. For the proposed single-inverter, sub-harmonic-based BL-WRSM topology: (a) MMF plot, (b) THD of the MMF plot, and (c) MMF components.
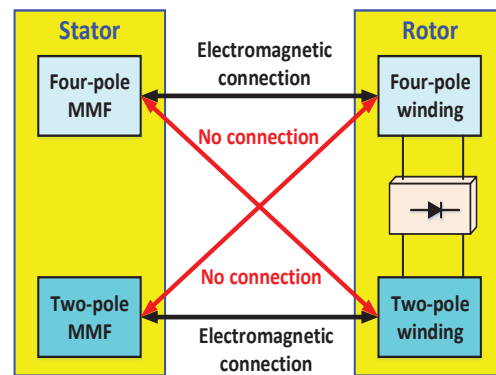

Fig. 5. Operating principle of the proposed single-inverter, sub-harmonic-based BL-WRSM topology.

between the four-pole stator MMF and two-pole rotor harmonic winding, and the two-pole stator and four-pole rotor field winding. This is because the speed of both MMF components is not the same. In fact, the speed of the sub-harmonic MMF component is half of the speed of four-pole MMF.

III. ELECTROMAGNETIC ANALYSIS

To achieve the electromagnetic performance of the proposed topology, FEA is conducted in JMAG-Designer ver.19.1 for a four-pole, twenty-four-slot machine. The parameters of this machine are presented in Table 1. The stator and rotor structures of the machine are presented in Fig. 3, whereas their winding configurations are presented in Fig. 6. The machine is operated at 1800 rpm and the inverter injects a three-phase current (I_{abc}) having the magnitude of 10 A (peak) to the two-pole and four-pole stator windings. The inverter

output current (I_{abc}) is presented in Fig. 7. The two-pole winding (XYZ) has 90 turns whereas the four-pole winding (ABC) has 270 turns. As the number of turns for both windings are kept different, a current of unequal magnitude flows through each winding. The currents of ABC and XYZ windings i.e., I_{ABC}, and I_{XYZ} are presented in Fig. 8. These currents produce an MMF in the air-gap comprising of fundamental and sub-harmonic components. Figure 9 shows the flux - y plot of the machine. The fundamental component generates the main four-pole stator field whereas the sub-harmonic component induces a harmonic current in the two-pole rotor harmonic winding. The induced harmonic current is rectified to inject DC to the main rotor field winding to create the rotor field. The harmonic and rectified field currents are presented in Fig. 10.

Table 1: Machine parameters

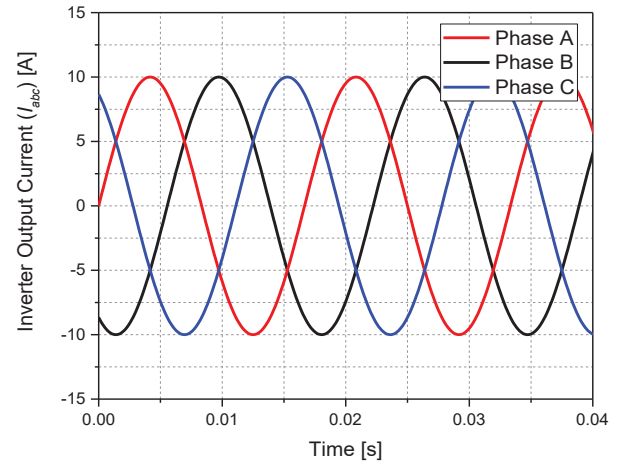| Parameter	Value
Rated power	4.55 kW
Rated speed	1800 rpm
Rated current	10 A (peak)
Stator/rotor outer diameter	130/79 mm
Air-gap length	0.5 mm
Shaft diameter	20 mm
Stack length	120 mm
Stator slots	24
Field/harmonic winding poles	4/2
Stator four-pole (ACB) winding turns	270
Stator two-pole (XYZ) winding turns	90
Field/harmonic winding turns	150/15
Variable resistor (VR)	1 Ω

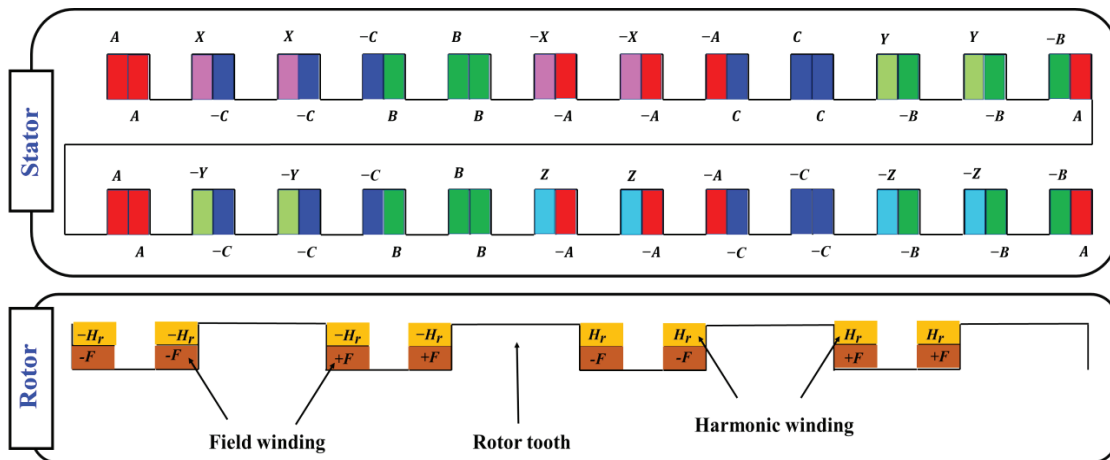Fig. 7. Inverter output current.

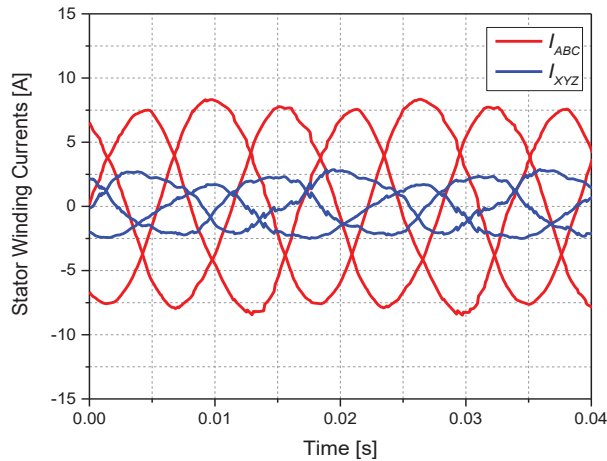Fig. 6. Stator and rotor winding configurations.
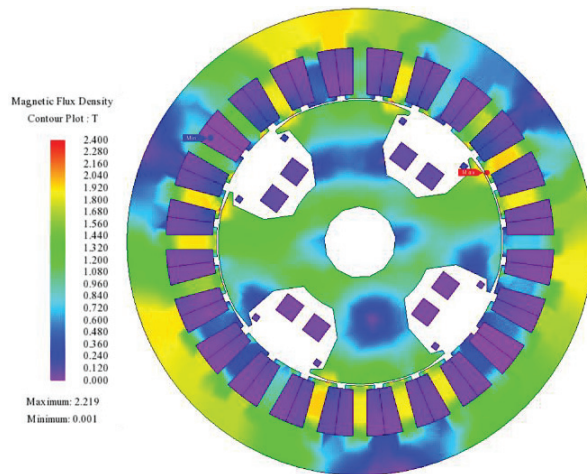
Fig. 8. Stator winding currents.

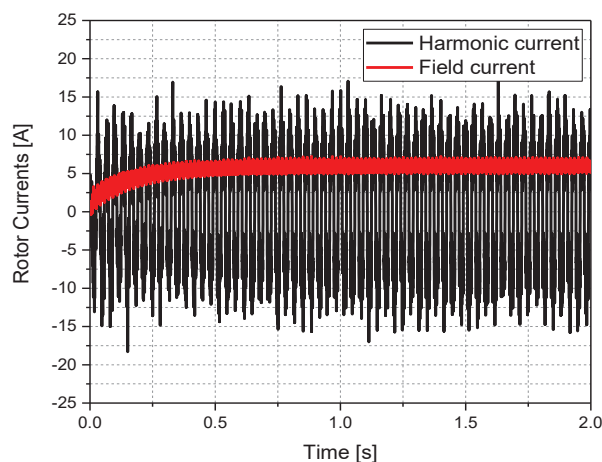Fig. 9. Magnetic flux density plot of the machine.
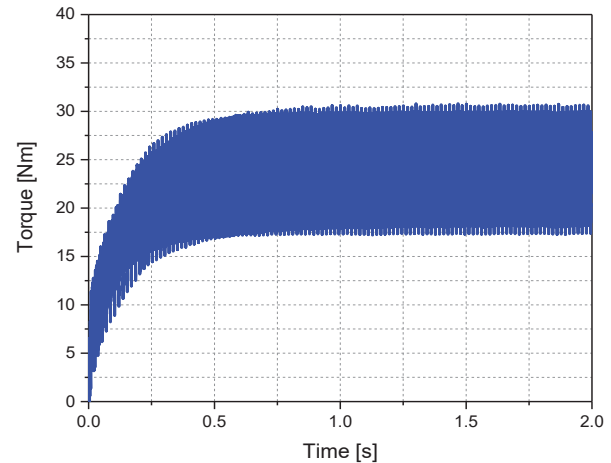

Fig. 10. Rotor currents.

Fig. 11. Torque.

The magnetic interaction of the four-pole rotor and stator fields develops torque. This torque is shown in Fig. 11.

The average generated torque for the proposed sub-harmonic-based brushless WRSM topology is 24.133 Nm under steady-state operation. However, the maximum and minimum torques are around 30.7 Nm and 17.3 Nm, respectively. A torque ripple of around 55.52% is produced which can be minimized by optimizing the machine using parametric optimization algorithms and skewing methods.

IV. CONCLUSION

A sub-harmonic-based, cost-effective, brushless WRSM topology based on a single inverter and dual-stator armature winding configurations was proposed in this paper. The proposed topology used a two-pole and four-pole stator windings having a separate star-connection and a different number of turns. This generated an MMF comprising fundamental and sub-harmonic components. The fundamental component was used to develop the main field and the sub-harmonic component was used to produce a harmonic current in a rotor harmonic winding, which was rectified to excite the rotor field winding to achieve a brushless operation. A four-pole, twenty-four-slot machine was used to achieve electromagnetic torque and justify the operation of the proposed topology.

The proposed brushless WRSM topology is cost-effective, when it is compared to the conventional sub-harmonic-based WRSM topologies which require a dual-inverter configuration. Furthermore, it is simple as it does not require any sophisticated control strategies or power electronics devices, except a typical three-phase inverter.

As the two-pole winding is in parallel with the four-pole winding, its current may be controlled using a rheostat to develop the required magnitude of harmonic MMF, which eventually will provide the freedom to develop the required magnitude of output torque.

ACKNOWLEDGMENTS

REFERENCES

[1] M. Ayub, A. Hussain, G. Jawad, and B. Kwon, "Brushless operation of a wound-field synchronous machine using a novel winding scheme," *IEEE Transactions on Magnetics*, vol. 55, no. 6, pp. 1-4, June 2019.

[2] C. Chakraborty, S. Basak, and Y. T. Rao, "Synchronous generator with embedded brushless synchronous exciter," *IEEE Transactions on Energy Conversion*, vol. 34, no. 3, pp. 1242-1254, Sep. 2019.

[3] S. S. H. Bukhari, A. A. Memon, S. Madanzadeh, G. J. Sirewal, J. Doval-Gandoy, and J.-S. Ro, "Novel single inverter-controlled brushless wound field synchronous machine topology," *Mathematics*, vol. 9, no. 15, pp. 1739, 2021.

[4] S. S. H. Bukhari, F. H. Mangi, I. Sami, Q. Ali, and J.-S. Ro, "High-harmonic injection-based brushless wound field synchronous machine topology," *Mathematics*, vol. 9, no. 15, pp. 1721, 2021.

[5] G. Jawad, Q. Ali, T. A. Lipo, and B. I. Kwon, "Novel brushless wound rotor synchronous machine with zero-sequence third-harmonic field excitation," *IEEE Transactions on Magnetics*, vol. 52, no. 7, pp. 1-4, July 2016.

[6] N. Jiao, W. Liu, Z. Zhang, T. Meng, J. Peng, and Y. Jiang, "Field current estimation for wound-rotor synchronous starter-generator with asynchronous brushless exciters," *IEEE Transactions on Energy Conversion*, vol. 32, no. 4, pp. 1554-1561, 2017.

[7] F. Yao, D. Sun, L. Sun, and T. A. Lipo, "Dual third-harmonic-current excitation principle of a brushless synchronous machine based on double three-phase armature windings," *2019 22nd International Conference on Electrical Machines and Systems (ICEMS)*, Harbin, China, pp. 1-4, 2019.

[8] Q. Ali, T. A. Lipo, and B. I. Kwon, "Design and analysis of a novel brushless wound rotor synchronous machine," *IEEE Transactions on Magnetics*, vol. 51, no. 11, pp. 1-4, Nov. 2015.

[9] S. S. H. Bukhari, Q. Ali, J. Doval-Gandoy, and J.-S. Ro, "High-efficient brushless wound rotor synchronous machine topology based on sub-harmonic field-excitation technique," *Energies*, vol. 14, no. 15, pp. 4427, 2021.

Syed Sabir Hussain Bukhari received his B.E degree in Electrical Engineering from Mehran University of Engineering and Technology, Jamshoro, Pakistan, in 2009, and Ph.D. from the Department of Electronic Systems Engineering, Hanyang University, South Korea in 2017. He joined Sukkur IBA University as an Assistant Professor in December 2016. He is currently working as a Research Professor at Chung-Ang University, Seoul, South Korea under the Korean Research Fellowship (KRF) program. His main research interests include electric machine design, power quality and drive controls.

Jong-Suk Ro received his B.S. degree in Mechanical Engineering from Han-Yang University, Seoul, Korea, in 2001 and his Ph.D. in Electrical Engineering from Seoul National University (SNU), Seoul, Korea, in 2008.

He conducted research at the R&D center of Samsung Electronics as a Senior Engineer from 2008 to 2012. From 2012 to 2013, he was at Brain Korea 21 Information Technology of SNU, as a Post-Doctoral Fellow. He conducted research at the Electrical Energy Conversion System Research Division of the Korea Electrical Engineering & Science Research Institute as a Researcher in 2013. From 2013 to 2016, he worked at Brain Korea 21 Plus, SNU, as a BK Assistant Professor. In 2014, he was at the University of Bath, UK. Currently, he is an Associate Professor of the School of Electrical and Electronics Engineering, Chung-Ang University, Seoul, Korea.

His research interests include the analysis and optimal design of next-generation electrical machines using smart materials such as electromagnetic, piezoelectric, and magnetic shape memory alloys.